Multi-scale Diffusion Processes
From Hydrogen Bonds to Human Skin

im Fachbereich Physik der Freien Universität Berlin eingereichte Dissertation

zur Erlangung des akademischen Grades eines Doktors der Naturwissenschaften (Dr. rer. nat.)

vorgelegt von
Robert Schulz

Berlin, 2018

Erster Gutachter:	Prof. Dr. Roland R. Netz Freie Universität Berlin
Zweiter Gutachter:	Prof. Dr. Frank Noé Freie Universität Berlin
Tag der Disputation:	30.11.2018

Contents

Chapter 1

Introduction

Diffusion is ubiquitous in nature. It takes place on the microscopic scale, such as the diffusive motion of molecules [1] or the motion of proteins in biological cells [2] and even on the ultra-macroscopic scale like the diffusion of galactic nuclei [3].

In other disciplines such as economics, the motion of stock prices and option pricing for example are modeled based on diffusion equations [4, 5]. In sociology, the field of *diffusion of innovations* [6] seeks to understand at which rate and how innovations, like information, ideas or technology, are spreading and attracting new individuals, and in linguistics the concept of diffusion is used to understand the spreading of languages [7].

In physics, and in particular in the context of biological systems on small length scales up to the size of molecules and atoms, the diffusive motion manifests in a random movement of particles and is, thus, very different from the macroscopic point of view where the knowledge of an initial configuration predicts the smooth and continuous behavior of the future state like the trajectory of a falling object in the gravitational field of a planet. Judging from a macroscopic point of view it is remarkable that we do not feel that we are actually embedded in an ocean of jittering molecules performing seemingly random motions.

From a historical perspective until the beginning of the 19th century there was only little knowledge about diffusion. It was Thomas Graham, who first studied the diffusion in gases systematically [8, 9], followed by studies of James Clerk Maxwell, who could accurately estimate the diffusion coefficient of carbon dioxide [10]. In between, Adolph Fick, inspired by the work of Graham, postulated two diffusion laws [11] which state that the diffusive flux points from areas with high concentration to areas with low concentration with a rate that is proportional to the gradient of the concentration (Fick's first law), and that the concentration changes in time under the influence of diffusive motion (Fick's second law) described in mathematical terms in modern notation by

$$\frac{\partial c(x,t)}{\partial t} = D\frac{\partial^2 c(x,t)}{\partial x^2}, \tag{1.1}$$

where $c(x,t)$ is the concentration of the diffusing particle and D is the diffusion constant.

Significant progress was achieved when Einstein and Smoluchowski embraced the topic of diffusion at the beginning of the 20th century [12, 13]. In particular, they examined the phenomena of *Brownian motion*, named after the Scottish botanist Robert Brown, who first studied the motion of pollen grains supended in liquid water [14]. Einstein took a purely theoretical approach and concluded that if the existence of atoms is true, then particles suspended in a viscous medium must undergo random irregular motion due to collisions with other molecules. The ideas he developed could later be used by Jean-Baptiste Perrin for his research on Brownian motion to prove the existence of atoms in estimating the Boltzmann constant [15–17].

Smoluchowski derived a partial differential equation, known as the *Smoluchowski* or *Fokker-Planck equation*, which describes the diffusive motion of a particle in a free-energy landscape $F(x)$ with a position-dependent diffusivity profile $D(x)$

$$\frac{\partial}{\partial t}c(x,t) = \frac{\partial}{\partial x}\left(D(x)e^{-\beta F(x)}\frac{\partial}{\partial x}c(x,t)e^{\beta F(x)}\right), \tag{1.2}$$

where $\beta = 1/(k_B T)$ is the inverse thermal energy. The free energy reflects the local affinity of the diffusing substance and describes how the substance partitions in equilibrium, whereas the diffusivity describes the position-dependent rate at which the substance diffuses in the absence of external forces. Note that this equation transforms into Eq. (1.1) when the diffusivity and free energy become a constant. The Smoluchowski equation has been used in numerous systems such as protein folding with a position-dependent diffusivity [18], diffusion of particles near interfaces [19] or even in discplines outside the biomolecular domain such as decision-processes and market-strategies [20, 21].

Einstein's and Smoluchowski's approach is based on the time evolution of the ensemble of trajectories governed by partial differential equations [22, 23], whereas another direction tackles the problem of describing individual trajectories by stochastic differential equations [24, 25], with the Langevin equation [26] as the most prominent example. Both descriptions are equivalent and can be converted into each other based on different approaches [22, 27] and opened an entirely new field which is nowadays known as the field of *stochastic processes* with applications in a multitude of disciplines.

In this thesis, we discuss diffusion processes on different scales and environments. In particular, on the microscopic scale we analyze the diffusive motion of water molecules in pure water and on the the mesoscopic scale we discuss the dynamics of drug diffusion in human skin.

1.1 Water dynamics

In the experiment, Robert Brown performed in the beginning of the 19th century, not only the pollen grains diffuse around in liquid water, but also the water molecules perform a diffusive motion on the microscopic scale. Needless to say, water plays a crucial

role in many aspects of life [28, 29]. The human body consists mainly of water [30], where most of which is located inside the cells [31]. As a solvent it influences the structure of macromolecules [32], e.g in protein folding [33]. Undesired conformational changes of a protein can lead to neurodegenerative diseases such as Huntington's or Alzheimer's disease [34, 35]. Water plays such an important role in life, that looking for conditions of life beyond our planet is equivalent of looking for water on extraterrestrial objects [36].

A water molecule H_2O consists of an oxygen and two hydrogen atoms aligned such that the HOH-angle is $104.45°$. Compared to other molecules with similar size such as methane CH_4, oxygen difluoride OF_2, or carbon dioxide CO_2, a unique difference emerges. At ambient conditions water is liquid, whereas for the other three substances the boiling temperature is significantly below zero degrees Celsius. This is somewhat surprising, since e.g. oxygen difluoride and water have almost the same geometry with a bond angle of $103°$ for oxygen difluoride. The explanation lies in the fact that water forms hydrogen bonds (H-bonds) which arise from the strong polarity of water due to the larger electronegativity of the oxygen atom compared to the hydrogen atom. Water can donate and accept two H-bonds so that in the ice phase a water molecule participates in four bonds, whereas in the liquid phase the actual number is smaller, since H-bonds are broken more often due to thermal fluctuations. In liquid water an H-bond between two water molecules is only kept for a time span of picoseconds before it is broken and a new bond is formed with a new partner [37, 38]. Hydrogen bonds also control the properties of interfacial water such as the surface tension of water at the air-water interface [39]. The H-bond network is altered in the presence of solutes. For example, polar solutes adapt usually well into the existing water structure [40], whereas hydrophobic molecules are enclosed in a cavity by the surrounding water molecules [41], which can even strengthen the H-bonds around the hydrophobic molecule [42]. In general, whenever a charge redistribution in aqueous environments occurs it is directly related to rearrangements of the H-bond network and, thus, to the reorientation of individual H-bonds [43].

It is a long standing goal [44] to understand the underlying mechanism of H-bond rearrangements in liquid water. Even the most simple process of breaking and forming of an H-bond between two water molecules that are part of the bulk water system is still not completely understood.

As a matter of fact, it is not easy to observe exchanges of H-bonds. On the experimental side, techniques such as infrared pump-probe spectroscopy [45–48], nuclear magnetic resonance (NMR) [49, 50], quasi-elastic neutron scattering [51, 52], terahertz spectroscopy [53], and dielectric spectroscopy [54] are used frequently to study the individual motion of water molecules which are able to resolve motions up to the fs-domain. On the theoretical side, molecular dynamics (MD) simulations provide an elegant tool to study water dynamics, e.g. MD-simulation of water as shown in Fig. 1.1. Originally, MD-simulations were developed in the 1950's [55] and have constantly evolved to be capable of simulating large-size proteins [56]. In these simulations the trajectories of each atom or molecule is calculated by solving Newton's equations of

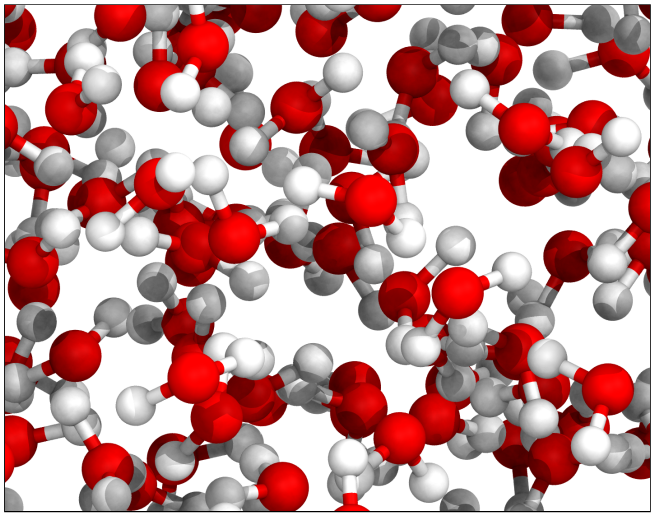

Figure 1.1: Snapshot of a MD-simulation of SPC/E water at $T = 300$K.

motions numerically for a small time step. This process is continued iteratively to obtain a trajectory for a given time span.

With the help of MD-simulations of bulk water it was proposed [57, 58], that in half of the H-bond breaking events a new H-bond is formed right after. And just about a decade ago it has been suggested that the H-bond exchange occurs mainly via large-angular jumps where a water rotates quickly from one acceptor to another [37, 59].

Most certainly, MD-simulations opened new perspectives for the understanding of water-reorientation dynamics, but the overwhelmingly large state space spanned by only a couple of hundred water molecules, aside from far more complex systems like membranes or proteins, is still hard to analyze. A variety of concepts have been established such as replica-exchange, umbrella sampling or transition path sampling in order to derive the free-energy landscape and the slow time scales [60–62] of biomolecular processes. A prominent example, which has gained ample attraction within the last decade, are Markov state models (MSM). The term Markov or Markovian refers to the fact that the future configuration of the system depends solely on its current state, hence it is independent of its past configuration [63].

Markov state models have been extensively used to understand the dynamics of a solute, like in the context of protein folding [64–66] or ligand-binding processes [67, 68], but are rarely used to understand the dynamics of the solvent itself [69, 70]. Further, Markov state models allow to identify the slow processes in the large conformational state space and can be regarded as a coarse-graining of the dynamics of the entire system, which is achieved in projecting onto only a relatively small number of states, see Fig. 1.2. MSMs can not only predict the stationary properties such as the free-energy landscape, but also kinetic quantities and processes. The estimation is encapsulated in a (i) reduction or discretization of the in general high-dimensional state space spanned

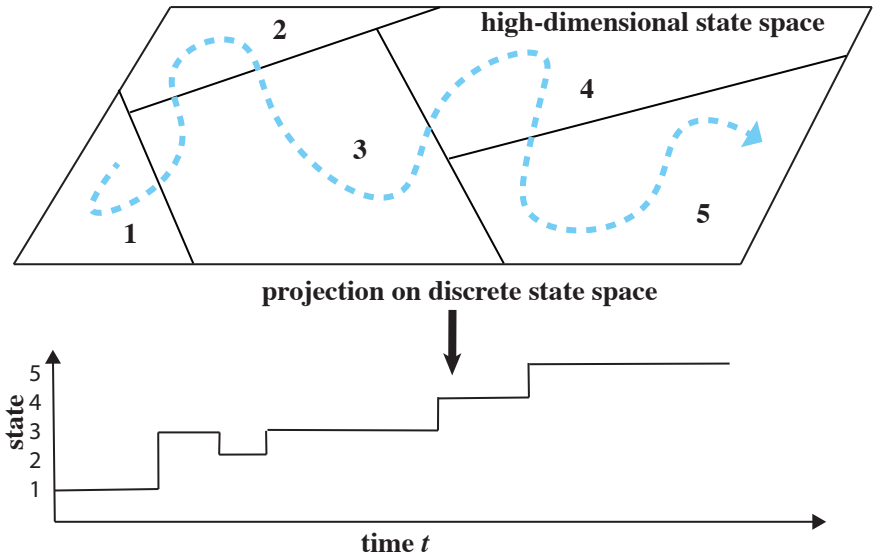

Figure 1.2: The trajectory of the continuous dynamics (cyan dashed line) is projected onto a coarse-grained discrete state space. The resulting process is a Markov jump processes, which approximates the original continuous stochastic process.

by all momenta and positional degrees of freedom of all atoms, and (ii) a model which describes the stochastic transitions between different states. The transitions are governed by a transition probability matrix $T_{ij}(\tau)$ which describes the conditional probability to be in state j at time τ, given one started in state i at time 0. The matrix is estimated from a trajectory by counting transitions from one to another state described by

$$T_{ij}(\tau) = \frac{c_{ij}(\tau)}{\sum_{k=1}^{N} c_{ik}(\tau)}, \tag{1.3}$$

where N is the number of coarse-grained states, and $c_{ij}(\tau)$ is the observed number of jumps from state i to j after time τ [71]. The stationary state can be easily deduced from the matrix in terms of an eigenvalue problem

$$\sum_{i=1}^{N} \pi_i T_{ij}(\tau) = \pi_j, \tag{1.4}$$

where π_j is the stationary distribution, the probability to be in state j. The free energy according to $F_i = -\ln(\pi_i)$ can be calculated right away. The eigenvalues λ_i of the transition matrix are directly related to the molecular relaxation time scales via $t_i = -\tau / \ln(|\lambda_i(\tau)|)$, whereas the eigenvectors $\mathbf{r}_i$ are related to structural reconfigurations. This is at the heart of MSMs, the power to make the large amount of MD-data interpretable, and to obtain relevant quantities from an MD-simulation.

In this thesis we analyze trajectories from a classical molecular dynamics simulations of SPC/E water [72] with a Markov state model. At first, we study a water trimer as part of the entire bulk system. As a result, the associated smallest time scales correspond to cooperative interchanges of H-bonds in the water trimer. Later we analyze the switching event of one hydrogen bond between two water molecules and derive the full transition network. The most probable pathway is a direct switch without an intermediate state, which is well in agreement with previous studies [37,57–59]. However, a considerable fraction of transition paths proceeds along different intermediate states that involve alternative H-bonds or unbound states.

1.2 Drug diffusion in human skin

Organism are constructed of functional biological units, called cells, typically of μm-size, which contain materials such as the genome and the cytoskeleton [73]. On this small length scale the regulated transport of molecules through cells comprises an essential factor in a number of tasks a cell has to fulfill. The formation of distinct barriers is another important feature of multicellular organisms, which can be found in different sections of the human body such as the blood-brain barrier, mucosa membranes, and the skin, which constitutes the largest organ in the human organism. An accurate functioning of the skin barrier is provided when desired molecules can penetrate through the barrier, whereas the transport of undesired substances is inhibited [74,75]. Thus it provides a great challenge for the development of drugs [76].

Human skin consists primarily of two layers: the epidermis and dermis [77], see Fig. 1.3. The epidermis, typically about 100 μm thick, prevents the skin from drying out and serves as the main barrier against undesired materials. It is further divided into the stratum corneum, the outmost 10-20 μm thick skin layer which consists of dried-out dead skin cells, and plays a key role in the skin barrier function [78]. A damaged skin barrier is considered the main element for skin diseases such as psoariasis or atopic dermatitis [79,80]. The dermis located right underneath the epidermis contains blood vessels and protects the body against stress and strain.

Since the processes of molecular diffusion in human skin take place in crowded environments, the motion of molecules is of stochastic nature. A variety of diffusion models ranging from 1D to 3D-models incorporating different levels of cell geometries have been established [81–86]. Their common denominator is directly related to Fick's law of diffusion [11].

In Chapter 3 and 4 we focus on diffusive dynamics on the mesoscale. In particular, we discuss drug diffusion in human skin of the lipophilic glucocorticoid dexamethasone which is used to treat autoimmune or inflammatory disorders [87,88].

Drug concentration profiles are derived from X-ray microscopy experiments at three consecutive times, performed by the Rühl group (Chemistry department, FU Berlin). The skin samples have been prepared by the Schäfer-Korting/Hedtrich (Institute of Pharmacy, FU Berlin) and Vogt/Blume-Peytavi group (Dermatology department, Charité

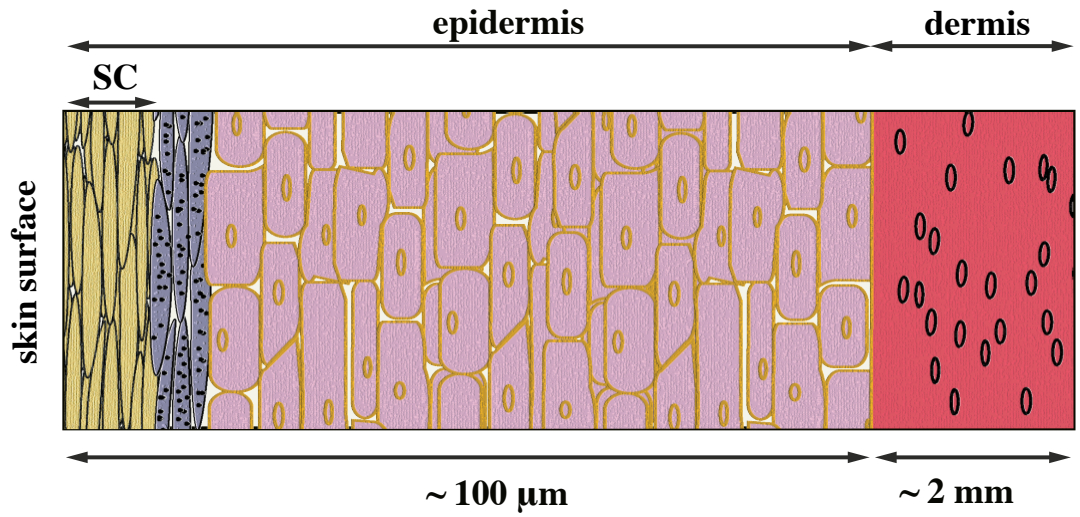

Figure 1.3: Schematic picture of skin. The stratum corneum located at the skin surface and part of the epidermis plays an important role for the skin barrier function. The dermis, underneath the epidermis, contains blood vessels and cushions the human body from stress.

Berlin). The analysis is based on the general 1D-diffusion equation (1.2) with experimental concentration-depth profiles of dexamethasone in human skin as the only input. We present a robust method based on a trust-region algorithm [89, 90] for numerically inverting the general 1D-diffusion Eq. (1.2) to obtain the position-dependent diffusivity and the free-energy profiles of the drug dexamethasone as a function of skin depth without employing further assumptions, since the analysis is purely data-based.

As a result, we show that the skin barrier function depends on the combination of a significantly reduced diffusivity of the drug dexamethasone in the stratum corneum, whereas a pronounced free-energy barrier at the transition from the epidermis to the dermis is revealed. With these two parameters we can predict the penetration into skin and also check the model validity.

In Chapter 4 we compare concentration profiles of dexamethasone originating from healthy and damaged human skin and discuss the robustness of the inversion method introduced in Chapter 3. The resulting free-energy profiles of healthy and damaged skin show almost no deviations, whereas the diffusivity profile of damaged skin is significantly larger in the stratum corneum which results in an enhanced penetration of dexamethasone into skin. The robustness analysis reveals that the inversion method is stable and yields well-defined solutions when more than two concentration profiles are used as input.

Chapter 2

Collective hydrogen-bond rearrangements in liquid water

Bibliographic information. The content of this chapter is in preparation to be submitted to a peer-reviewed journal (Ref. [i]).

2.1 Introduction

Water plays a key role for many biological, chemical, and physical processes [28]. On the microscopic level, water dynamics involves the formation and breaking of hydrogen bonds (H-bonds) which is important for understanding protein [91, 92], ligand-receptor [93], protein-surface [94], electrolyte [95,96], proton [97] and hydrophobic solvation dynamics [98, 99]. Despite the fundamental importance of water dynamics in liquid water, the understanding of collective structural mechanisms remains challenging, such as the switching of a single H-bond from one accepting water molecule to another [100, 101].

The classical view introduced by Debye [44] describes the reorientation dynamics of a water molecule as a diffusion process. According to this model, when an H-bond is broken, the water molecule performs an angular Brownian motion until it finds a new H-bond partner. Although this view provides to straightforwardly interpret the water dielectric relaxation in the GHz regime [95, 96], it was challenged based on two theoretical advancements: Employing transition path sampling in conjunction with classical molecular dynamics simulations, it was suggested that in roughly half of the H-bond breaking events, a new H-bond with a different water molecule is formed right after [58], partly confirming Stillinger's switching-of-allegiance scenario of the local hydrogen bonding dynamics [57].

More explicitly, it has been shown that the switch of an H-bond donor occurs typically through a rather abrupt angular jump [37,59,101], which is supported experimentally by neutron scattering [102, 103] and 2D-IR spectroscopy [47, 104]. In particular, it was demonstrated that the H-bond switch is a cooperative process that at least involves three water molecules [37,59,101]. The prevalence of abrupt rotations suggests that non

H-bonded configurations, also referred to as dangling H-bonds, are free-energetically unstable and therefore should only appear as short-lived transient states that either rebond with its initial H-bond partner or quickly engage in a new H-bond with a different partner, which indeed has been demonstrated in simulations and experiments [105]. Note that an abrupt angular change is not necessarily in conflict with Debye's diffusive model, since the presence of an angular free energy barrier quite naturally predicts a transition path time that is much shorter than the H-bond life time [106–108] (see Results and Discussion Section for more details). Experimentally, H-bond network rearrangements can be studied by femtosecond IR spectroscopy and are characterized by time scales ranging in the sub-picosecond to picosecond range [48, 109–111], THz absorption studies reflect H-bond rearrangements in the sub-picosecond rage [112], while photon echo peak shift studies demonstrate the existence of relaxation phenomena in the 5 to 15 ps range [113]. So based on experimental results, H-bond restructuring relaxation times span a broad range from a few picoseconds down to hundreds of femtoseconds.

Similar questions about the kinetics of H-bond changes also arise in isolated water clusters at low temperatures [114–116], where concerted rotations of water molecules have been observed experimentally and have been interpreted in terms of cooperative H-bond switching. Clearly, in these low-temperature systems the dynamics is governed by quantum tunneling, not by thermally activated barrier crossing. Moreover, and due to the small number of involved molecules and the absence of stochastic effects the possible pathways can for small clusters be enumerated exactly [115, 116].

In contrast, water bonding kinetics in liquid water poses two problems that arise from the coupling to a dynamic finite-temperature environment. Firstly, it is a priori not clear what the minimum number of water molecules should be that would allow to meaningfully define a dynamic restructuring of water, and secondly, the stochastic coupling to a random liquid environment creates a multitude of thermally activated competing pathways that connect given starting and final water structures.

In principle, MD simulations should be able to resolve questions related to local H-bond kinetics and mechanisms unambiguously. However, even given such simulation data, understanding H-bond kinetics and mechanisms is challenging for the human analyst, since the relative conformation of only two water molecules is described by a six-dimensional space (one separation coordinate, two relative angular coordinates and three relative orientational coordinates). Consequently, the state space of three water molecules, the minimal system where collective H-bond switching can be studied, is 12-dimensional, which makes the direct observation of H-bond dynamics in simulation trajectories prohibitively difficult. In this paper we demonstrate that Markov state models (MSMs) [117–119] can provide an analysis framework to study water dynamics in the complete continuum conformational space (spanned by positional and orientational angles and the relative separation) to classify competing dynamic normal modes of H-bond rearrangements in an unbiased and complete fashion.

MSMs haven been proven useful to describe the slow dynamics in systems with many degrees of freedom, for example protein folding [64,120], protein ligand-binding

[121–123] and protein conformation changes [124, 125]. There are only few studies in which MSMs have been developed that account for solvent degrees of freedom [69,70], mostly because the solvent diffusion makes it difficult to define the proper subspace of relevant solvent degrees of freedom. As of yet, MSMs have not been used to analyze the coupling between orientational and translational water degrees of freedom, although this coupling has been demonstrated to be crucial for liquid water [126]. Here we employ MSMs to analyze and understand the complex multi-dimensional solvent dynamics without prior definition of what a hydrogen bond is. Indeed, the metastable hydrogen-bonded water structures come out as eigenstates of the transition matrix estimated from the MD data. Based on classical simulation trajectories of liquid pure water at ambient temperature $T = 300$ K, we first in the first part construct a MSM in the full twelve-dimensional configurational space of three water molecules and show that a few slow reconfiguration processes in the ps range can be distinguished and analyzed in terms of the cooperative rearrangements of their H-bond patterns. These slow processes are followed by a quasi-continuum of faster processes with characteristic times below two picoseconds, which is consistent with the experimental finding that water relaxation processes span a wide range of timescales. We next analyze an individual H-bond switching event, defined as the process where a given central water molecule acts as a donor and the accepting H-bond partner switches from one water molecule to a different one. This H-bond switching event has been identified as a central element of H-bond dynamics in liquid water and consequently it has been amply studied [37, 59, 101]. By projection on H-bond states, we perform a full MSM analysis of this H-bond switch scenario and provide the complete transition pathway network and analyze the competing transition probabilities. Here we basically confirm that H-bond switching mostly proceeds without intermediates [37, 59, 101], but also show the strength of our approach by demonstrating the existence of a significant fraction of H-bond switching events that involve intermediate states with alternative or weak H-bonds.

2.2 Methods

2.2.1 Markov state modeling

MSMs describe the complex dynamics of an arbitrary system by a Markovian stochastic process. Relevant degrees of freedom are projected onto a finite number of discrete states and the rates or transition probabilities between different states are described by a transition probability matrix $\mathbf{T}$. From this matrix transition times, transition paths and their probabilities can be extracted [117, 118, 127]. First, the state space has to be partitioned into N states. This is not trivial for a diffusive system like liquid water, since the relevant state space should ideally include only the subset of water molecules that interact with each other, which obviously changes with time. We will later explain how we solve this problem by suitable projection. From a simulated trajectory the $N \times N$ transition probability matrix $\mathbf{T}$ is calculated. The elements T_{ij} describe the

conditional probability of a transition from state i to j within a fixed lag time τ and are estimated by $T_{ij}(\tau) = c_{ij}(\tau)/\sum_j c_{ij}(\tau)$, where $c_{ij}(\tau)$ is the number of transitions from state i to j within time τ and $\sum_j c_{ij}(\tau)$ is the number of transitions from i to any other state within time τ. The matrix is defined in such a way that the sum of every row is unity, thus, it conserves probability. We assume that the transition matrix is ergodic (any state can be reached from any other state within a finite number of steps), which yields a single eigenvector $\boldsymbol{\pi}$ with eigenvalue unity, the stationary distribution. For an MD simulation in equilibrium the detailed balance assumption $\pi_i T_{ij} = \pi_j T_{ji}$ holds. If the N-dimensional vector $\mathbf{p}(t)$ describes the probability distribution at time t, the probability at time $t+\tau$ follows from $\mathbf{p}(t+\tau) = \mathbf{p}(t)\mathbf{T}(\tau)$. The system is Markovian if it fulfills the Chapman-Kolmogorov equation

$$\mathbf{T}(n\tau) = \mathbf{T}^n(\tau). \tag{2.1}$$

The spectral decomposition of the transition matrix according to

$$\begin{aligned}\mathbf{p}(n\tau) &= \mathbf{p}(0)\mathbf{T}^n(\tau) \\ &= \sum_{i=1}^{N} \lambda_i^n (\mathbf{p}(0)\cdot\mathbf{r}_i)\mathbf{l}_i^T \\ &= \sum_{i=1}^{N} e^{-n\tau/t_i^*} (\mathbf{p}(0)\cdot\mathbf{r}_i)\mathbf{l}_i^T,\end{aligned} \tag{2.2}$$

where $\mathbf{r}_i$ and $\mathbf{l}_i^T$ are the $i-$th right and left eigenvectors of the transition matrix, yields characteristic time scales

$$t_i^* = -\frac{\tau}{\ln \lambda_i} \tag{2.3}$$

that are directly related to the eigenvalues λ_i and for a Markovian system are independent of the lag time τ. Eq. (2.2) describes the evolution of the probability density distribution as a weighted superposition of exponentially decaying left eigenvectors. In a nutshell, the construction of a Markov state model requires (i) clustering of the phase space into N states, (ii) estimating the transition matrix from data, and (iii) checking the validity of the Markov model by testing whether the implied time scales depend on the lag time τ, see Sec. 2.5.1 for details.

From the transition matrix transition pathways can be extracted that lead from the subspace of reactant states A to the subspace of product states B and pass through the subspace of intermediate states I. The solution of the linear system of equations

$$-q_i^B + \sum_{k\in I} T_{ik} q_k^B = -\sum_{k\in B} T_{ik} \tag{2.4}$$

defines the committor probability q_i^B, which describes the probability of reaching B before returning to A when being in state i. The flux along the intermediate states i and j which contribute to transitions from A to B is

$$f_{ij} = \pi_i q_i^A T_{ij} q_j^B, \tag{2.5}$$

from which the reaction rate k_{AB} follows as

$$k_{AB} = \sum_{i \in A}^{N} f_{ij} / \left(\tau \sum_{i=1}^{N} \pi_i q_i^A \right). \tag{2.6}$$

The set of states and fluxes creates a transition network, which can be decomposed into individual transition pathways with different probabilities, see Sec. 2.5.2 for details.

2.2.2 Molecular dynamics simulations

The MSM is based on a molecular dynamics (MD) simulation of 895 SPC/E water molecules in a cubic box of edge length $L = 3$ nm with periodic boundary conditions. The trajectories are generated by GROMACS with a Berendsen weak coupling thermostat and barostat with a relaxation time of $t_{\text{rel}} = 1$ ps for a fixed temperature of $T = 300$ K and a pressure of $p = 1$ bar. The time step of the MD simulation is 2 fs, every 20 fs the positional coordinates of every water molecule are stored and the total simulation time is 10 ns. The relative configuration of two water molecules is described by six coordinates: we fix the reference water molecule O* in the coordinate center with its two hydrogens in the $x - y$ plane such that the dipole vector points in the x direction, to describe the configuration of a second water molecule we then have three coordinates for the rotation (α, β, γ), see Fig. 2.1A, and three coordinates for the translation in spherical coordinates (R, ϕ, θ), see Fig. 2.1B. The rotation is described by Euler angles (α, β, γ) in the (z, x', z')-convention: A rotation around the z-axis by the angle α, a rotation around the new x-axis (x') by the angle β and a following rotation by the angle γ around the new z-axis (z'), see Fig. 2.1A. Consequently, for three water molecules the state space is 12-dimensional.

According to the distance-angle criterion [128], an H-bond exists if the distance between two oxygen atoms O* and O^a is $R < 0.35$ nm and the angle between the $\overline{\text{O*H*}}$ and $\overline{\text{O*O}^a}$ vectors is $\angle(\overline{\text{O*O}^a}, \overline{\text{O*H*}}) < 30°$. There are four ways in which two water molecules can establish an H-bond, see Fig. 2.1C for our color coding which we use throughout this paper. In the green and cyan configuration O^a accepts an H-bond from O*, whereas in the orange and red configuration O^a donates an H-bond to O* via H_1^a and H_2^a, respectively.

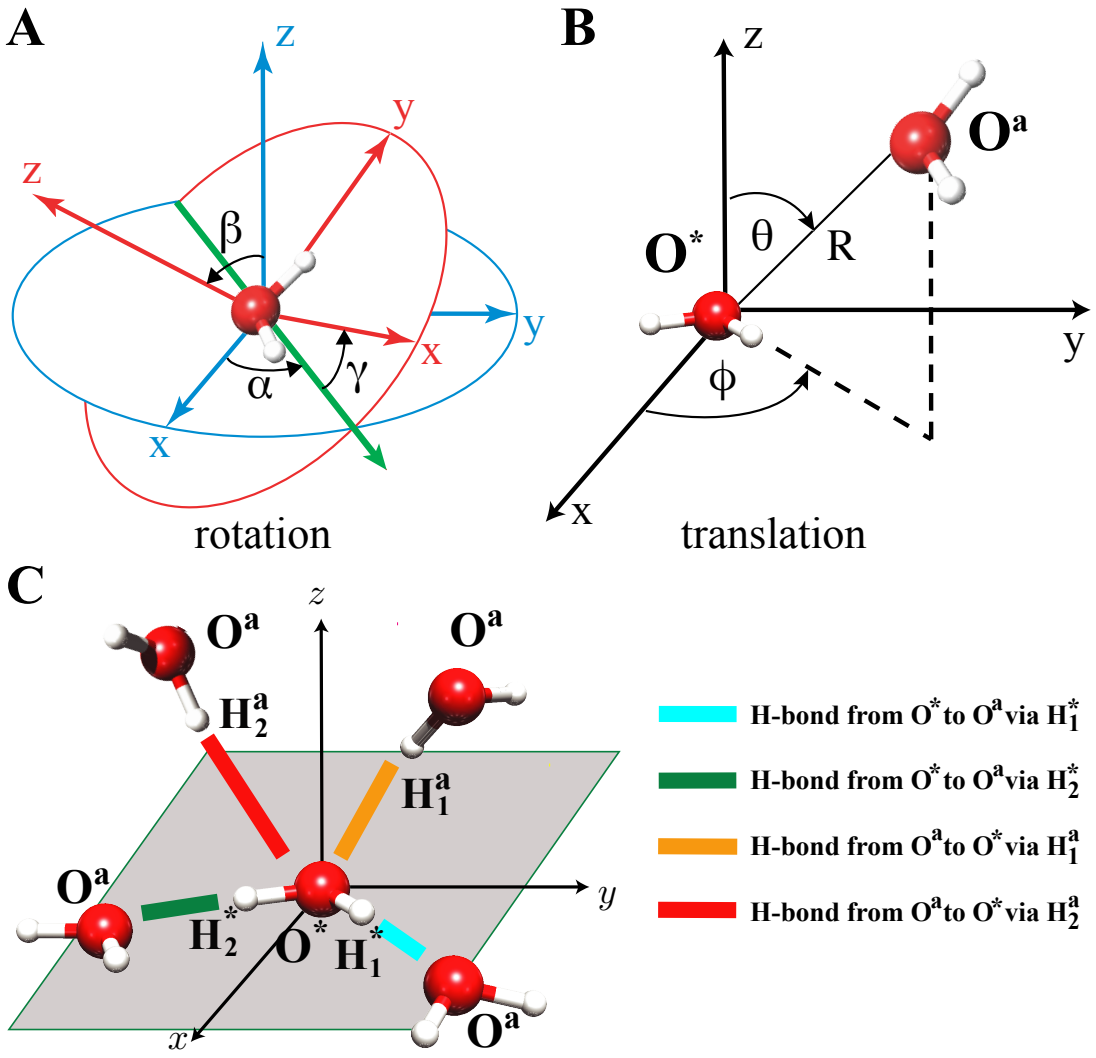

Figure 2.1: **(A)** Euler angles are used for the rotational degrees of freedom and **(B)** spherical coordinates for the translational degrees of freedom. The reference water O* is placed in the coordinate center such that its two hydrogens are located in the $x-y$-plane and the dipole vector points along the x-axis. **(C)** Sketch of different H-bond configurations between two waters. In the cyan configuration O* acts as a donor via H_1^* to O^a, in the green configuration it donates via H_2^* to O^a. In the orange configuration O* accepts an H-bond via H_1^a, whereas in the red configuration it accepts via H_2^a.

2.3 Results and discussion

2.3.1 H-bond rearrangements from three-water MSM

We base our MSM on trajectories of three water molecules, denoted by O*, O^a, and O^b, which are embedded in the liquid water environment. In order to select the set of

considered water molecules we first determine the radial distribution function $g_{OO}(R)$ between water oxygens from which we derive the free energy

$$F(R) = -k_{\mathrm{B}}T \ln\left[g_{OO}(R)\right] - k_{\mathrm{B}}T \ln(R^2), \tag{2.7}$$

depicted in Figs. 2.2A and B. The yellow and green domains correspond to the first and second hydration shells that are separated by a barrier of about $1k_{\mathrm{B}}T$. In previous work we had determined the position-dependent relative diffusivity profile $D(R)$ between two water molecules using the mean first-passage time (MFPT) method, which maps the relative water dynamics onto the generalized Fokker-Planck equation [1]. Our results in Fig. 2.2C show that for small separations around $R = 0.3$ nm the diffusivity $D(R)$ is six times smaller than the bulk value. Previously we had associated the decrease of $D(R)$ with the presence of orthogonal degrees of freedom that we speculated to be related to water orientational dynamics. In Fig. 2.2C we also show the diffusivity profile from our MSM model which results from a projection of the discrete Markov state dynamics onto the separation coordinate R (see Sec. 2.5.3 for details). The good agreement between the results from these two very different methods is a crucial consistency check and in particular demonstrates that the slowed down translational water dynamics in the first hydration shell is indeed caused by the collective motion of water molecules that couples translational and orientational degrees of freedom.

We start recording the 12-dimensional trajectories for the three-water MSM as soon as the radial separation between O* and $\mathrm{O^a}$, $R_{\mathrm{O^*O^a}}$, and between O* and $\mathrm{O^b}$, $R_{\mathrm{O^*O^b}}$, are both < 0.5 nm. We stop recording when one of the two waters leaves the cutoff radius of 0.5 nm, see Fig. 2.3 for a sample trajectory and graphical definition of $R_{\mathrm{O^*O^a}}$ and $R_{\mathrm{O^*O^b}}$. We capture 320,000 trajectories with a total length of 1700 ns and use the k-means++ algorithm [129] with 500 states to cluster states in the 12-dimensional state space. We also varied the number of states in Sec. 2.5.4, but found no advantage of using more than 500 clusters. The transition probability matrix $\mathbf{T}(\tau)$ is estimated for a range of lag times τ and the time scales t_i^* are derived from the eigenvalues of each eigenvector according to Eq. (2.3). In Fig. 2.4A we plot the time scales against the lag time. The merging of time scales below 3 ps is caused by non-Markovian effects due to inertial effects. In the range from 3 to 20 ps the time scales are only weekly dependent on τ and the dynamics can be approximately considered as Markovian, although this is not strictly necessary for our normal mode analysis. The residual dependence on τ in the intermediate time range originates from a combination of projection errors and inertial effects, see [117] for an in-depth discussion. We observe that the slowest time scales are fairly well separated from each other, which suggests a physical interpretation of the associated processes. For $\tau \geq 20$ ps the time scales merge again, which is due to limited sampling at large lag times, see Sec. 2.5.5 for a discussion.

In order to understand the physical meaning of the different processes, we project the 500 components of the eigenvectors onto the underlying 12-dimensional conformational space of the three water molecules, for this we choose a lag time of $\tau = 7$ ps. In Sec. 2.5.6 we demonstrate that the interpretation of the resulting processes is

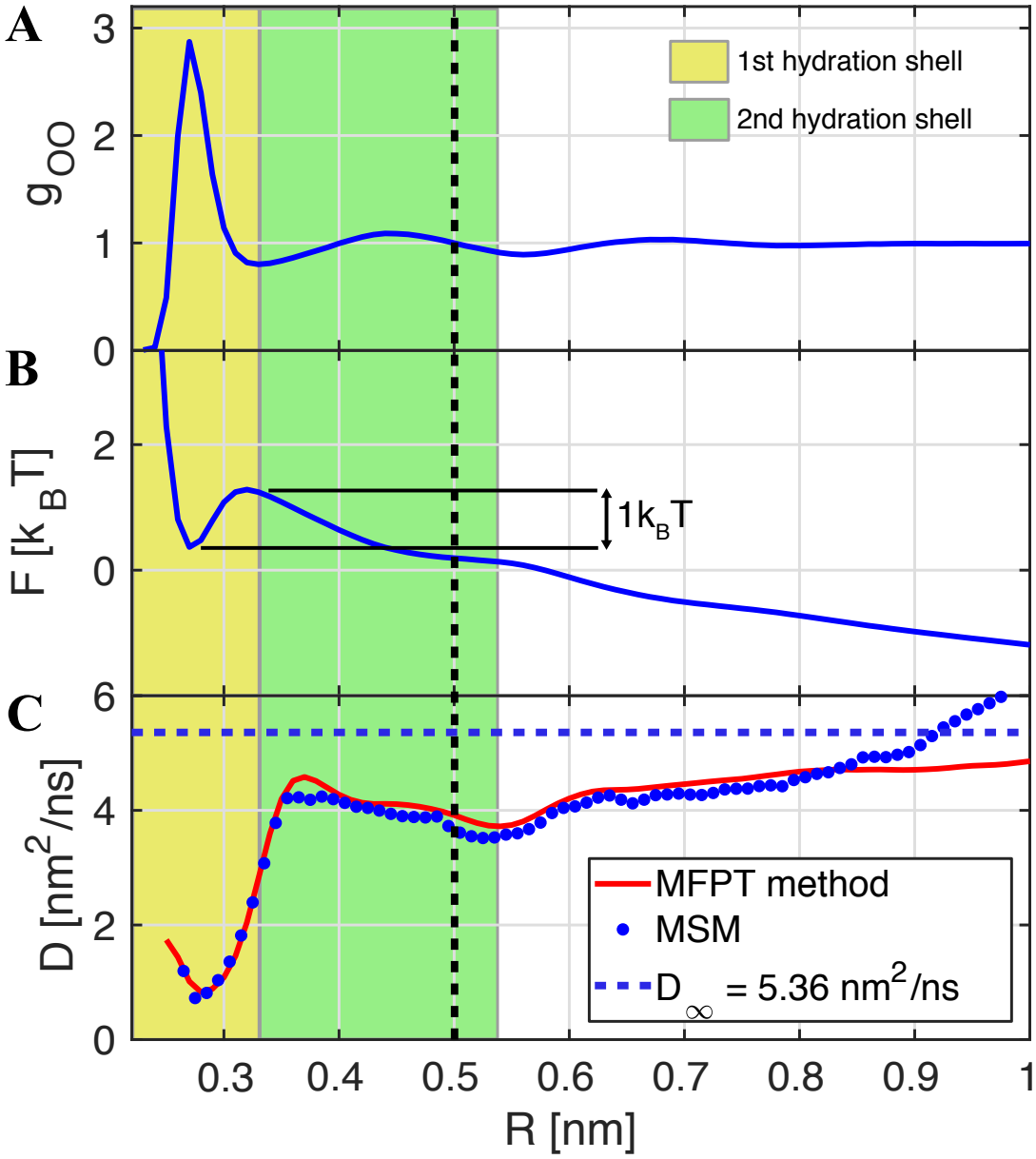

Figure 2.2: **(A)** Radial distribution function $g_{OO}(R)$ between water molecules. $R = 0.5$ nm has been chosen as a cut-off for the selection of trajectories for the three-water MSM. **(B)** Free energy landscape $F(R)$. **(C)** Radial diffusivity profile $D(R)$ between two water molecules. The diffusivity profile calculated from the MSM is consistent with the profile estimated from the mean first-passage time (MFPT) method.

not changed when the lag time is changed to $\tau = 3$ ps or to $\tau = 15$ ps. For clarity we only show the projection onto the angle ϕ for O^a and O^b. The stationary distribution, depicted in Fig. 2.5A, shows pronounced clustering in four bands, at which

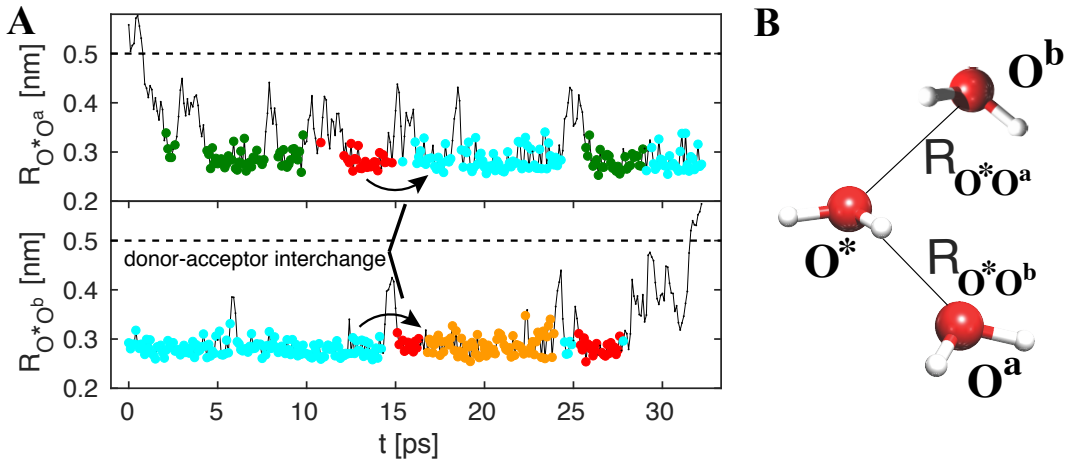

Figure 2.3: **(A)** Trajectories of the radial distances $R_{O^*O^a}$ and $R_{O^*O^b}$ between the oxygen of the central water and the oxygens of two neighboring water molecules. Trajectories are used for constructing the MSM when both distances are smaller than 0.5 nm, this cutoff is denoted by broken horizontal lines. Different colors mark different H-bonds according to the color coding in Fig. 2.1 and visualize H-bond rearrangements. For example, around $t = 15$ ps the O^a water molecules changes from being a donor to being an acceptor, while O^b changes from acceptor to donor. **(B)** Definition of the radial distances $R_{O^*O^a}$ and $R_{O^*O^b}$.

the eigenvector amplitude and thus the distribution probability is markedly enhanced. If we color the eigenvector components according to the H-bond color coding in Fig. 2.1C, we indeed see that these four bands correspond to the four different H-bonds that can form between O* and O^a and between O* and O^b. We stress that our Markov model is constructed in an unbiased fashion and only based on the distances in the 12-dimensional configurational space, but that the resulting state clusters can a posteriori be straightforwardly associated with H-bonds.

The slowest process with a time scale $t_1^* = 6.1$ ps is depicted in Fig. 2.5B. The eigenvector contains negative components, which describe a loss of probability, and positive components, which describe a gain of probability, and thus corresponds to a transition in configurational space. Interpretation of this transition is possible by projection on H-bonds, visualized by our color coding: For O^a the green and cyan H-bond configurations (in which O* donates to O^a) are predominantly negative, whereas the red and orange H-bond configurations (in which O* accepts from O^a) are positive. For O^b we observe the opposite, the red and orange configurations are negative and the green and cyan configurations are positive. This means that the slowest time scale is caused by a transition where in the initial configuration O^a accepts an H-bond from O* and O^b donates an H-bond to O*, while in the final configuration O^b accepts an H-bond from O* and O^a donates an H-bond to O*, as illustrated at the bottom of Fig. 2.5B (note that the reverse process is of course described by the same eigenvector with a negative amplitude). This process thus describes the interchange of donor and acceptor position of O^a and O^b and is named donor-acceptor interchange. This process is achieved by a

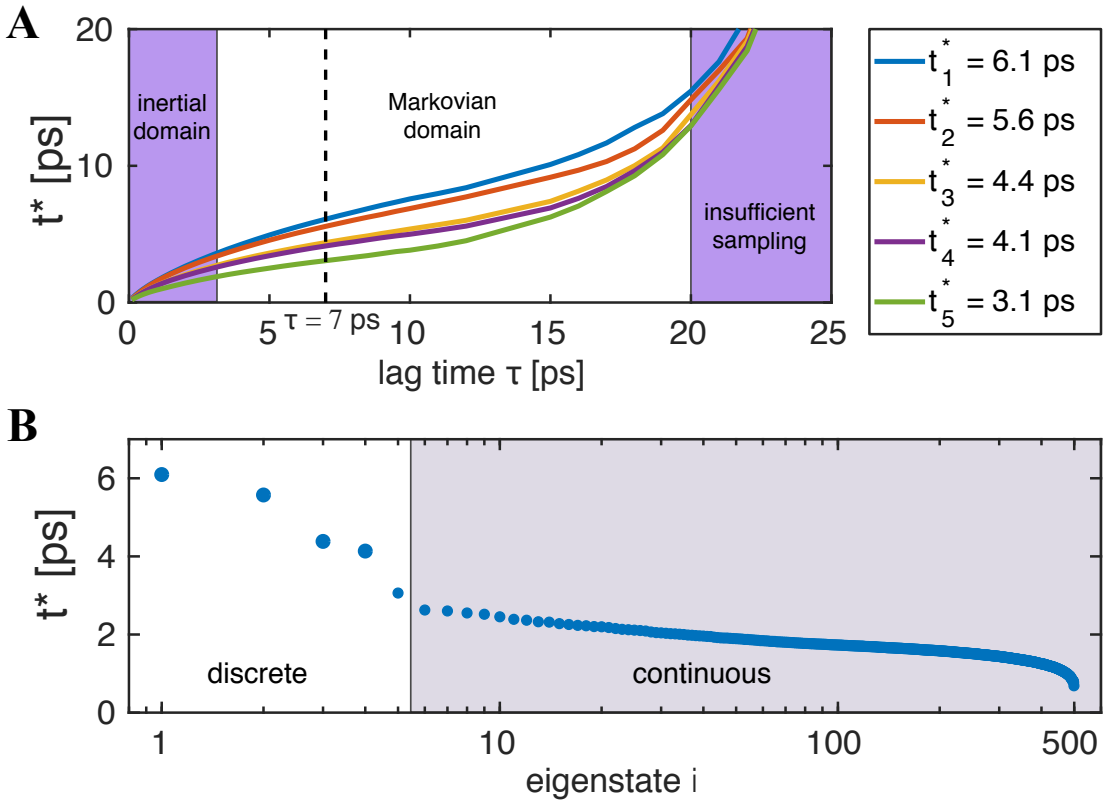

Figure 2.4: **(A)** Plot of the five slowest time scales t_i^* versus the lag time τ for the three-water MSM. **(B)** Plot of all time scales for fixed lag time $\tau = 7$ ps. The five slowest time scales are separated from a continuum.

concerted rotation of all three water molecules and occurs in the trajectory in Fig. 2.3 around $t = 15$ ps, where water O^a changes from red to cyan (donating $\rightarrow$ accepting), whereas O^b changes from cyan to red (accepting $\rightarrow$ donating). Note that this process presumably involves other water molecules as well, which however will not modify the extracted time scale and the eigenvector components shown in Fig. 2.5B. This robustness of our three-water MSM is vividly demonstrated by the fact that even a more restricted two-water MSM yields the same time scales, as shown in Sec. 2.5.7.

The second slowest process with a time scale of $t_2^* = 5.6$ ps, depicted in Fig. 2.5C, describes an acceptor-acceptor interchange. Here the dominant negative part of the O^a eigenvector in cyan describes an initial state where the central water O* donates an H-bond, whereas O^b is initially described by the green configuration where the central water O* also donates an H-bond. In the final configuration O^a and O^b have interchanged positions. Thus, this process is an acceptor-acceptor interchange, which can be achieved by a single rotation of the central water O* by $180°$ around its dipole axis. In the third slowest process with $t_3^* = 4.4$ ps in Fig. 2.5D, both waters O^a and O^b initially donate H-bonds to O* (negative orange and red eigenvector components),

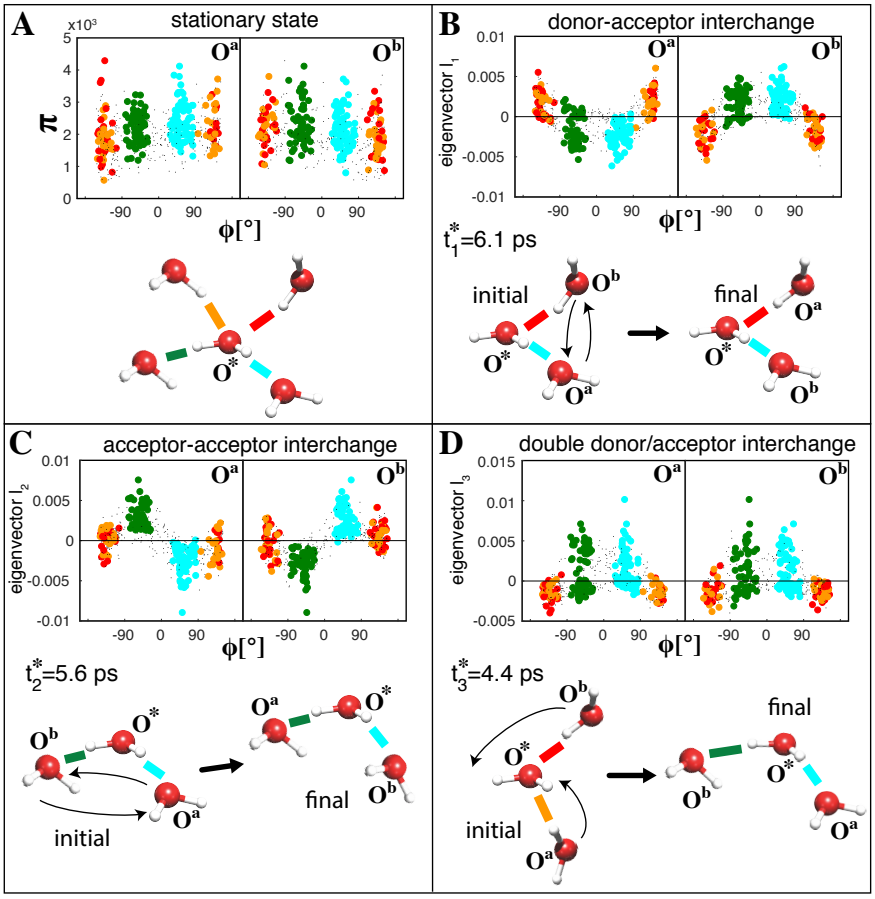

Figure 2.5: Equilibrium state and the three slowest hydrogen-bond interchange processes of the three-water MSM. We show the projection of the eigenvector onto the angle ϕ for the water pairs $O*-\mathrm{O^a}$ and $O*-\mathrm{O^b}$. Colored eigenvector components denote H-bonds according to the definition shown in (A). **(A)** The equilibrium state consists of a combination of H-bonds between O* and the waters $\mathrm{O^a}$ and $\mathrm{O^b}$. **(B)** The eigenvector associated with the slowest time scale $t_1^* = 6.1$ ps describes a donor-acceptor interchange, where $\mathrm{O^a}$ and $\mathrm{O^b}$ interchange their roles as acceptor and donor. This process is achieved by a collective rotation of all three waters O*, $\mathrm{O^a}$, and $\mathrm{O^b}$. **(C)** Acceptor-acceptor interchange with a time scale of $t_2^* = 5.6$ ps. Here O* donates H-bonds to both waters $\mathrm{O^a}$ and $\mathrm{O^b}$ via its two H-atoms in the initial and final states. This process is achieved by a single rotation of the central water molecule O*. **(D)** Double donor/acceptor interchange with a time scale of $t_3^* = 4.4$ ps. In the initial state O* accepts two H-bonds from $\mathrm{O^a}$ and $\mathrm{O^b}$, in the final state $\mathrm{O^a}$ and $\mathrm{O^b}$ accept H-bonds from O*.

whereas in the final state both waters accept H-bonds from O* (predominantly positive blue and cyan eigenvector components). This transition can be achieved by a concerted rotation of all three water molecules and corresponds to a double donor/acceptor interchange. The faster processes become more and more difficult to interprete since they do not allow for a clear cut interpretation in terms of H-bond patterns.

We conclude that our three-water MSM unambiguously reveals the slowest H-bond rearrangement patterns in a water trimer that is embedded in liquid water. The re-

sultant slowest time scales are in the range of $4 - 6$ ps and thus considerably slower than the typical librational time scale of $t_{\text{libr}} \sim 200$ fs [38, 47, 130] or the reorientational time scale of $t_{\text{reorient}} \sim 2.5$ ps it takes a H-bond donating water to switch from one to a different acceptor [37, 47, 59, 102, 131]. This is not difficult to rationalize, since the three processes presented in Fig. 2.5 involve the breaking and reformation of at least two H-bonds. For the second slowest process with $t_2^* = 5.6$ ps in Fig. 2.5C the H-bond arrangement can proceed via the rotation of a single water molecule, for the slowest and third slowest processes in Fig. 2.5B and D the arrangement involves the concerted reconfiguration of the entire water trimer. In photon-echo experiments [113] it was found that a comparatively slow time scale in the 5 - 15 ps range exists that is related to H-bond rearrangements. In agreement with these experiments, our findings suggest an entire set of slow dynamic collective water modes that lie in this time range. It is interesting that the single water rotation mode in Fig. 2.5C has almost the same time scale as the other two concerted rotation transitions in Fig. 2.5B and D, and that all three modes describe very different structural rearrangements of the H-bonding pattern within the water trimer. This vividly demonstrates why the interpretation of the microscopic water dynamics is so complex, even when simulation trajectories with full configurational information are available. It would be hard to extract the dynamical modes shown in Fig. 2.5 from the simulation trajectories without the MSM analysis. In Sec. 2.5.7 we show that a restricted MSM for a water dimer gives quite similar slow time scales but obviously does not allow to interpret the kinetic processes in terms of collective H-bond reconfigurations. This shows that the resulting time scales of the water MSM are robust with respect to the number of water molecules the MSM is based upon.

2.3.2 Transition paths for H-bond acceptor switching

In the previous section, we analyzed the slowest elementary processes that occur in a three-water MSM and showed that they correspond to the simultaneous breaking and reforming of at least two H-bonds. In this section we consider a somewhat simpler scenario, namely the switching of a single H-bond from one accepting water molecule to a different accepting water molecule. In fact, the mechanism and the transition pathway of this H-bond switching event have been challenging topics of research for decades [57]. In [58] it has been shown via transition path sampling that in roughly half of the cases when an H-bond is broken, a new H-bond forms right after. In [37, 59] it has been shown that this H-bond switch is dominated by an abrupt angular rotation of the central water molecule that acts as a donor. Here we will bring these two findings in harmony to each other and in particular will analyze the complete transition network that describes the switching of a single H-bond acceptor.

In order to describe the switching event of a single H-bond acceptor by a MSM we modify the selection rule for trajectories and project onto a much restricted set of states. We now consider trajectories where O* is H-bonded to a water O^a via its hydrogen atom H_1^* initially and switches to a different water O^b to which it forms an H-bond via

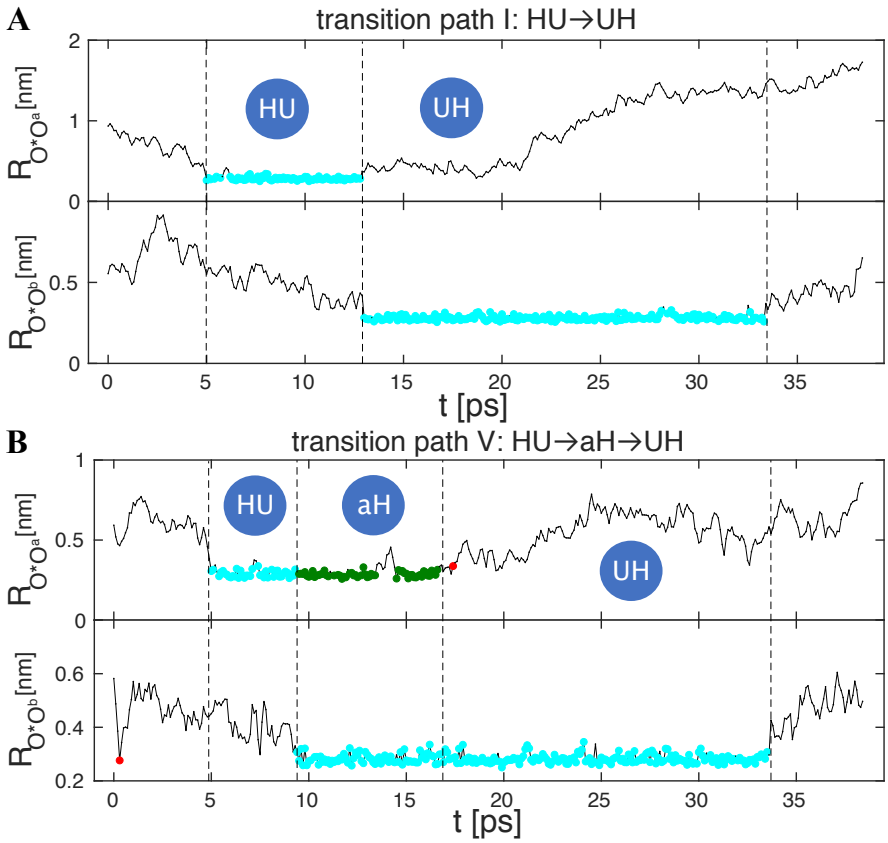

Figure 2.6: Sample trajectories of H-bond switching events in terms of the radial distances R_{O*O^a} and R_{O*O^b} between three water molecules. (**A**) At $t = 5$ ps an H-bond (cyan color) between O* and O^a is formed for the first time. At $t = 13$ ps this H-bond between O* and O^a is broken and immediately switches to O^b. After this, O^a diffuses away from O* while O* and O^b stay H-bonded until the H-bond is finally broken at $t = 34$ ps. This process is an example for the direct transition path type I, see Fig. 2.7C. **(B)** At $t = 5$ ps an H-bond (cyan color) between O* and O^a is formed for the first time. At $t = 9$ ps this H-bond switches to O^b and O^a forms an alternative H-bond with O* where it accepts a different hydrogen from O* (denoted by green color) until it diffuses away at $t = 16.5$ ps. This process is an example of transition path type V, see Fig. 2.7C. The color notation of H-bonds is defined in Fig. 2.1.

the same hydrogen H_1^*. We start recording trajectories as soon as O* and O^a become H-bonded under the condition that no H-bond between O* and O^b exists and stop when the H-bond between O* and O^b is broken finally, see Fig. 2.6A and B for two example trajectories.

We collect a total of 199,197 H-bond switching events and define four basis states which describe the H-bond configuration between two water molecules. In the H-bonded state, called H, the central water molecule O* forms an H-bond with water molecule O^x by donating its hydrogen H_1^*, where the O^x stands for water O^a or O^b. In the unbound state, called U, there is no H-bond between O* and O^x and the radial distance between the waters is $R_{O*O^x} > 0.35$ nm, which exceeds the threshold

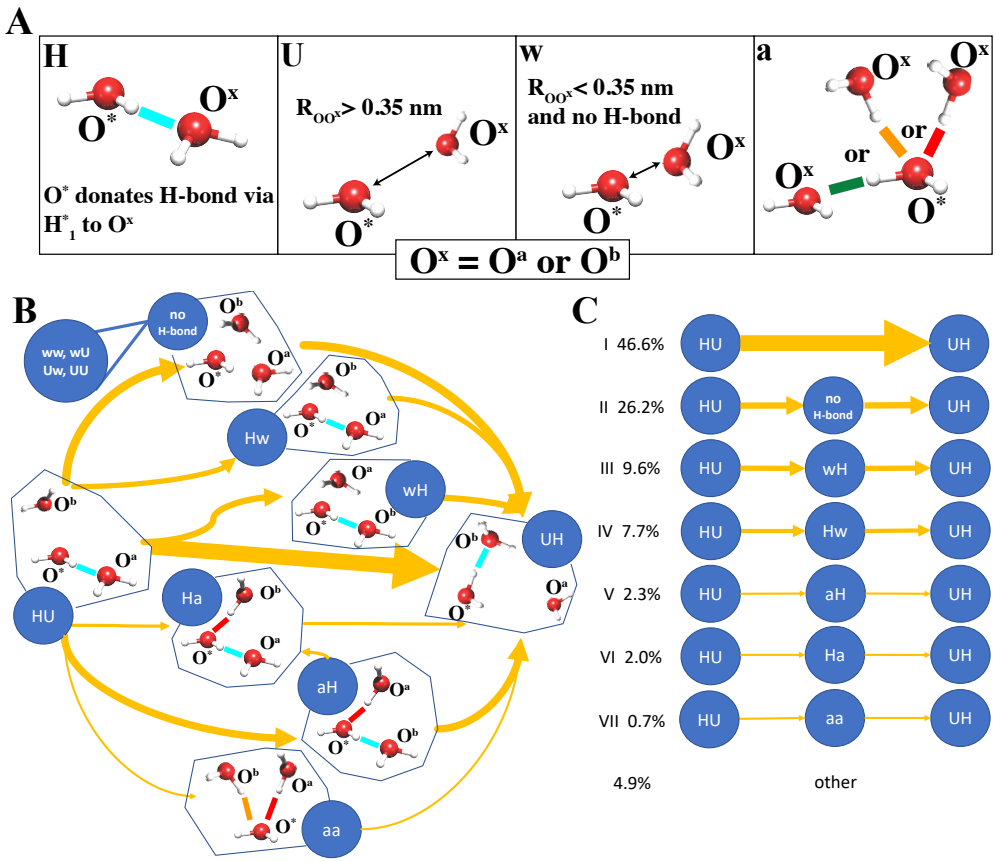

Figure 2.7: **(A)** The four basis states describing the bonding state between O* and a second water molecule O^x. **(B)** Transition network for the H-bond acceptor switching, showing only the eight dominant pathways, the thickness of arrows indicates the net-flux. In the reactant state HU, O* acts as an H-bond donor to O^a via H_1^*, while no H-bond with O^b is present and the distance between O* and O^b is larger than 0.35 nm. In the product state UH, O* acts as a H-bond donor to O^b via the same hydrogen H_1^*, while no H-bond with O^a is present and the distance between O* and O^a is larger than 0.35 nm. **(C)** Transition pathwayss ordered by their probabilities. Pathways with probability lower than 0.5% are not shown.

separation for an H-bond. In the weakly bounded state, called w, there is no H-bond because the angular criterion is not fulfilled, but the distance between the two waters is $R_{O*O^x} < 0.35$ nm. In the alternative H-bond state, called a, the water molecule O* either accepts an H-bond from O^x or it forms an H-bond with O^x by donating its other hydrogen H_2^* to O^x, see Fig. 2.7A for an illustration of these four states. The combinations of these four basis states yields $4 \times 4 = 16$ MSM cluster states for three water molecules O*, O^a, and O^b.

In the reactant state O* and O^a are in state H whereas O* and O^b are in state U, which we denote as HU (i.e. the first letter denotes the bonding state between O* and O^a and the second letter denotes bonding state between O* and O^b). The product state is defined as UH where water molecules O^a and O^b have exchanged their roles, see

Fig. 2.7B. The validity of the defined MSM for a lag time of $\tau = 1$ ps is discussed in Sec. 2.5.8. We calculate the committor probabilities according to Eq. (2.4), the transition rate turns out to be $k_{\mathrm{HU}\to\mathrm{UH}} = 0.24$ ps^{-1} according to Eq. (2.6). This yields a reaction or mean first-passage time of

$$\tau_{\mathrm{m}fp} = 1/k_{\mathrm{HU}\to\mathrm{UH}} = 4.2 \text{ ps}. \tag{2.8}$$

This mean first-passage time is smaller than the previously published estimate of the H-bond life time of $\tau_{\text{HB-life}} = 6.5$ to 7.0 ps [37, 100], but larger than the previously calculated H-bond switching time $\tau_{\text{HB-switch}} = 3.3$ ps, see Ref. [37, 59] and Sec. 2.5.8. Note that the difference between the H-bond life time and H-bond exchange time follows from the fact that after an H-bond exchange another H-bond exchange can occur, leading back to the initially H-bonded configuration, see also Ref. [37] for details. As a consequence, our reaction time $\tau_{\mathrm{m}fp}$ includes the diffusion of O^b towards O* and of O^a away from O* and is therefore a bit larger than the H-bond switching time. The resultant time scale is similar to the time it takes two water molecules to diffuse from the first to the second hydration shell, which ranges between 4 to 12 ps depending on the target distance in the second hydration shell, see Ref. [1].

The 16 states and the fluxes defined by Eq. (2.5) create a transition network, which can be decomposed into competing pathways that are characterized by different transition probabilities, see Sec. 2.5.2 for the detailed derivation. We show the complete transition network in Fig. 2.7B. The thickness of the arrows indicates the net flux. States which contribute with a net flux close to zero have been omitted, as a consequence of this the transition network in Fig. 2.7B shows only 11 of the 16 possible states defined by the MSM. As the most important result, we find that competing pathways for the H-bond switching exist. The main transition pathway I with a probability of 46.6% is the direct transition path HU→UH, where O* switches its donating hydrogen from O^a to O^b without an intermediate state (on the time scale set by the lag time of $\tau = 1$ ps). The transition pathways III and IV involve the weakly bound state w, where O^a or O^b is in an intermediate state found at a separation $R < 0.35$ nm. The three transition pathways I, III, and IV sum up to about two thirds of all possible transitions, they describe a direct H-bond switch between the two accepting water molecules and thus correspond to the pathway described by Laage et al. [37, 59] and indeed constitute the predominant pathway for H-bond switching in agreement with [58].

However, the second important pathway II consists of a short-lived intermediate state which can be of the ww, wU, Uw, or UU type, and has a probability of 26.2%. The other group of pathways, V,VI, and VII, involve intermediate states where O* forms an alternative H-bond with O^a or O^b, they sum up to a total probability of 5.0%. An example of a trajectory of type IV is shown in Fig. 2.6B, where the O^a water does not immediately diffuse away from O* after breaking its initial H-bond with O*, but rather stays H-bonded to O* via an alternative H-bond. Together, all pathways where the H-bond does not switch directly from O^a to O^b make up about one third of all switches, and thus are not negligible. Clearly, by extracting averaged coordinates during H-bond switches from simulation trajectories or by looking at dominant transition path

ways from transition path sampling, such subdominant alternative pathways are easily overlooked.

2.4 Conclusions

We use Markov state modeling for the analysis of liquid water structurual dynamics based on classical molecular dynamics simulations. In the first part we consider water dynamics in the full 12-dimensional continuum space of a water trimer that is embedded in liquid water and identify the slowest dynamic processes and relate them to dynamical rearrangements of H-bond patterns. The three slowest processes consist of the breaking and reforming of at least two H-bonds and correspond to donor-acceptor, acceptor-acceptor and double donor/acceptor interchanges. Interestingly, the second slowest process, the acceptor-acceptor interchange, corresponds to the rotation of a single water molecule, while the donor-acceptor and double donor/acceptor interchanges involve the concerted rotation of all three water molecules. This means that slow water processes consist of either collective (like the slowest and third-slowest process in Fig. 2.5B and C) or single-water reorientation processes (like the second-slowest process in Fig. 2.5C). In the second part we formulate the MSM in a much restricted state space that results from a prior H-bond projection. Using transition path analysis we classify all possible pathways describing the H-bond switching from one accepting water molecule to a second accepting water molecule. The dominant transition pathways correspond to a direct transition to the new H-bond acceptor without a broken H-bond as an intermediate state, which make up about 66% of all transitions and have been investigated before [37, 58, 59]. A non-H-bonded intermediate occurs in the transition pathway in about 26% of all transitions while in 5% of all transitions an alternative H-bond arrangement occurs in the intermediate state. We conclude that the dominant transition pathways we find for the single H-bond switch are consistent with previous results but that MSMs allow to draw a more complete picture of the H-bond reconfiguration dynamics.

In previous quantum calculations the concerted breaking and reforming of H-bonds in isolated water clusters at zero temperature has been characterized [114–116]. These studies suggest that H-bond rearrangements are local and do not involve more than three water molecules [115]. Nevertheless, it would be interesting to extend MSMs to tetramers or pentamers in order to check whether concerted H-bond rearrangements that involve more than three water molecules exist in the liquid state. Our simulation trajectories are obtained from classical force field simulations and neglect the quantum nature of nuclei motion, which is an acceptable approximation at the time scale we are probing [132, 133]. Effects from suboptimal force fields are presumably more critical, which is an issue we leave for future studies.

As a final note we would like to discuss whether the occurrence of abrupt angular jumps is in conflict with Debye's diffusive model. As briefly mentioned in the introduction, the presence of an angular free energy barrier predicts a transition path time

that is much shorter than the H-bond life time [106–108]. Explicitly, the mean-first passage time to cross a harmonic barrier of angular width L is for large barrier height U given by [108]

$$\tau_{\mathrm{m}fp} = \frac{\sqrt{\pi} L^2 e^{U/k_B T}}{8D(U/k_B T)^{3/2}}, \tag{2.9}$$

where D is the effective angular diffusion constant along the angular reaction coordinate. In contrast, the transition path time, that means the actual duration of the path that crosses the barrier, is for large barrier height U given by [108]

$$\tau_{\mathrm{t}p} = \frac{\sqrt{\pi} L^2 \ln(2e^{\gamma} U/k_B T)}{8DU/k_B T}, \tag{2.10}$$

where $\gamma = 0.577$ is the Euler gamma constant, and only logarithmically depends on the barrier height. The ratio of the transition path and the mean-first passage time is given by [106]

$$\tau_{\mathrm{t}p}/\tau_{\mathrm{m}fp} = \frac{\ln(2e^{\gamma} U/k_B T)(U/k_B T)^{1/2}}{\sqrt{\pi} e^{U/k_B T}} \tag{2.11}$$

which for a rescaled barrier height $U/k_B T = 4$ takes a value of $\tau_{\mathrm{t}p}/\tau_{\mathrm{m}fp} = 0.05$. This means that even for a moderate barrier height the angular transition is rather short and thus abrupt compared with the hydrogen bond life time, which does not invalidate the Debye diffusive picture but rather shows that free-energetic barrier effects must be taken into account.

2.5 Supporting Information

2.5.1 Constructing Markov state models

Markov state models allow to describe the complex dynamics occurring in a MD-simulation by a Markov chain - a stochastic process without memory effects. In order to achieve this, the entire dynamics is projected onto a number of discrete states where fast processes are projected out. The rates or transition probabilities between different states are governed by a transition probability matrix

$$\mathbf{T}(\tau) = \begin{pmatrix} T_{11} & T_{12} & \cdots & T_{1N} \\ T_{21} & T_{22} & \cdots & T_{2N} \\ \vdots & \vdots & & \vdots \\ T_{N1} & T_{N2} & \cdots & T_{NN} \end{pmatrix}, \tag{2.12}$$

where the elements $T_{ij}(\tau)$ describe the conditional probability of a transition from state i to j within a lag time τ. Once this matrix has been estimated, different processes,

transition paths, and probabilities can be extracted and ordered by the time scale t^* of each process. We give a brief overview of the concept of Markov state models in this section and refer the reader to [117, 118, 127] for more details.

The phase space $\Omega(\mathbf{q}, \tilde{\mathbf{q}})$ of a system consisting of N atoms yields a $6N$-dimensional state space spanned by the positional $\mathbf{q}$ and momentum $\tilde{\mathbf{q}}$ degrees of freedom. The process $\{\mathbf{x}_t\}_{t\in\mathbb{R}}$, where $\mathbf{x}_t = \mathbf{x}_t(\mathbf{q}, \tilde{\mathbf{q}})$, describes a trajectory in phase space, which is completely deterministic when considering a MD-simulation in the NVE ensemble and knowing the initial configuration. Solving the Liouville equation

$$\frac{\partial \rho}{\partial t} = -\mathcal{L}\rho = \sum_{i=1}^{n} \left[\frac{\partial H}{\partial \tilde{q}_i} \frac{\partial}{\partial q_i} - \frac{\partial H}{\partial q_i} \frac{\partial}{\partial \tilde{q}_i} \right] \rho \tag{2.13}$$

for a given Hamiltonian H yields the complete information at any time t. We further assume the process is homogeneous in time and reversible, in particular it fulfills detailed balance. The evolution within time τ is given by the formal solution of Eq. 2.13

$$\rho(\mathbf{q}, \tilde{\mathbf{q}}, t + \tau) = e^{\mathcal{L}\tau} \rho(\mathbf{q}, \mathbf{q}, t) = \mathcal{P}(\tau)\rho(\mathbf{q}, \tilde{\mathbf{q}}, t) \tag{2.14}$$

where the propagator $\mathcal{P}(\tau) = e^{\mathcal{L}\tau}$ contains the entire information about the dynamics of the system. The propagator can be estimated by a projection onto a low-dimensional and finite state space, where usually all momentum degrees of freedom are neglected, see Fig. 2.8 for an illustration. The projection is typically not exact anymore, but the dynamics one is interested in will not be changed significantly if the projection is performed suitably. Since we simplified the dynamics from continuous to discrete state space the propagator $\mathcal{P}(\tau)$ reduces to the transition matrix

$$\mathcal{P}(\tau) \to \mathbf{T}(\tau). \tag{2.15}$$

This matrix is defined such a way, that the sum of every row is 1, which describes the conservation of probability. This kind of matrix is called *row-stochastic*. The evolution of a density distribution reads then as

$$\mathbf{p}^T(t + \tau) = \mathbf{p}^T(t) \cdot \mathbf{T}(\tau), \tag{2.16}$$

where $\mathbf{p}^T$ denotes the transpose of $\mathbf{p}$ and the phase space density ρ is reduced to a (normalized) probability vector $\mathbf{p}(\tau)$. Eq. 2.16 implies the following identity

$$\mathbf{T}(n\tau) = \mathbf{T}^n(\tau) \tag{2.17}$$

known as the *Chapman-Kolmogorov* equation. Whenever a stochastic process fulfills Eq. (2.17) the process is Markovian and depends only on the current configuration. The transition matrix is estimated by

$$T_{ij}(\tau) = \frac{c_{ij}(\tau)}{\sum\limits_j c_{ij}(\tau)}, \tag{2.18}$$

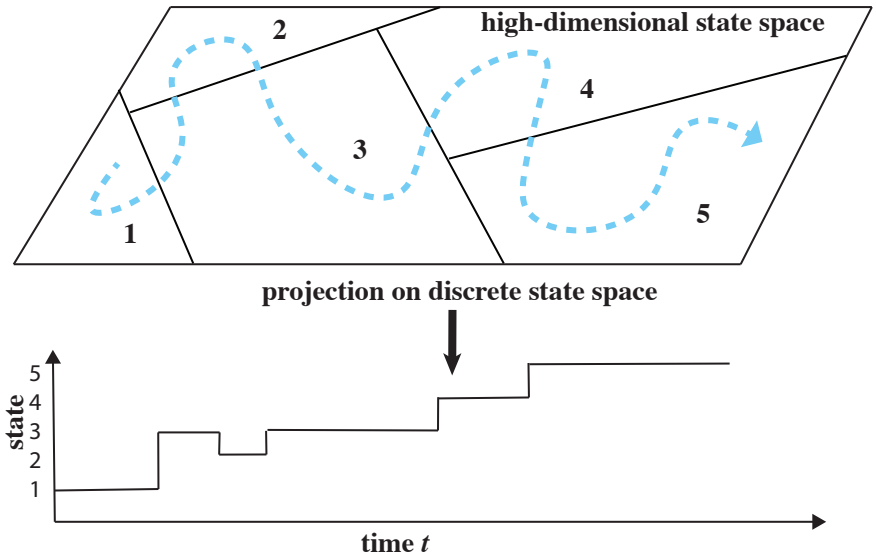

Figure 2.8: **Clustering of state space.** Schematic trajectory in 6N-dimensional phase state space. Here, the entire state space has been partitioned into only five clusters which cover the complete state space.

where c_{ij} is the frequency of jumps from state i to j within time τ and $\sum_j c_{ij}(\tau)$ is the frequency of jumps from i to any other state j within lag time τ.

Once a transition matrix has been estimated, a spectral decomposition yields different time scales and processes associated to these time scales.

Spectral decomposition

The eigenvectors and eigenvalues of the transition matrix provide useful information about the processes that govern the system dynamics. For a $N \times N$ matrix we always can obtain a left $\mathbf{l}$ and a right $\mathbf{r}$ eigenvector to the same eigenvalue:

$$\mathbf{T}\mathbf{r}_i = \lambda_i \mathbf{r}_i \tag{2.19}$$

$$\mathbf{l}_i^T \mathbf{T} = \mathbf{l}_i^T \lambda_i, \tag{2.20}$$

where the i denotes the i-th eigenvector. Further it is assumed that the matrix is diagonalizable and we define the following vectors and matrices.

$$\mathbf{\Lambda} = \begin{pmatrix} \lambda_1 & & 0 \\ & \ddots & \\ 0 & & \lambda_N \end{pmatrix} = \mathrm{diag}(\lambda_1, \ldots, \lambda_N) \tag{2.21}$$

$$\mathbf{R} = \begin{pmatrix} \mathbf{r}_1 & \ldots & \mathbf{r}_N \end{pmatrix} \tag{2.22}$$

$$\mathbf{L} = \begin{pmatrix} \mathbf{l}_1^T \\ \vdots \\ \mathbf{l}_N^T \end{pmatrix}, \tag{2.23}$$

where $\mathbf{\Lambda}$ is the diagonalized matrix of $\mathbf{T}$, containing all eigenvalues on the diagonal. $\mathbf{R}$ contains all right eigenvectors, and $\mathbf{L}$ all left eigenvectors. The decomposition of the transition matrix is then given by

$$\begin{aligned} \mathbf{T} =& \mathbf{R}\mathbf{\Lambda}\mathbf{R}^{-1} && (2.24)\\ =& \mathbf{L}^{-1}\mathbf{\Lambda}\mathbf{L} && (2.25)\\ =& \mathbf{R}\mathbf{\Lambda}\mathbf{L} && (2.26)\\ =& \sum_{i=1}^{N} \lambda_i \mathbf{r}_i \otimes \mathbf{l}_i^T, && (2.27) \end{aligned}$$

where we used $\mathbf{R}\mathbf{R}^{-1} = \mathbf{L}\mathbf{L}^{-1} = \mathbf{R}\mathbf{L} = \mathbf{1}$. With this decomposition we are able to describe the evolution of the probability density distribution as the superposition of eigenvectors

$$\begin{aligned} \mathbf{p}(n\tau) &= \mathbf{p}(0)\mathbf{T}^n(\tau) \\ &= \sum_{i=1}^{N} \lambda_i^n (\mathbf{p}(0) \cdot \mathbf{r}_i)\mathbf{l}_i^T \\ &= \sum_{i=1}^{N} e^{-\frac{n\tau}{t_i^*}} (\mathbf{p}(0) \cdot \mathbf{r}_i)\mathbf{l}_i^T, \end{aligned} \tag{2.28}$$

where we used $\mathbf{T}^n = \mathbf{R}\mathbf{\Lambda}^n\mathbf{L}$. Thus, the evolution is given by summing every left eigenvector weighted by a scalar $(\mathbf{p}(0) \cdot \mathbf{r}_i)$ and the n-th power of each eigenvalue. We assume the matrix fulfills detailed balance

$$\pi_i T_{ij} = \pi_j T_{ji}, \tag{2.29}$$

where $\boldsymbol{\pi}$ is the stationary distribution of $\mathbf{T}$, which is the (normalized) left eigenvector to $\lambda = 1$. Every other eigenvalue is real-valued in the interval

$$-1 < \lambda < 1. \tag{2.30}$$

The eigenvectors reveal information about the processes. From Eq. (2.28) we can read off the time scale of each process, which is directly related to the eigenvalue

$$\lambda_i^n(\tau) = e^{n\ln(\lambda_i(\tau))} = e^{-\frac{n\tau}{t_i^*}}. \tag{2.31}$$

For a perfect Markov state model this time scale is independent of the lag time τ, since

$$\begin{aligned} t_i^*(\tau) &= -\frac{\tau}{\ln\lambda_i(\tau)} = -\frac{n\tau}{n\cdot\ln(\lambda)} = -\frac{n\tau}{\ln(\lambda_i^n(\tau))} \\ &= -\frac{n\tau}{\ln(\lambda_i(n\tau))} = t_i^*(n\tau) = \text{const.}, \end{aligned} \tag{2.32}$$

where we used $\lambda^n(\tau) = \lambda(n\tau)$ which follows directly from the Chapman-Kolmogorov Eq. (2.17). The fact, that the time scale should be independent of the lag time, is a useful tool to check if Eq. (2.17) is fulfilled, since it is rather cumbersome to compare transition matrices estimated at different lag times. However, when estimating transition matrices by counting transitions from one state to another, the time scales are not necessarily independent of the lag time since the model relies crucially on the defined state space and the sampling. In particular, (i) for small lag times the inertia of the massive particles dominates and leads to non-Markovian effects, (ii) insufficient selection/projection of states can lead to memory effects as well, and (iii) for large lag times, typically larger than the largest time scale, sampling issues arise, see also Sec. 2.5.5.

In a nutshell the steps for the construction of a Markov state model can be summarized as follows.

i) Clustering. First, the state space needs be clustered into a predefined number N of clusters. For this a *cluster center* needs to be assigned. Every point of the trajectory which is inside the cluster will be assigned to the cluster center. There are numerous methods how to cluster. A prominent algorithm we use is called k-means++ [129], where the functional

$$J = \sum_{i=1}^{N} \sum_{\mathbf{x}_j \in S_i} \|\mathbf{x}_j - \mu_i\|^2 \tag{2.33}$$

is minimized, $\mathbf{x}_j$ represents the j-th component of the trajectory, μ_i is the i-th cluster center of a total of N cluster centers and S_i represents the i-th cluster. If the data contains variables of incomparable units then the data can be standardized before performing the clustering.

ii) Estimation. The transition matrix is estimated from a long or many short trajectories by

$$T_{ij}(\tau) = \frac{c_{ij}(\tau)}{\sum\limits_j c_{ij}(\tau)}, \tag{2.34}$$

where $c_{ij}(\tau)$ is the frequency of jumps from state i to j within lag time τ and $\sum_j c_{ij}(\tau)$ is the frequency of jumps from i to any state within time τ.

iii) Markovianity check. The system can be assumed Markovian when fulfilling the Chapman-Kolmogorov equation Eq. (2.17). This is conveniently achieved by estimating transition matrices for different lag times τ and calculating the slowest time scales t_i^*. The Markovianity is given when t_i^* becomes independent of the lag time.

2.5.2 Transition paths

The concept of transition path theory (TPT), allows us to derive the probability to observe a certain transition pathway for a reactant and product state.

We derive the key quantities in order to find every possible pathways and its associated probability. We follow the excellent derivation in [64, 134, 135].

Given is the $N \times N$ transition matrix $\mathbf{T}(\tau)$ defined in Eq. (2.12) and the set of all cluster states N_{clust}, consisting of in total N states, which are partitioned into the subsets A, B, and I, where

$$\begin{aligned} A &= \text{reactant state} \\ B &= \text{product state} \\ I &= \text{intermediate states.} \end{aligned}$$

Transitions occur from the reactant state A to product state B, where a transition path could go directly from A to B or cross intermediate states $i \in I$. We are interested in finding every possible transition path and its associated probability. An important quantity is the committor probability q_i^B, which describes the probability that when being in state i, the system will rather reach the product state B than recurring to the reactant state A. The committor probabilities are derived by solving the following system of linear equations

$$-q_i^B + \sum_{k \in I} T_{ik} q_k^B = -\sum_{k \in B} T_{ik}. \tag{2.35}$$

By definition $q_i^B = 0$ if $i \in A$ and $q_i^B = 1$ if $i \in B$. The probability that the system comes from A rather than from B when being in state i is described by the backward committor q_i^A. For systems obeying detailed balance the backward- and forward-committor fulfill

$$q_i^B + q_i^A = 1. \tag{2.36}$$

The committor q_i^B increases gradually when moving closer to the product state B. The *flux* f_{ij} is defined as the probability flux that contributes to transitions from A to B, given by

$$f_{ij} = \pi_i q_i^A T_{ij} q_j^B, \tag{2.37}$$

which describes the rate to find the system in state i (π_i) which was previously in the reactant state A (q_i^A) and moves to state j (T_{ij}) and then reaches rather the product state B than going back to A (q_j^B). When being on a pathway from A to B recrossing events could occur

$$i \to j \to i \ldots. \tag{2.38}$$

The *net flux* given by

$$f_{ij}^B = \max\{0, f_{ij} - f_{ji}\} \tag{2.39}$$

considers only a single transition from one to another state (no recrossing). The set of states and net fluxes between the states form a transition network, which is flux-conserving, the total flux K leaving A must be equal to the flux entering B and is given by

$$K = \sum_{i \in A} \sum_{j \notin A} \pi_i T_{ij} q_j^B. \tag{2.40}$$

For all intermediate states I Kirchhoff's law is fulfilled

$$\sum_{j \in I} (f_{ij} - f_{ji}) = 0. \tag{2.41}$$

When knowing the total flux K we are able to estimate the reaction rate from $A \to B$ as

$$k_{AB} = \frac{K}{\tau \sum_{i=1}^{N} \pi_i q_i^A} \tag{2.42}$$

where τ is the lag time of the transition matrix and N is the number of states. Thus the mean first-passage time is

$$\tau_{\text{mfp}} = 1/k_{AB}. \tag{2.43}$$

Decomposing pathways

The net-fluxes of the full or coarse-grained model are based on individual pathways that connect A and B.

In order to find the probability to observe a certain transition path, we need to decompose the net-flux network.

We define a pathway as a path starting in A and ending in B. The set of all possible pathways is $\mathcal{W}$. A pathway w without recrossing events is called a *reaction pathway*.

An important parameter along a reaction pathway w is its *minimal net-flux*

$$c(w) = \min_{e=(i,j) \in w} \{f_{ij}^B\}. \tag{2.44}$$

The *bottleneck* of a reaction pathway are the two states b_1 and b_2, which are connected by the minimal net-flux

$$(b_1, b_2) = \arg \min_{e=(i,j)\in w} \{f_{ij}^B\}. \tag{2.45}$$

As a consequence, the best reaction pathway is characterized by a maximum of all minimal net-fluxes and is therefore called $c_{\max}(w)$. This pathway is in general not unique since the bottleneck could belong to another reaction pathway as well. The *dominant reaction pathways* $W_D \in \mathcal{W}$ are defined by all pathways

$$W_D = \{w \in \mathcal{W} : c(w) = c_{\max}\}, \tag{2.46}$$

with the same $c_{\max}$. Thus, the bottleneck divides the dominant reaction pathways into two sets

$$W_D = W(\mathbf{L}) \times W(\mathbf{R}), \tag{2.47}$$

such that every reaction pathway can be decomposed into

$$w = (\underbrace{i_{l_1}, \ldots, i_{l_n} = b_1}_{w_L}, \underbrace{b_2 = i_{r_1}, \ldots, i_{r_m}}_{w_R}). \tag{2.48}$$

The *representative dominant reaction pathway* $w^* \in \mathcal{W}_D$ is defined as

$$w^* = \arg \max_{w\in W_D} \min_{\substack{e=(i,j)\in w \\ (i,j)\neq(b_1,b_2)}} \{f_{ij}^B\} \tag{2.49}$$

and describes the reactant pathway which is most likely to be observed.

In order to calculate the probability of all other pathways, the net-flux $c_{\max}$ is removed from the flux network only along the reaction pathway w^* such that a reduced transition network is created

$$\tilde{f_{ij}^B} = \begin{cases} f_{ij}^B - c_{\max}, & \text{if} (i,j) \in w^* \\ f_{ij}^B, & \text{otherwise} \end{cases}. \tag{2.50}$$

The net-flux $\tilde{f_{ij}^B}$ is called the *residual net-flux*. Identifying the dominant reaction pathway of the reduced network will lead to the next most likely transition path. This process is continued until the full flux K has been subtracted, comprised in the following algorithm

i) Compute the representative dominant reaction pathway

ii) Update the flux network in calculating the residual net-flux

iii) Iterate until the entire flux K has been subtracted

The result is an ordered list of all reactant transition pathways

$$(w_1^*, w_2^*, \ldots, w_M^*) \tag{2.51}$$

for every possible reaction pathways such that

- $c_{\text{max}}^{(i)} > c_{\text{max}}^{(j)}, \quad 0 \leq i < j \leq M$
- $\sum_{i=1}^{M} c_{\text{max}}^{(i)} = K$

The probability to observe a certain path is given by

$$P(w_i^*) = \frac{c_{\text{max}}^{(i)}}{K}. \tag{2.52}$$

2.5.3 Free-energy and diffusivity profiles from 2-water MSM

With a MSM, the free-energy and diffusivity profile acting between water molecules can be extracted from the transition matrix. The relative water dynamics is assumed to be governed by the Fokker-Planck equation in three dimensions [1]

$$\frac{\partial}{\partial t} P(\mathbf{r}, t) = \nabla \cdot \left(e^{-\beta U(\mathbf{r})} \mathbf{D}(\mathbf{r}) \cdot \nabla \left[e^{-\beta U(\mathbf{r})} P(\mathbf{r}, t) \right] \right), \tag{2.53}$$

where $P(\mathbf{r}, t)$ is the probability to find the two waters at a certain separation $\mathbf{r}$ at time t, $U(\mathbf{r})$ describes the effective pair potential, $\mathbf{D}(\mathbf{r})$ the relative diffusivity tensor, and $\beta = 1/k_B T$. The diffusivity tensor takes a diagonal form

$$\mathbf{D} = \begin{pmatrix} D & 0 & 0 \\ 0 & D_\phi & 0 \\ 0 & 0 & D_\theta \end{pmatrix} \tag{2.54}$$

when introducing spherical coordinates R, ϕ, θ, where we neglected the orientation of the second water molecule. The angular degrees of freedom can be integrated out

$$p(R, t) = \int_0^{2\pi} d\phi \int_0^{\pi} d\phi \sin(\phi) R^2 P(R, \phi, \theta, t), \tag{2.55}$$

which results in the following partial differential equation for the probability to find the waters at distance R at time t

$$\frac{\partial}{\partial t} p(R, t) = \frac{\partial}{\partial R} \left[R^2 e^{\beta U(R)} D(R) \frac{\partial}{\partial R} e^{\beta U(R)} \frac{p(R, t)}{R^2} \right]. \tag{2.56}$$

We define a free energy $F = U - 2k_{\mathrm{B}}T\ln(R)$ to recover the usual form of the one-dimensional diffusion equation

$$\frac{\partial}{\partial t}p(R,t) = \frac{\partial}{\partial R}\left[e^{-\beta F(R)}D(R)\frac{\partial}{\partial R}e^{\beta F(R)}p(R,t)\right]. \tag{2.57}$$

From simulations the free energy $F(R) = -k_{\mathrm{B}}T\ln\langle p(R)\rangle$ can be obtained easily by Boltzmann inversion of the equilibrium distribution $\langle p(R)\rangle$ which equals the equilibrium distribution of the Markov model

$$\langle p(R)\rangle = \pi(R). \tag{2.58}$$

For the numerical solution of the diffusion Eq. (2.57) we discretize Eq. (2.57) in space and time, which leads to the form of a Master equation

$$\begin{aligned}\frac{p_i(t+\Delta t) - p_i(t)}{\Delta t} &= W_{i,i-1}p_{i-1}(t) + W_{i,i+1}p_{i+1}(t)\\ &\quad + W_{i,i}p_i(t).\end{aligned} \tag{2.59}$$

For the transition rates we use [136]

$$W_{i,j} = \frac{D_i + D_j}{2(\Delta R)^2}\exp\left(-\frac{F_i - F_j}{2k_BT}\right) \quad \text{with} \quad j = i \pm 1 \tag{2.60}$$

and $W_{i,i} = -W_{i-1,i} - W_{i+1,i}$, which satisfies concentration conservation and detailed balance. The concentration profile $p_i(t)$ at time $t = n\Delta t$ follows from Eq. 2.59 as

$$p_i(t) = \sum_{j=1}^{N}\left[(\mathbf{I} + \Delta t\mathbf{W})^n\right]_{i,j}p_j(0) = \sum_{j=1}^{N}\mathrm{e}^{t\mathbf{W}}_{i,j}p_j(0) \tag{2.61}$$

where $\mathbf{I}$ is the identity matrix and $\mathbf{W}$ is the rate matrix defined in Eq. (2.60). The continuous limit $\Delta t \to 0$ in Eq. (2.61) has been taken in order to express the n-th power by the matrix exponential. That way the transition matrix $\mathbf{T}$ can be expressed by the matrix exponential of the rate matrix $\mathbf{W}$ via

$$\mathbf{T}(t) = e^{t\mathbf{W}}. \tag{2.62}$$

The rate matrix $\mathbf{W}$ contains the free-energy and diffusivity profile as given by Eq. (2.60). From a Markov state model the free-energy profile can be easily obtained from the normalized left eigenvector with eigenvalue $\lambda = 1$. The calculation of the diffusivity profile is more subtle. We estimate the diffusivity profile from mean first-passage times which are calculated from an absorbing transition matrix. This is described in detail in the next section.

Absorbing Markov chains

The concept of absorbing Markov chains is described in Ref. [137]. Consider a transition matrix $\mathbf{T}$ with entries T_{ij} and k absorbing states. If at least one state is absorbing, then $T_{ii} = 1$ and the transition matrix can be rewritten as

$$\mathbf{T} = \begin{pmatrix} \mathbf{Q} & \mathbf{R} \\ \mathbf{0} & \mathbf{I} \end{pmatrix}, \tag{2.63}$$

where $\mathbf{I}$ denotes the identity matrix of order k. The submatrix $\mathbf{Q}$ is of square form and corresponds to the transient states. The residual matrix $\mathbf{R}$ is in general not of square from but non-negative. The n-th power of the transition matrix takes the form

$$\mathbf{T}^n = \begin{pmatrix} \mathbf{Q}^n & \mathbf{R}_n \\ \mathbf{0} & \mathbf{I} \end{pmatrix}, \tag{2.64}$$

where

$$\mathbf{R}_n = (\mathbf{I} + \mathbf{Q} + \ldots + \mathbf{Q}^{n-1})\mathbf{R}. \tag{2.65}$$

The inverse of $(\mathbf{I} - \mathbf{Q})^{-1}$ is called the *fundamental matrix*

$$\mathbf{N} = (\mathbf{I} - \mathbf{Q})^{-1} = \mathbf{I} + \mathbf{Q} + \mathbf{Q}^2 + \ldots \tag{2.66}$$

and describes how many times the process will be in transient state j before being absorbed when initially located in a transient state i.

We are interested in calculating the first-passage time distribution $f_{ij}^{(n)}$, describing the probability of being absorbed in state j after exactly n steps when being initially in state i.

Without loss of generality we consider only one absorbing state and the absorbing transition matrix reads as

$$\mathbf{T} = \begin{pmatrix} \mathbf{Q} & \mathbf{r} \\ \mathbf{0}^T & 1 \end{pmatrix}. \tag{2.67}$$

Let $p_{ij}^{(n)}$ denote the probability to reach the absorbing state j within n-steps. Then the first-passage time distribution after n-steps is the difference of the probability of being absorbed within n steps subtracted by the probability of being absorbed within $n-1$ steps

$$f_{ij}^{(n)} = p_{ij}^{(n)} - p_{ij}^{(n-1)}. \tag{2.68}$$

It follows from Eq. (2.65) that

$$\mathbf{f}^{(n)} = \mathbf{r}_n - \mathbf{r}_{n-1} = \mathbf{Q}^{n-1}\mathbf{r}, \tag{2.69}$$

which defines the first-passage-time distribution as a vector, where every component describes the probability of being absorbed in exactly n steps when initially being in state i. The mean first-passage time, the first moment of $\mathbf{f}^{(n)}$, can be calculated by

$$\begin{aligned}\boldsymbol{\tau} =& \sum_{n=0}^{\infty} \mathbf{f}^{(n)} \cdot n \\ =& \sum_{n=0}^{\infty} \mathbf{Q}^{n-1}\mathbf{r} \cdot n \\ =& (1 + 2Q + 3Q^2 + \ldots)\mathbf{r} \\ =& (1 + Q + Q^2 + \ldots) \cdot (1 + Q + Q^2 + \ldots)\mathbf{r} \\ =& \mathbf{N}^2\mathbf{r} \\ =& \mathbf{N}\mathbf{1}, \end{aligned} \tag{2.70}$$

where $\mathbf{1}$ is a vector containing only ones. Further, we used $\mathbf{N}\mathbf{r} = \mathbf{1}$ which follows directly from Eq. (2.65). Since $\mathbf{N}$ can be extracted easily from a transition matrix, the mean first-passage time can be calculated right away from Eq. (2.70).

Diffusivity extraction

We come back to our transition matrix introduced in Eq. (2.62) and expand the matrix for small lag time t, which results in

$$\mathbf{T}(t) \approx \mathbf{I} + t\mathbf{W} + O(\mathbf{W}^2). \tag{2.71}$$

The matrix $\mathbf{Q}$ is given by $\mathbf{Q} = \mathbf{W}'t$, where the dimension of $\mathbf{W}'$ is reduced by one in truncating the last row and column of $\mathbf{W}$. This makes it possible to invert $\mathbf{W}'t$. For the fundamental matrix we can write then

$$\mathbf{N} \approx \left[\mathbf{I} - (\mathbf{I} + \mathbf{W}'t)\right]^{-1} = -(\mathbf{W}'t)^{-1}. \tag{2.72}$$

Together with Eq. (2.70) we obtain the following identity for the mean first-passage times

$$(\mathbf{W}'t)\boldsymbol{\tau} = -\mathbf{1} \tag{2.73}$$

The action of the matrix $\mathbf{W}'$ on the mean first-passage vector τ can also be expressed by

$$(\mathbf{W}'t)\boldsymbol{\tau} = \mathbf{S}\mathbf{d} = -\mathbf{1}, \tag{2.74}$$

where $\mathbf{d}$ is the diffusivity vector

$$\mathbf{d} = (\tilde{D}_1, \ldots, \tilde{D}_{n-1})^T \tag{2.75}$$

which corresponds to the values of the mean diffusion constant between two discretized bins

$$\tilde{D}_i = \frac{D_i + D_{i+1}}{2}. \tag{2.76}$$

The components of the matrix $\mathbf{S}$ are given by

$$S_{1,1} = \frac{(\tau_2 - \tau_1)t}{(\Delta R)^2} \cdot e^{-\frac{F_2 - F_1}{2k_B T}} \tag{2.77}$$

$$S_{i-1,i} = \frac{(\tau_{i-1} - \tau_i)t}{(\Delta R)^2} \cdot e^{-\frac{F_{i-1} - F_i}{2k_B T}} \tag{2.78}$$

$$S_{i,i} = \frac{(\tau_{i+1} - \tau_i)t}{(\Delta R)^2} \cdot e^{-\frac{F_{i+1} - F_i}{2k_B T}} \tag{2.79}$$

$$S_{n-1,n-1} = -\frac{\tau_i t}{(\Delta R)^2} \cdot e^{-\frac{F_{n+1} - F_n}{2k_B T}}. \tag{2.80}$$

When we invert $\mathbf{S}$ we obtain the diffusivity vector

$$\mathbf{d} = -\mathbf{S}^{-1}\mathbf{1}. \tag{2.81}$$

However, this inversion might be singular or ill-posed, which occurs e.g. when two neighboring mean first-passage times are almost equivalent or the when the sampling is insufficient. This problem can controlled when regularizing the original problem. The *Tikhonov* regularization of Eq. (2.81) yields the following least-square problem

$$\min\{\|\mathbf{S}\mathbf{d} + \mathbf{1}\|_2^2 + \|\lambda\mathbf{d}\|_2^2\}, \tag{2.82}$$

where $\lambda > 0$ is the regularization parameter. The explicit solution to Eq. 2.82 is given by

$$-\mathbf{d} = (\mathbf{S}^T\mathbf{S} + \lambda^2\mathbf{I})^{-1}\mathbf{S}^T\mathbf{1}. \tag{2.83}$$

This can be rewritten when $\mathbf{S}$ is described by its singular value decomposition

$$\mathbf{S} = \mathbf{U}\mathbf{\Sigma}\mathbf{V}^T, \tag{2.84}$$

where the columns of $\mathbf{U}$ are called the left-singular vectors, the orthonormal eigenvectors of $\mathbf{S}\mathbf{S}^T$, and the columns of $\mathbf{V}$ are the right-singular vectors, the orthonormal eigenvectors of $\mathbf{S}^T\mathbf{S}$. The diagonal of $\mathbf{\Sigma}$ carries the (positive) singular values σ_i which are the square roots of the positive eigenvalues of the symmetric matrix $\mathbf{S}^T\mathbf{S}$. Using the definition of the singular value decomposition for $\mathbf{S}$ we obtain

$$\begin{aligned}
-\mathbf{d} &= \left[(\mathbf{U}\mathbf{\Sigma}\mathbf{V}^T)^T\mathbf{U}\mathbf{\Sigma}\mathbf{V}^T + \lambda^2\mathbf{I}\right]^{-1}(\mathbf{U}\mathbf{\Sigma}\mathbf{V}^T)^T\mathbf{1} \\
&= \left[\mathbf{V}^T(\mathbf{\Sigma}^T\mathbf{\Sigma} + \lambda^2\mathbf{I})\mathbf{V}\right]^{-1}\mathbf{V}\mathbf{\Sigma}^T\mathbf{U}^T\mathbf{1} \\
&= \mathbf{V}\left[\mathbf{\Sigma}^T\mathbf{\Sigma} + \lambda^2\mathbf{I})\right]^{-1}\mathbf{\Sigma}^T\mathbf{U}^T\mathbf{1} \\
&= \mathbf{V}\mathrm{diag}\left(\frac{\sigma_1}{\sigma_1^2 + \lambda^2}, \ldots, \frac{\sigma_n}{\sigma_n^2 + \lambda^2}\right)\mathbf{U}^T\mathbf{1}.
\end{aligned} \tag{2.85}$$

We see that for singular values close to zero, the regularization parameter $\lambda > 0$ assures an invertible matrix $\mathbf{S}$.

Diffusivity profile

Finally we are able to calculate the diffusivity profile. We record trajectories from a MD simulation (same as main text) for pairs of waters, where only the distance R between the two oxygen atoms is stored. We start recording as soon as the radial distance between the two oxygen atoms is $R < 1.4$ nm and stop when the distance becomes larger than $R \geq 1.4$ nm. In total, more than 7 million trajectories are recorded. We equally cluster within the range from $R_{\text{min}} = 0.23$ nm to $R_{\text{max}} = 1.4$ nm with a spatial resolution of $\Delta R = 0.01$ nm and estimate the transition matrix.

We calculate the mean first-passage times according to Eq. (2.70) from the transition matrix $\mathbf{T}(t = 7.0\,\text{ps})$ for a lag time of $t = 7$ ps and plot the results in Fig. 2.9A for different choices of the absorbing target position R_t. There is a maximum in the mean first-passage time at about $R = 0.26$ nm. For smaller separations the dynamics cannot be described by a one-dimensional diffusion equation since it would result in a negative diffusivity according to Eq. (2.74), where a stritly decreasing mean first-passage time is demanded.

The free energy is estimated from the normalized left eigenvector with eigenvalue $\lambda = 1$ via $F_i = -k_{\text{B}}T\ln(\pi_i)$, see Fig. 2.9B. There is a barrier of $\Delta F = 1\ k_{\text{B}}T$ for crossing from the first to the second hydration shell, for larger separations a decreasing free energy $F \propto -\ln(R)$ is observed. At about a separation distance of $R = 1.0$ nm the free energy increases again. This is caused due to limited sampling at a lag time that is larger than the time resolution of the data. The diffusivity profile has been calculated according to Eq. (2.85). Due to the maximum in the mean first-passage times, the matrix $\mathbf{S}$ becomes singular. Therefore we choose a small regularization parameter of $\lambda = 0.001$ to ensure invertibility.

The calculated diffusivity profile shows a pronounced minimum in the first hydration shell with a minimum value of $D_{\text{min}} \approx 0.8\,\text{nm}^2/\text{ns}$. Up to $R = 0.8$ nm the diffusivity profile is in good agreement to the results obtained previously from the mean first-passage method presented in [1]. For $R > 1.0$ nm it starts to deviate caused by the increase of the free energy due to limited sampling.

Lag-time sensitivity

We discuss the resulting free-energy and diffusivity profile when the lag time is varied.

We estimate transition matrices for lag times of $t = [0.1, 1, 2, 3, 7, 10]$ ps and calculate the resulting free-energy and diffusivity profiles according to Eq. (2.83), which are plotted in Fig. 2.10. We see a strong dependence on the chosen lag time for the diffusivity, whereas the free-energy profile shows only deviations for separation values of $R > 1.0$ nm which are characterized by a slight increase at larger lag times. At a

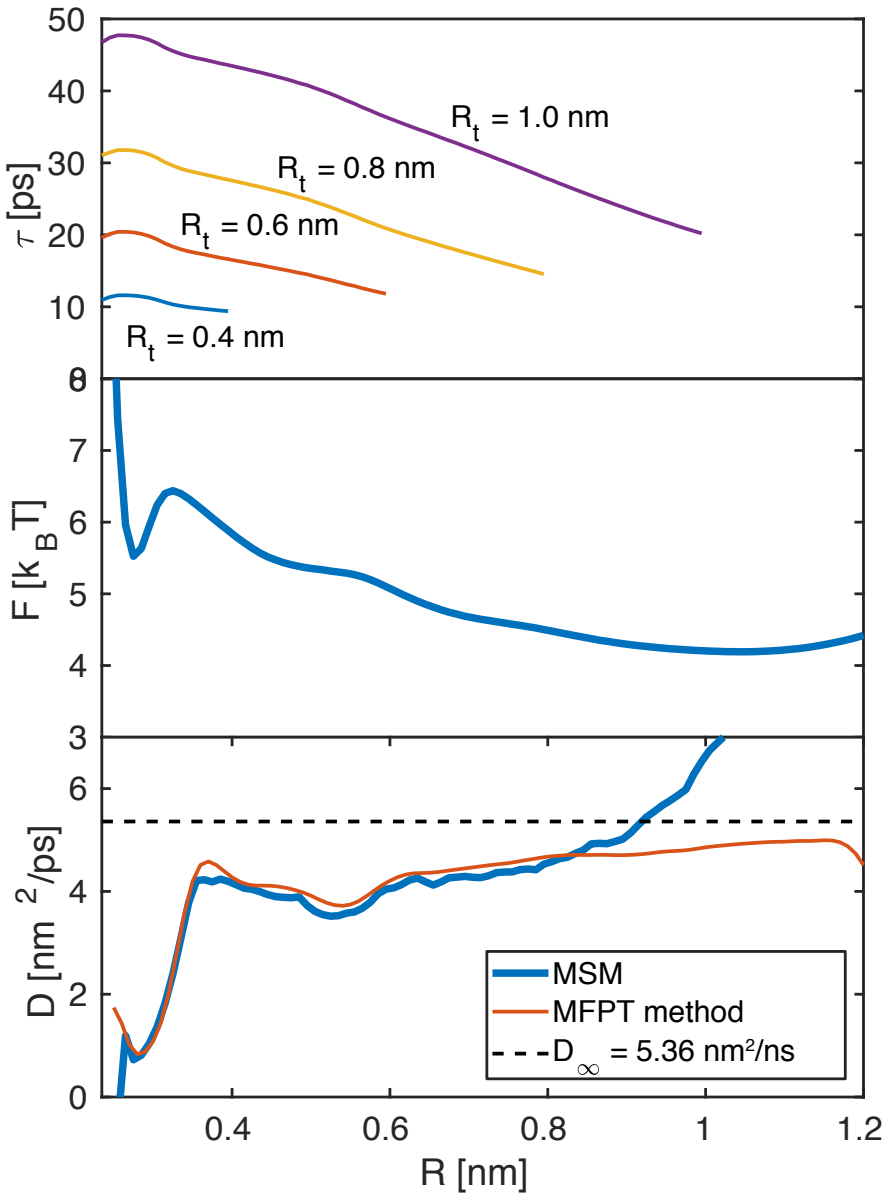

Figure 2.9: **(A)** Mean first-passage times for different target separations R_t obtained from the transition matrix estimated at a lag time of $t = 7$ ps. **(B)** Free-energy profile obtained from the (left) eigenvector with eigenvalue $\lambda = 1$. **(C)** Diffusivity profile obtained from Eq. (2.81) (blue lines) compared with profile estimated previously by the mean first-passage time method (red lines) [1].

lag time of $t = 0.1$ ps the largest diffusivities are obtained. The diffusivity approaches the values obtained from the round-trip method for lag times $t > 3$ ps. This result is at first sight suprising since the estimation of the diffusivity profile according to Eq. (2.74) holds strictly in the limit $t \to 0$, since the identity between the rate matrix $\mathbf{W}'$

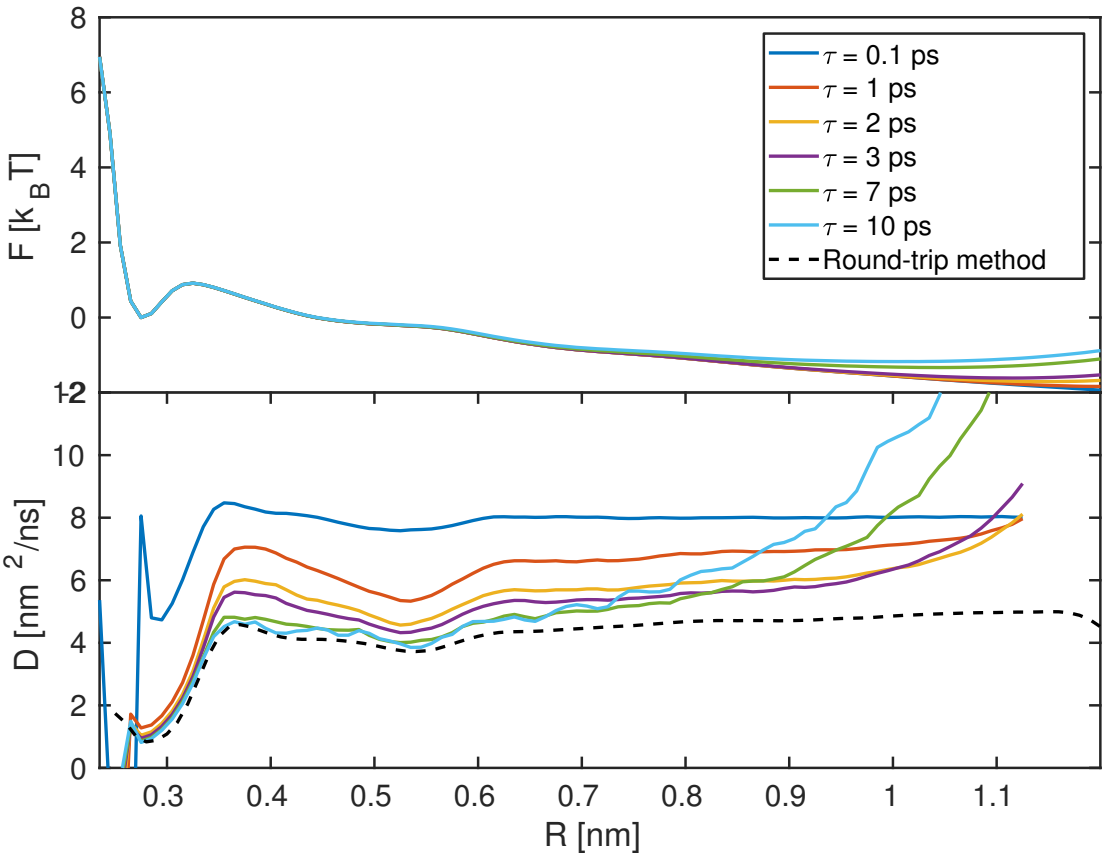

Figure 2.10: **(A)** Free energy estimated for different lag times. The increase at $R > 1.0$ nm is due to insufficient sampling at large lag times. **(B)** Diffusivity profiles estimated for different lag times according to Eq. (2.85).

and mean first-passage times in Eq. (2.74) results from a linear expansion of $\mathbf{T}(t)$. We summarize that a MSM reproduces observables such as the free-energy and diffusivity profiles in agreement with other methods such as the mean first-passge time method [1].

2.5.4 Varying the number of clusters

We next discuss the behavior of the time scales when different numbers of clustes are used while the number of trajectories is kept constant. The clusters have been calculated by the k-means++ algorithm [129] for cluster numbers of 10, 100, 500, 1000, and 2000. We plot the behavior of the slowest time scale t_1^* in Fig. 2.11.

With increasing cluster number the time scales are shifted upwards. For larger cluster numbers the change is smaller. For cluster numbers ≥ 500 the lag time plot stays rather invariant.

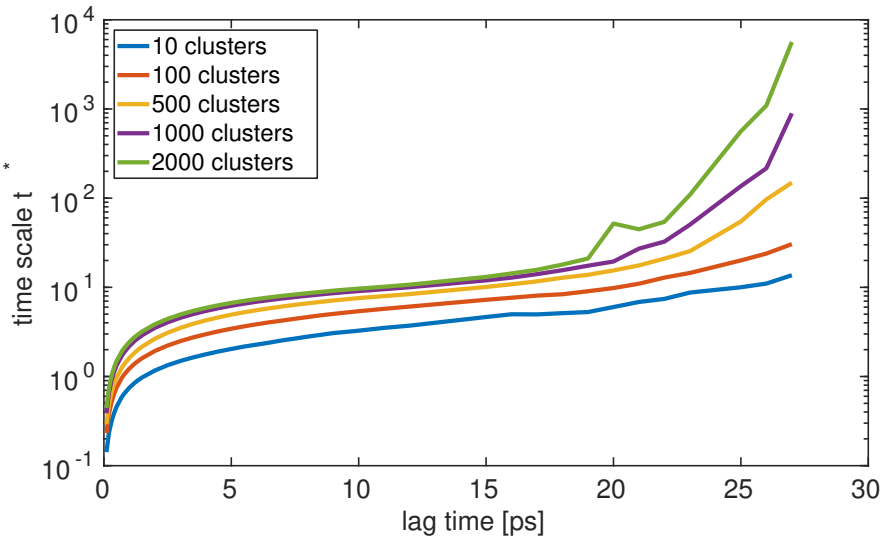

Figure 2.11: Slowest time scale behavior for different number of cluster centers in the three-water MSM.

2.5.5 Lag-time dependency from reduced data sets

In this section we discuss the behavior of the time scales when fewer data is used to estimate the transition matrix of the Markov model. We use the 320.000 trajectories of the three-water MSM (see main text) with a total length of approximately 1700 ns and a time resolution of 0.1 ps corresponding to $17 \cdot 10^6$ data points.

The full trajectory is separated into $(1.7, 17, 170, 1700)$ ns slices corresponding to approximately $0.1\%, 1\%, 10\%$ and 100% of the full data. We use $n = 500$ clusters and estimate the cluster states by the k-means++ algorithm and construct the transition matrix of the Markov model. We study the behavior of the slowest time scale in Fig. 2.12.

For a data reduction to 0.1% (blue line) no constant domain is visible and the time scale increases exponentially for $\tau > 3$ ps. In the case when 1% of data is used (cyan line) the Markovianity breaks apart for $\tau \approx 10$ ps and for the other two cases (green and orange) at $\tau \approx 15$ and 20 ps respectively. The black horizontal line denotes the time scale of the considered process $t_1^* \approx 6.1$ ps. The dashed vertical lines indicate the lag time at which the time scale estimate becomes unreliable. It can be derived as follows.

Assume we estimate a transition matrix by counting transitions from one to another state via

$$T_{ij}(\tau) = \frac{c_{ij}(\tau)}{\sum_j c_{ij}(\tau)}. \tag{2.86}$$

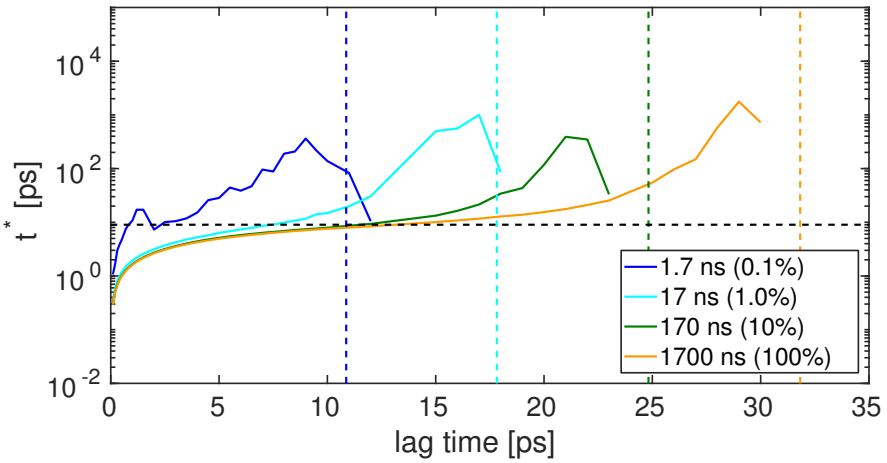

Figure 2.12: Behavior of the slowest time scale t_1^* of the three-water MSM when the input data is reduced.

We assume there is a sampling error σ when estimating an eigenvalue

$$\lambda = \lambda_{\text{est}} + \sigma. \tag{2.87}$$

This then yields for the time scale

$$t^* = -\frac{\tau}{\ln[\lambda_{\text{est}} + \sigma]}. \tag{2.88}$$

For increasing lag times the eigenvalue eventually becomes smaller than the sampling error

$$\lambda \ll \sigma \tag{2.89}$$

so that the estimated eigenvalue is dominated by the sampling error, which yields for the time scale

$$t^* \approx -\frac{\tau}{\ln(\sigma)}. \tag{2.90}$$

The critical threshold for the lag time is therefore given by

$$\tau_{\text{crit}} \approx -t^* \cdot \ln \sigma \tag{2.91}$$

We can estimate the error σ by associating the absolute error with the standard deviation, which in general decays for a number of N data points as

$$\sigma \propto \frac{1}{\sqrt{N}} \tag{2.92}$$

where N is the number of data points. Let us for simplicity assume that each state of the total $n = 500$ states has been visited equally. Then the number of visits per cluster is approximately $N/n \approx \sum_j c_{ij}$. This would imply a standard deviation for the error of an element of the transition matrix of

$$\sigma \approx \frac{1}{\sqrt{N/n_c}} \tag{2.93}$$

The calculated critical lag times are depicted in Tab. 2.1. We can see that these values

length	1.7 ns	17 ns	170 ns	1700 ns
data points	$1.7 \cdot 10^4$	$17 \cdot 10^4$	$170 \cdot 10^4$	$1700 \cdot 10^4$
σ	0.17	0.05	0.02	0.005
τ_{crit}	10.8 ps	17.8 ps	24.8 ps	31.8 ps

Table 2.1: **Critical lag time.** Estimation error of the transition matrix and critical lag time.

define an upper boundary before the time scales start increasing. Obviously, increasing the amount of data does not significantly increase the shift of the critical lag time τ_{crit}. As a rule of thumb, an increase of the amount of data by a factor of 10, would only increase the critical lag time by approximately the time scale, since

$$\begin{aligned} \tau_{\text{crit}} &= -t^* \cdot \ln(10N/n)^{-\frac{1}{2}} \\ &= -t^* \cdot [\ln(N/n)^{-\frac{1}{2}} - \frac{1}{2}\ln(10)] \\ &\approx -t^* \cdot \ln(N/n)^{-\frac{1}{2}} + t^* \end{aligned} \tag{2.94}$$

Especially for small time scales the increase of data has only a small effect of extending the Markovian plateau.

2.5.6 Eigenvector analysis at different lag times for three-water MSM

In the main text, we used a lag time of $\tau = 7$ ps for the three water model. We now show that if we change the lag time to $\tau = 3$ ps and to $\tau = 15$ ps, the interpretation of the eigenvectors does not change, see Fig. 2.13. The slowest process describes exactly the same process if we choose $\tau = 3$ ps or $\tau = 15$ ps, which holds also for the 2nd slowest process. Therefore, a variation of the lag time does not influence the interpretation and time ordering of the processes.

2.5.7 H-bond rearrangements from two-water MSM

The two-water MSM captures the slow dynamics of two water molecules O* and O^a in the 6-dimensional state space. The same MD-simulation as in the main text is used and the model trajectories are selected in the following way. Whenever the radial distance

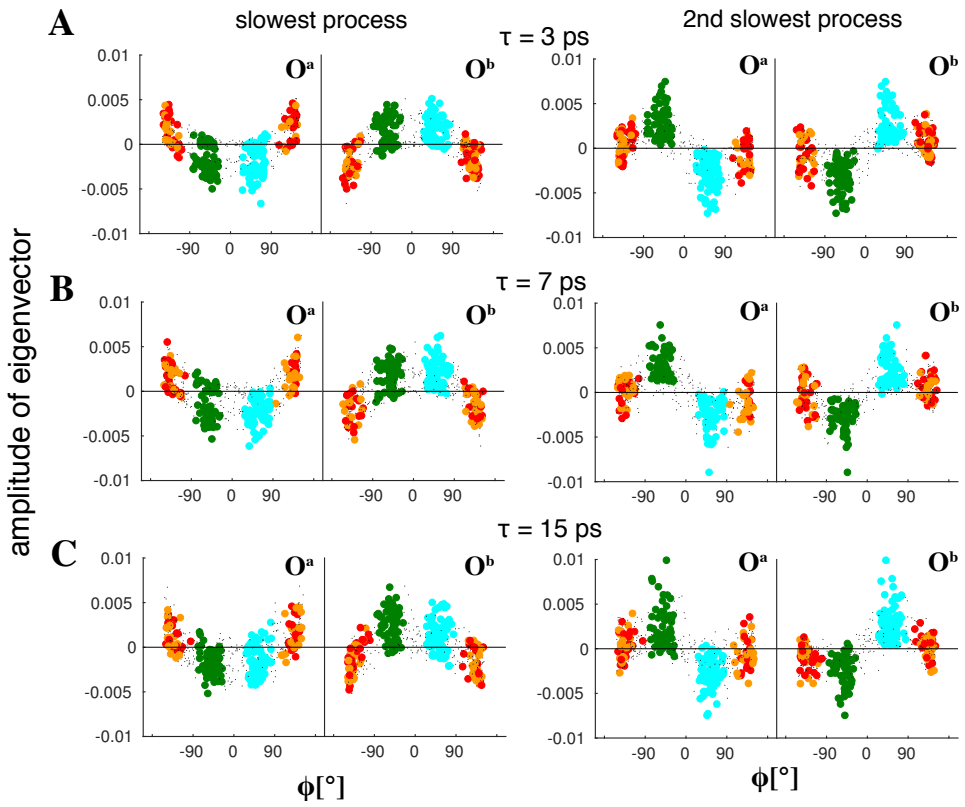

Figure 2.13: Slowest and second slowest process in the three-water MSM. The interpretation of the eigenvectors at different lag times does not change.

between the two oxygen atoms is $R < 0.5$ nm the relative position between these two water molecules is recorded as a 6-dimensional trajectory by three Euler angles and three spherical coordinates. In total, we captured 872,853 trajectories suming up to a total trajectory length of 1250 ns which are used as input for the MSM. A typical trajectory can be seen in Fig. 2.14, where the recording starts at a separation value of $R < 0.5$ nm and ends at a separation value of $R > 0.5$ nm. The cyan, green, red, and orange colors correspond to different kinds of H-bonds which are explained in the main text. We cluster the 6-dimensional state space, for which we use the k-means++ algorithm implemented in PyEmma [129,138] with 500 cluster centers. The time scale behavior is shown in Fig. 2.15A. For small lag times $\tau < 1$ ps the time scales increase rapidly. Two factors are limiting the convergence to a constant plateau for small lag times. The first one is due to inertial effects, since velocities are ignored in our Markov state model.The second one arises from the finite number of clusters, which also introduces memory effects. For $\tau > 1$ ps the time scales separate and the slope of the time scales decreases. However, a perfectly constant plateau, as implied by Eq. (2.32), is not observed, which indicates that the dynamics in the 6-dimensional state space is not purely Markovian

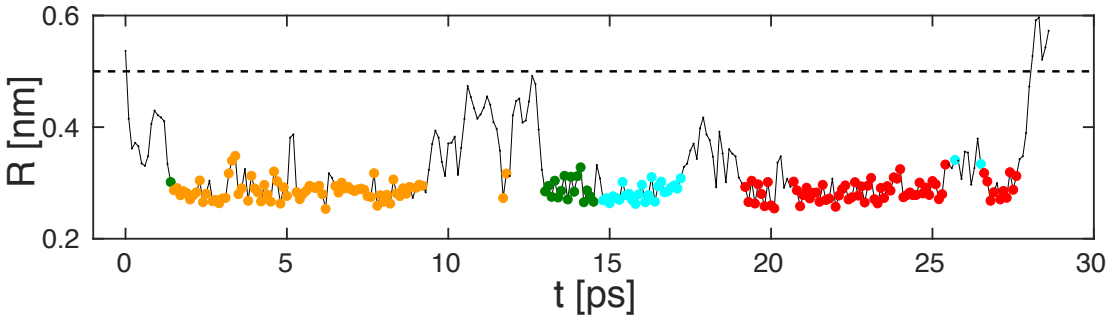

Figure 2.14: **Trajectory of two water molecules.** Typical time series of the radial distance R between two water molecules. The colors mark different H-bond configurations between O* and O[a].

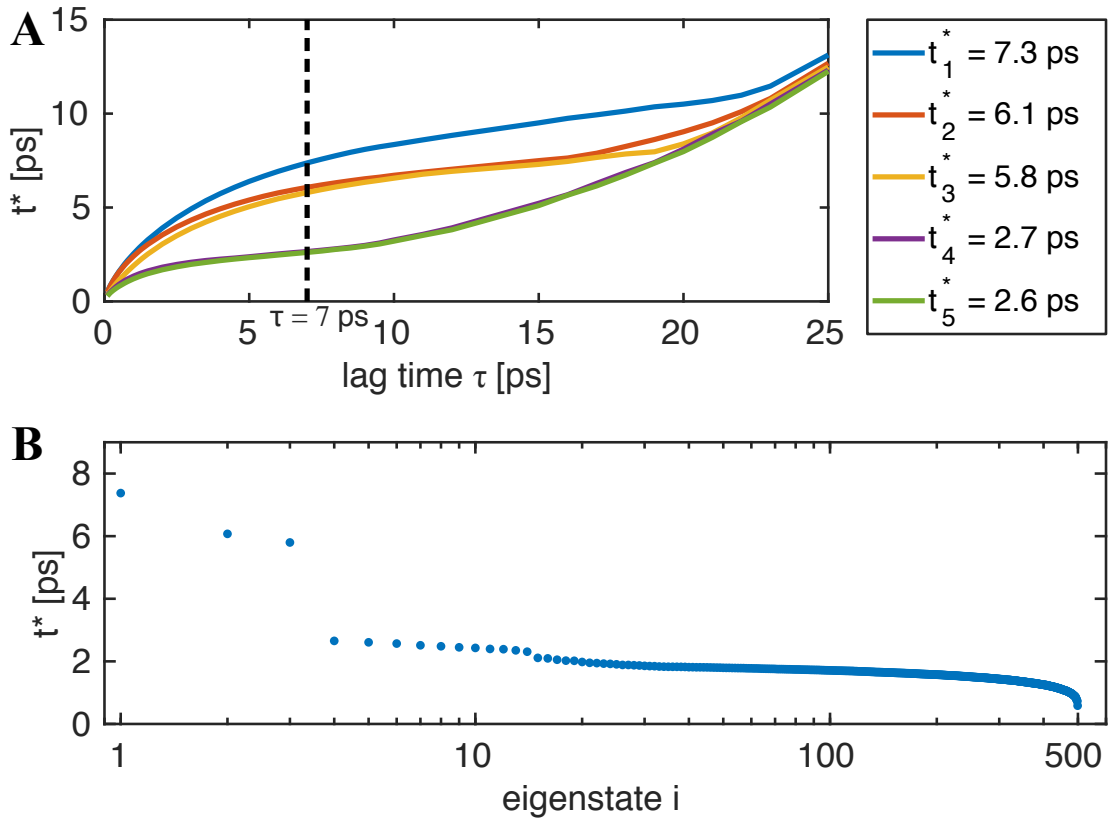

Figure 2.15: **(A)** Plot of the five slowest time scales t_i^* versus the lag time time τ for the two-water MSM. **(B)** Plot of all time scales for a fixed lag time $\tau = 7$ ps. The first three time scales separate from the continuum of the faster time scales.

due to the two factors stated above. Nevertheless, we can clearly separate different time scales and thus discern the processes associated to these different time scales. For $\tau > 20$ ps the time scales begin to merge again and cannot be distinguished anymore.

This is caused by insufficient statistics at lag times which exceed the largest time scale of the MSM. We discuss the behavior of time scale merging at large lag times in Sec. SI 2.5.5.

We choose the lag time of $\tau = 7$ ps, as in the three-water MSM, marked by a dashed line in Fig. 2.15A and plot also the other time scales for the chosen lag time in Fig. 2.15B. The three slowest time scales can be separated from the continuum of all other time scales and will be discussed here.

Eigenvector analysis

The first eigenvector $\boldsymbol{\pi}$ is associated to the eigenvalue $\lambda = 1$ and thus corresponds to the stationary distribution. We projected each component of the 500-dimensional stationary distribution vector on the Euler and spherical coordinates, see Fig. 2.16. In each of the 6 plots there are 500 dots, each representing the equilibrium value of

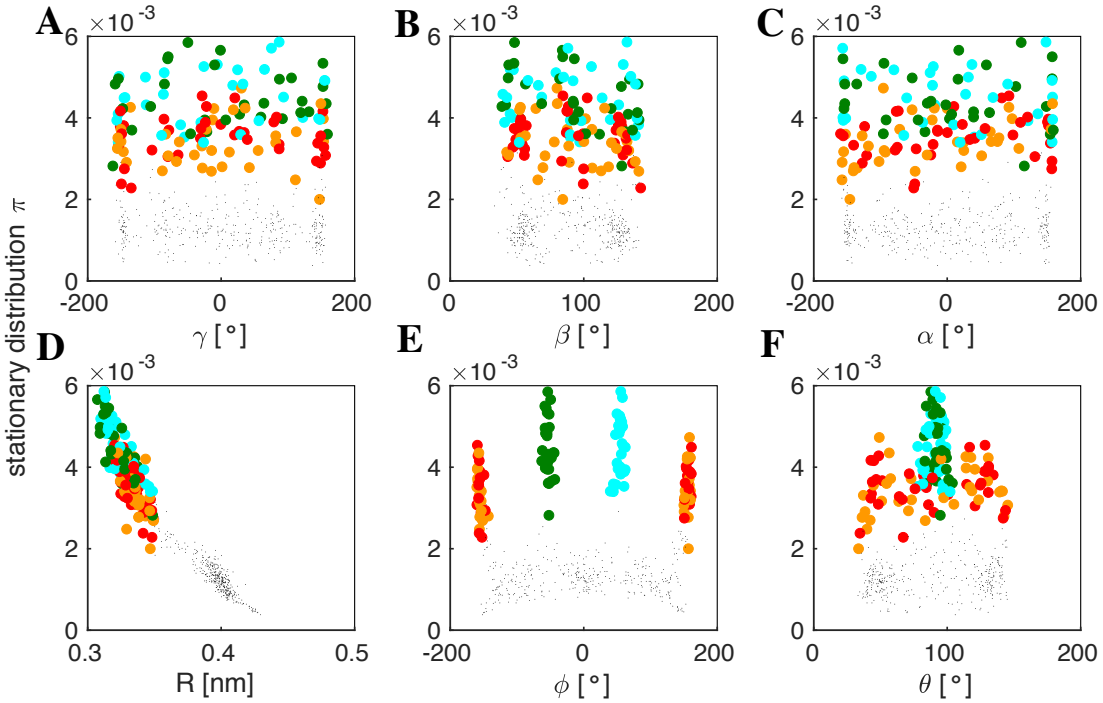

Figure 2.16: Equilibrium state of the two-water MSM. We show the projection of the eigenvector onto the Euler angles (α, β, γ) and onto the spherical coordinates (R, ϕ, θ). The colors denote different H-bonds between O* and O^a.

the associated coordinate we project on. Additionally, we mark the type of H-bond between O* and O^a by different colors, see main text for color definition, whereas the black dots indicate non H-bonded configurations.

The projection on the Euler angles in Fig. 2.16A,B,C provides no intuitive understanding of the configurations, but when we turn our focus on the three spherical co-

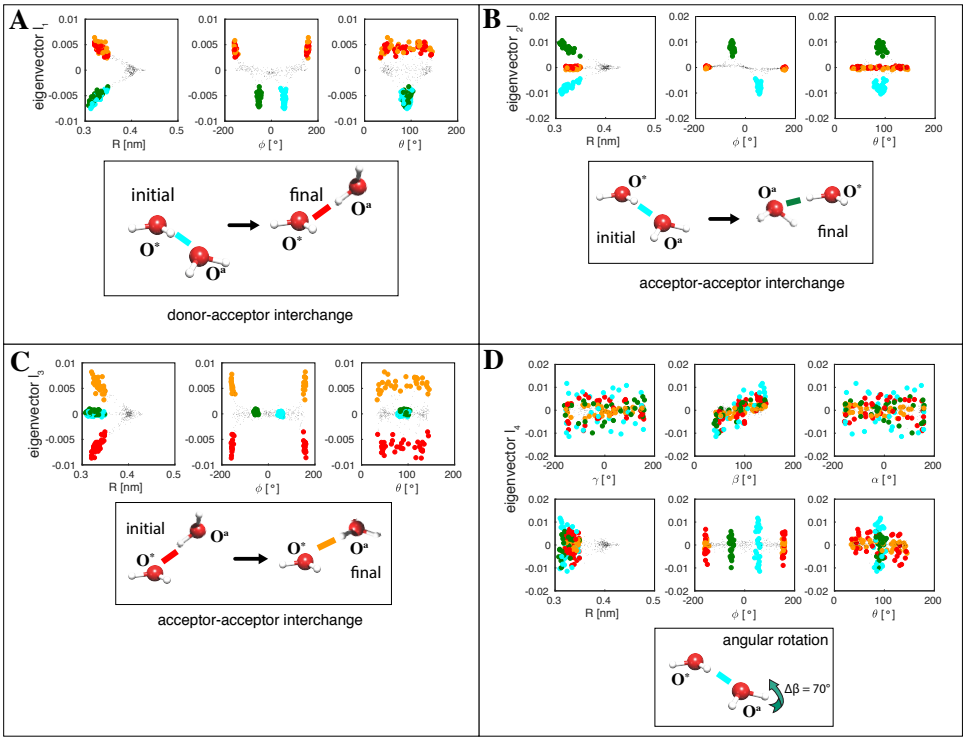

Figure 2.17: **(A)** The eigenvector associated with the slowest time scale $t_1^* = 7.3$ ps describes a donor-acceptor interchange, where O* and O^a interchange their roles as acceptor and donor. **(B)** Acceptor-acceptor interchange with a time scale of $t_2^* = 6.1$ ps. Here O* donates an H-bond to O^a via one of its hydrogen atoms, whereas in the final state O* provides the H-bond through its other hydrogen atom. **(C)** Acceptor-acceptor interchange with a time scale of $t_3^* = 5.8$ ps. This process is very similar to the second slowest process, where the role of O^a and O* are interchanged. **(D)** Fifth slowest process with $t_3^* = 2.7$ ps. Water O^a does not change its H-bonded state to O*, but performs an angular rotation of $\Delta\beta = 70°$ observable in the β-coordinate of the Euler angles.

ordinates we can see interpretable structures. In the plot in Fig. 2.16D, we see that it is very likely to find a configuration for small separation values, whereas with increasing distance the probability to find the two water molecules decreases. The ϕ-coordinate Fig. 2.16E clearly shows that the four peaks are associated to the four H-bond configurations defined in the main text. In the cyan and green configuration at $\phi \approx \pm 55°$, O* donates an H-bond to O^a, whereas in the red and orange configurations O* accepts an H-bond from O^a. In the θ-coordinate in Fig. 2.16F, the green and cyan configuration are peaked at $\theta \approx 90°$, whereas the red and orange ones are spread out over the entire θ-range. We conclude that H-bonds can be most clearly discerned from the ϕ-coordinate.

The slowest process in the MSM is given by the largest time scale, which here is $t_1^* = 7.3$ ps as indicated by the blue line in Fig. 2.15A. We examine the corresponding eigenvector by projecting on the spherical coordinates, see Fig. 2.17A.

Similar to the three-water MSM, the slowest process describes a donor-acceptor interchange. We can see how all green and cyan configurations (O* donates to O^a) carry negative components in the eigenvector, which describes a loss of probability, whereas the red and orange configurations (O^a donates to O*) carry positive components in the eigenvector. Thus, this process describes the interchange of donor and acceptor roles between O* and O^a. The process could also be interpreted the other way around, since an eigenvector can always be multiplied by a negative number, which would then result in an acceptor-donor interchange. This process can thus be regarded as a subprocess of the three-water MSM.

The second slowest process $t_2^* = 6.1$ ps describes an acceptor-acceptor interchange similar as found for the three-water MSM. Water O^a accepts initially an H-bond from O* through H_1^*, whereas in the final state the H-bond to O^a is provided through H_2^*, see Fig. 2.17B. An equivalent picture is seen in the third slowest process with almost the same time scale of $t_3^* = 5.8$ ps, where O^a provides an H-bond to O* with one of its hydrogen atom and finally donates through the other hydrogen atom, see Fig. 2.17C.

All faster processes are characterized by time scales of $t^* < 2.7$ ps, see Fig. 2.15B. The interpretation of the eigenvectors becomes more difficult and not every eigenvector has a simple physical interpretation. We discuss the 5th slowest process with $t_5^* = 2.7$ ps and project on the Euler and spherical coordinates, see Fig. 2.17D. Every of the four possible H-bond configurations is homogenously distributed for a fixed ϕ-angle, which indicates that the initial and final H-bonded positions are not changed. When we examine the Euler angle β, a change is observable. For $\beta < 100°$ the states are negative, whereas for $\beta > 100°$ the states are positive. The other two Euler angles are spread out almost equally on the negative and positive domain. We can calculate the angular change $\Delta\beta$ as the difference of the positive mean β-value and the negative mean β-value according to

$$\Delta\beta = \frac{\sum l_i \cdot c_i \cdot \Theta(c_i)}{\sum l_i \cdot \Theta(c_i)} - \frac{\sum l_i \cdot c_i \cdot (1 - \Theta(c_i))}{\sum l_i \cdot (1 - \Theta(c_i))} \approx 70°, \tag{2.95}$$

where l_i is the $i-$th component of the considered eigenvector, c_i is the i-th cluster center for β, and Θ denotes the Heaviside function. Interestingly, this value of $\Delta\beta = 70°$ is already close to the angle of $68°$ that Laage et al. [37, 59] derived for the average reorientation jump angle when an H-bond donating water molecule changes its acceptor water. This could indicate that this process is associated to an angular rotation O^a performs to provide a H-bond to another water while staying H-bonded to O*.

Summarizing, in the two-water MSM we can distinguish different processes, which are associated to breaking and forming of H-bonds. These time scales deviate slightly from the time scales in the 3-water MSM, but the observed processes correspond to subprocesses of the processes observable in the three-water MSM. Therefore, the three-water MSM can be regarded as a product of two two-water MSMs.

2.5.8 Validity of MSM for H-bond acceptor switching

We discuss the validity of the model described in Sec. IIIB in the main text. In Fig. 2.18A we plot all time scales estimated from the Markov state model. The three slowest time scales begin to saturate for $t > 1$ ps. On the one hand a small lag time is important to reduce the effect of spurious transitions when applying transition path theory, but on the other hand the lag time should not be too small since the ballistic motion of water dominates in this regime. In fact, the crossover from ballistic to the Markovian regime occurs when the mean squared displacement changes its scaling from $\propto t^2$ to $\propto t$, which occurs for a diffusing water molecule in our set-up at about $t = 0.2$ ps, see Fig. 2.18C. In Fig. 2.18B we plot the mean first-passage time of the switching event where O* switches its H-bond from O^a to O^b. The blue line corresponds to the mean first-passage time obtained directly from the MD-trajectory. For small lag times this yields a mean first-passage time of $\tau_{\text{mfp}}^{\text{MD}} \approx 3.3$ ps which is equivalent to the reorientation time estimated by Laage et. al. in Ref. [37]. With increasing lag time the mean first-passage time increases, caused by recrossing effects that occur. The red line in Fig. 2.18B corresponds to the mean first-passage time estimated from the transition matrix according to Eq. (2.70) and is equivalent to the mean first-passage time estimated from Eq. (2.43) and shows a stronger dependence of the chosen lag time. Our choice of the lag time of $t = 1$ ps ensures that the deviation between these two methods of extracting the mean first-passage time is minimal.

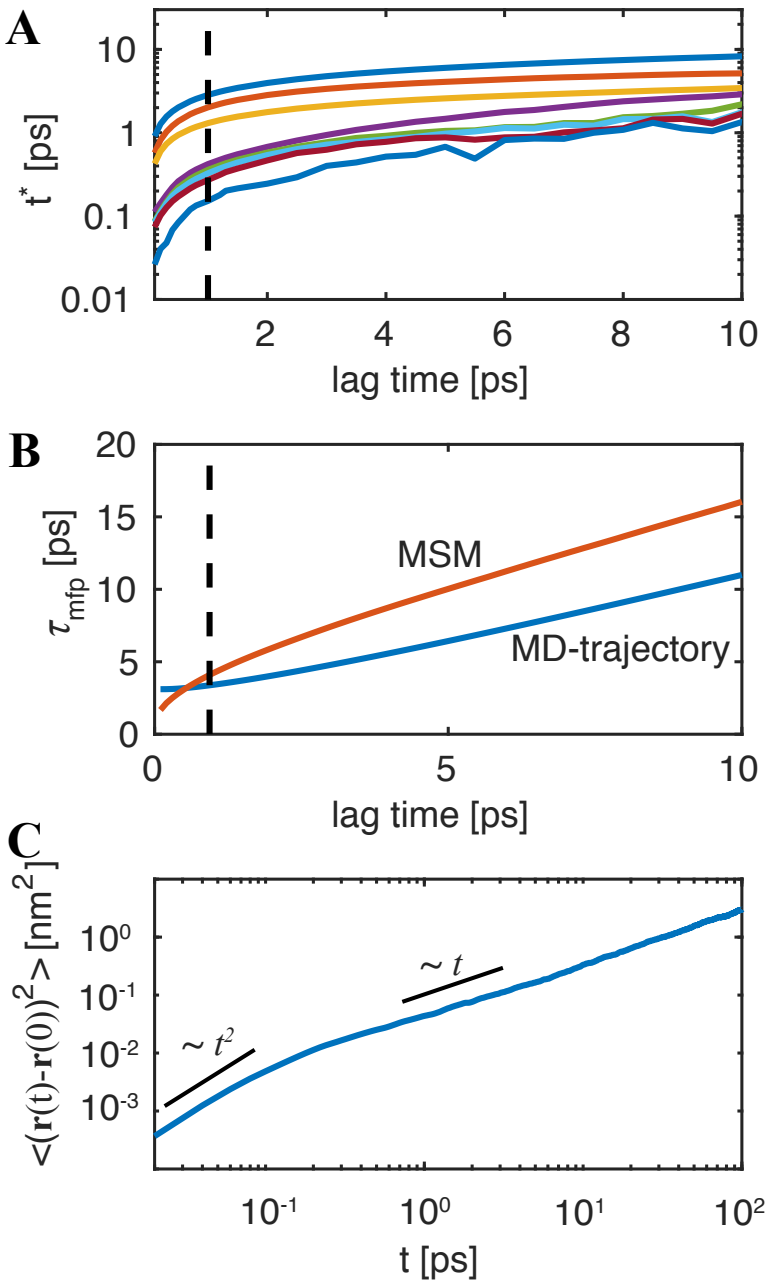

Figure 2.18: **(A)** Lag times from MSM for H-bond switching. Markovianity is approximately obtained for $t > 1$ ps. **(B)** Mean first-passage times estimated directly from MD-trajectory (blue) and from the transition matrix (red). **(C)** Mean squared displacement for two diffusing water molecules, which indicates a crossover from ballistic to diffusive motion at $t \approx 0.2$ ps.

Chapter 3

Data-based modeling of drug penetration relates human skin barrier function to the interplay of diffusivity and free-energy profiles

Parts of this chapter have previously been published. Reprinted with permission from Ref. [ii]. Copyright 2017 by the National Academy of Science.

3.1 Introduction

Multicellular organisms exhibit numerous structurally distinct protective barriers, such as the blood-brain barrier, intestinal, mouth and respiratory mucosa, and the skin, the largest human organ. These barriers are generally designed to keep foreign material out and in some cases to allow the highly regulated transfer of certain desired molecules,

consequently, they present a severe challenge for drug delivery [74, 75, 139]. The in-depth understanding of barrier function is not only required for controlled drug delivery, but is also of central interest in medicine, drug development and biology.

Human skin can be broadly divided into two layers, see Fig. 3.1A, the epidermis with a thickness of about 100 μm, which prevents water loss and the entrance of harmful microorganisms or irritants, and the dermis, which is typically 2 mm thick, contains blood vessels and protects the body from mechanical stress [140].

The epidermis is further divided into the stratum corneum (SC), the 10 μm - 20 μm thick outermost layer consisting of dried-out dead skin cells, the corneocytes, and the viable epidermis (VE). In the stratum granulosum (SG), which is part of the VE, skin cells (keratinocytes) are gradually flattened and transformed into corneocytes when migrating toward the SC.

The SC is structurally similar to a brick wall [141]: The bricks are the corneocytes,

while the mortar is the intercellular matrix, which is composed of stacked lipid bilayers. Several models for the permeation of drugs through skin exist, which incorporate the skin structure on different levels of complexity. In the simplest models the stratified skin structure is reflected by 1D layers with different diffusivities and partition coefficients [81–84,142], in more detailed models the 3D SC structure is accounted for [85,86]. In all models a certain skin structure and various transport parameters are assumed, which a posteriori are adjusted such as to reproduce experimental permeabilites or concentration-depth profiles inferred from tape-stripping studies [85, 86]. For a detailed overview of skin-diffusion models and a historical outline see Refs. [143,144].

We describe here a data-based modeling approach, i.e., which does not make any model assumptions, and as the only input requires drug concentration depth profiles in the skin at three consecutive times. Our approach, which we test for the lipophilic anti-inflammatory glucocorticoid dexamethasone (DXM) in *ex vivo* human skin, is very general and can be used for all kinds of permeation barriers. This drug is chosen since soft X-ray absorption spectromicroscopy allows to generate 2D absolute concentration profiles of unlabeled DXM in thin skin slabs with a resolution below 100 nm [145,146].

We start with the general 1D diffusion equation, which describes the evolution of a 1D concentration profile $c(z,t)$ in space and time and depends on the position-dependent free-energy profile $F(z)$ and the diffusivity profile $D(z)$

$$\frac{\partial}{\partial t}c(z,t) = \frac{\partial}{\partial z}\left(D(z)e^{-\beta F(z)}\frac{\partial}{\partial z}c(z,t)e^{\beta F(z)}\right), \tag{3.1}$$

where $\beta = 1/(k_{\mathrm{B}}T)$ is the inverse thermal energy. The free-energy profile $F(z)$ reflects the local affinity and determines how the substance, in our specific case DXM, partitions in equilibrium, namely $c_{\mathrm{eq}}(z) \propto e^{-\beta F(z)}$. The diffusivity profile $D(z)$ is a local measure of the velocity at which the substance diffuses in the absence of external forces. The diffusion equation not only describes passive and active particle transport in structured media, it has in the past also been used for modeling marketing strategies [20], decision making [21] and epigenetic phenotype fluctuations [147]. The importance of a spatially varying diffusivity profile $D(z)$ has been recognized for the relative diffusion of two particles [148], trans-membrane transport [149], particle diffusion at interfaces [19,150], protein folding [18,151–153] and multidimensional diffusion [154]. The 1D diffusion equation can be solved analytically only in simple limits, for general $F(z)$ and $D(z)$ profiles the solution $c(z,t)$ must be numerically calculated.

The inverse problem, i.e. extracting $F(z)$ and $D(z)$ from simulation or experimental data, is much more demanding and has recently attracted ample theoretical attention. With one notable exception [155], most inverse approaches need single-particle stochastic trajectories and are not suitable to extract information from concentration profiles [19,148,149,156–158]. For the typical experimental scenario, where a few concentration profiles at different times are available, we here present a robust method that yields the $F(z)$ and $D(z)$ profiles with minimal numerical effort and for general open boundary conditions (see Material and Methods). We demonstrate our method using experimental 1D concentration-depth profiles of DXM (obtained by the Rühl group,

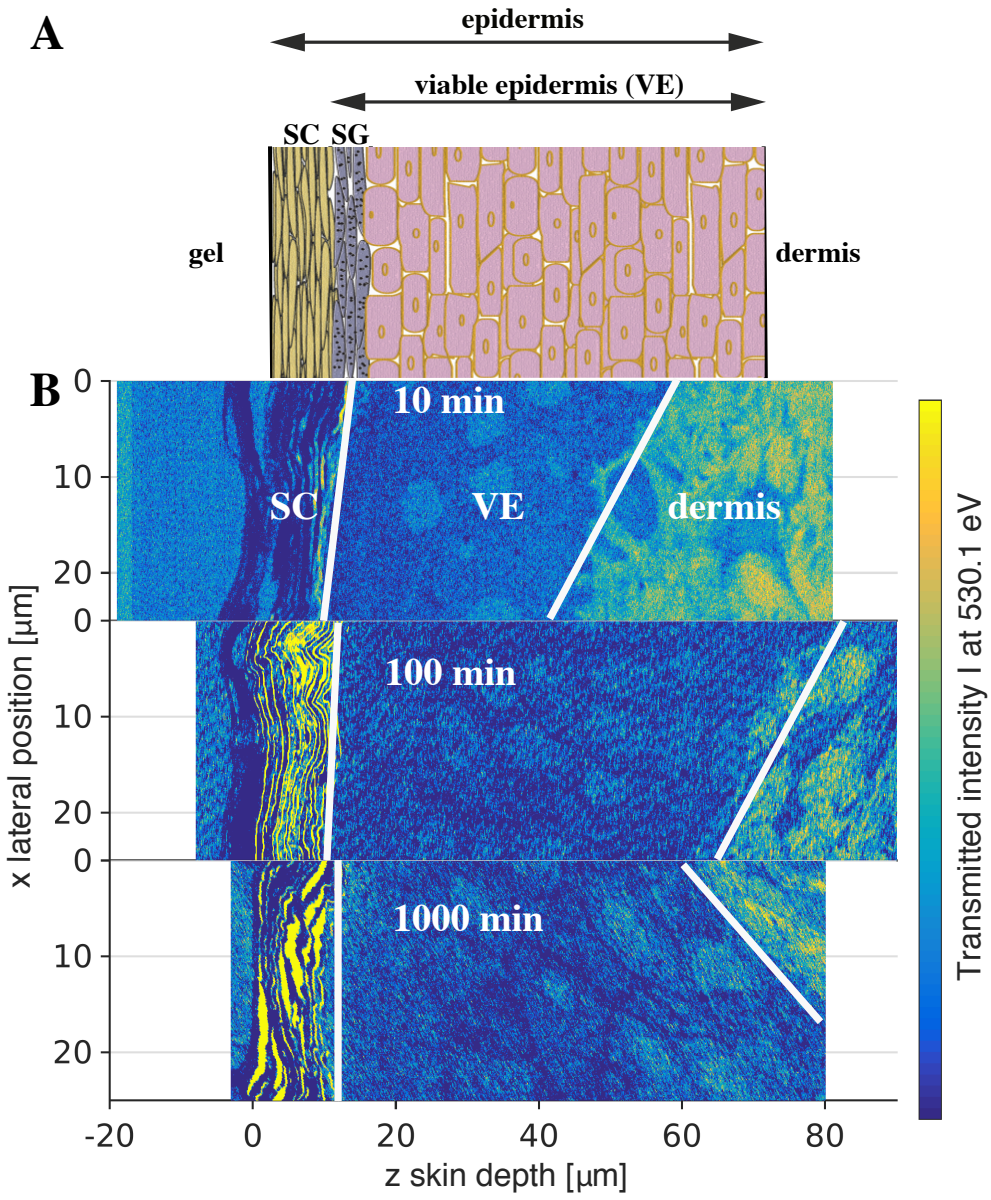

Figure 3.1: (A) Schematic epidermal skin structure. (B) Normalized 2D-transmission intensity profiles from X-ray scanning microscopy at photon energy 530.1 eV after 10, 100, and 1000 min penetration time. The profiles allow one to distinguish different skin layers, schematically indicated by white dividing lines, and demonstrate the skin sample variation. While the SC has a rather uniform thickness, the VE thickness varies considerably between the three samples.

FU Berlin), a medium-size drug molecule that in water is only poorly soluble [159]. Starting the drug penetration by placing a 1.5% DXM formulation in hydroxethyl cellulose (HEC) gel on top of excised human skin at time zero (performed by our col-

laborators from the Schäfer-Korting/Hedtrich (Institute of Pharmacy, FU Berlin) and Vogt/Blume-Peytavi group (Dermatology department, Charité Berlin)), 2D concentration profiles of DXM in the epidermal skin layer are obtained after penetration times of 10, 100, and 1000 min using soft X-ray absorption-spectromicroscopy [145, 146] (see Material and Methods).

In order to determine both the free-energy profile $F(z)$ and the diffusivity profile $D(z)$ in the epidermal skin layer as well as the diffusive DXM properties in the drug-containing HEC gel and in the dermis, we need three experimental concentration profiles recorded at different times as input. We demonstrate that both the diffusivity profile $D(z)$, which dominates drug penetration for short times, and the free-energy profile $F(z)$, which dominates long-time drug concentration profiles, are needed to describe drug penetration quantitatively.

Our analysis reveals that skin barrier function results from an intricate interplay of different skin layer properties: While the entrance of lipophilic DXM into the SC is free-energetically favored, the drug diffusivity in the SC is about thousand times lower than in the VE and thus slows down the passage of DXM through the SC. In addition, a pronounced free-energy barrier from the epidermis to the dermis prevents DXM from penetrating into the lower dermal layers. In essence, the epidermis has a high affinity for the lipophilic drug DXM, which together with the low diffusivity in the SC efficiently prevents DXM penetration into the dermis.

3.2 Results and discussion

3.2.1 Experimental concentration profiles

Figure 3.1B shows 2D absorption profiles recorded by our collaborators from the Rühl group (FU Berlin) at photon energy 530.1 eV for penetration times of 10, 100, and 1000 min. This photon energy selectively excites DXM [145]. The skin-depth coordinate z is shifted such that the outer skin surface is aligned to $z = 0$. The color codes the transmitted intensity, with blue indicating low and yellow high transmission, and allows insights into the skin structure. Note that the three profiles originate from different skin samples from the same donor, since the analysis of the identical skin sample for different penetration times is not possible [146]. Accordingly, these three samples have been chosen for maximal similarity of the SC and VE thicknesses.

The region below $z < 0$ μm is the Epon resin employed for skin embedding. For all three samples, the layered structure from $z \approx 0$ μm to $z \approx 10$ μm is the SC, while the VE extends from a depth of about $z \approx 10$ μm to a variable depth ranging from $z \approx 50$ μm to $z \approx 80$ μm. Within the VE oval-shaped keratinocyte nuclei are discerned, which move gradually toward the SC where they differentiate and flatten into corneocytes. The dermis, separated from the VE by the basal layer and the basal membrane, is clearly distinguished from the VE by the different transmission intensity. Note that the variation of the VE thickness across different samples is an inherent property of skin and must be kept in mind in the analysis. From the ratio of the 2D transmission

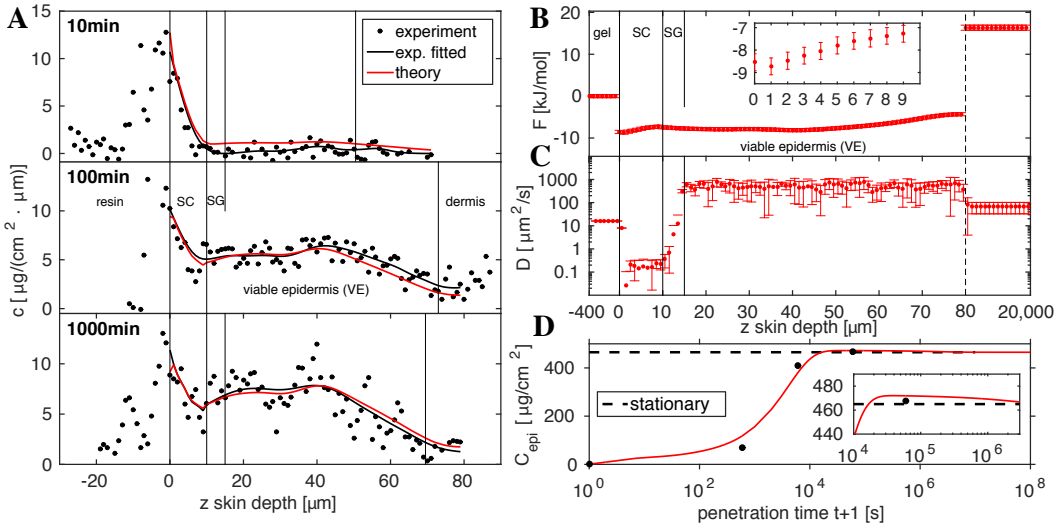

Figure 3.2: (**A**) 1D experimental DXM concentration profiles at three different penetration times (black circles) and cubic smoothing splines (black lines) are compared with theoretical predictions based on the diffusion equation (red lines). Vertical dividing lines indicate skin layers and are based on the 2D transmission intensity profiles in Fig. 3.1B. (**B**) Free-energy profile $F(z)$ and (**C**) diffusivity profile $D(z)$ derived from the experimental concentration profiles. $F(z)$ is low in the entire epidermis (SC and VE) compared to HEC gel and to the dermis and exhibits a small but significant gradual increase in the SC (see inset), the epidermis thus exhibits lipophilic affinity. $D(z)$ is low in the SC and increases by a factor of 1000 in the VE, where it is close to the free-solution value. The low diffusivity in the stratum granulosum (SG) in the depth range 10 μm $< z <$ 15 μm could indicate the presence of tight junctions. In the gel and beyond $z = 80\mu$m (indicated by a vertical broken line) the $F(z)$ and $D(z)$ profiles are approximated as constant. (**D**) Integrated amount of DXM in the epidermis C_{epi} from experiments (black circles) and theory (red line), showing a maximum at penetration time $t \approx 6 \times 10^4$ $s = 1000$ min (see inset) before it relaxes to the predicted stationary value indicated by a horizontal broken line.

profiles at photon energies of 530.1 eV and 528.0 eV the 2D concentration profiles of DXM are determined [145, 146] (see Sec. 3.4.1 and Figs. 3.5 and 3.6 for details).

Our aim is not to describe DXM diffusion at the cellular level, for which 3D concentration profiles at different penetration times of the same sample would be needed, our goal rather is to model the 1D diffusion of DXM from HEC gel on the skin surface through the epidermis into the deeper skin layers. For this, we laterally average the experimental 2D concentration profiles, the resulting 1D concentration data are shown in Fig. 3.2A (filled circles). We base our modeling on cubic smoothing spline fits (black lines) in the range $0 < z < 80$ μm, disregarding residual DXM in the Epon resin for $z < 0$ μm as well as the range $z > 80$ μm where only a single concentration profile is available. It is seen that already after 10 min penetration DXM has entered the SC. After 100 min penetration DXM is found in the VE, while the concentration in the SC has not changed much. The difference between the 100 min and the 1000 min profiles is seen to be rather small.

3.2.2 Extracting free-energy and diffusivity profiles

Feeding the three experimental DXM concentration profiles in the depth range $0 < z < 80$ μm after 10, 100, and 1000 min penetration time into our inverse solver for the diffusion equation, we derive the best estimates for the $F(z)$ and $D(z)$ profiles shown in Fig. 3.2B and C; in the gel and in the dermis, due to the absence of experimental data, we approximate $F(z)$ and $D(z)$ to be constant. The error bars reflect the standard deviation of the estimates that pass the error threshold $\sigma < 0.6$ μg/(cm$^2\mu$m) (see Material and Methods for more details).

The free energy $F(z)$ in Fig. 3.2B, approximated to be constant in the gel and set to $F_{\text{gel}} = 0$, exhibits a jump down by $\Delta F_{\text{gel/SC}} \approx -8.6$ kJ/mol at the boundary between gel and SC. This is in line with the lipophilic character of DXM which prefers to be in the lipid-rich SC compared to the HEC gel formulation. In the SC, the free energy increases rather smoothly by ≈ 1.5 kJ/mol over a range of 10 μm (see inset of Fig. 3.2B), reflecting a significant structural change across the SC that sustains the steep water chemical potential gradient across the SC [160]. In the depth range 10 μm $< z < 50$ μm, which corresponds to the VE, the free energy is rather constant. In the range 50 μm $< z < 80$ μm the free energy slightly increases again, which reflects the decreasing DXM concentration in the experimental profiles in Fig. 3.2A for 100 min and 1000 min. Comparison with the transmission intensity profiles in Fig. 3.1B reveals that this free energy increase is caused by the transition from the epidermis to the dermis, which due to skin sample variations is smeared out over a broad depth range of 50 μm $< z < 80$ μm. The free-energy jump of $\Delta F_{\text{VE/derm}} \approx 20.5$ kJ/mol at $z = 80\mu$m reflects a pronounced barrier for DXM penetration into the dermis related to the different DXM affinity to the dermis compared to the VE. Due to data scattering this value constitutes a lower bound, as is explained in Sec. 3.4.5 and Fig. 3.7. In fact, the free-energy difference between the HEC gel and the dermis, $\Delta F_{\text{gel/derm}} \approx 16.2$ kJ/mol =6.4 k_BT, is quite close to the free-energy difference derived from the maximal DXM solubility in water, $c_{\text{H}_2\text{O}} = 89$ mg/L at 25°C [161], and the DXM solubility in HEC gel $c_{\text{gel}} = 15$ g/L, via the partition coefficient according to $k_BT \ln(c_{\text{gel}}/c_{\text{H}_2\text{O}}) = 5.1 k_BT$. The free-energy profile thus identifies the dermis as essentially water-like, while the epidermis is a sink with high lipophilic affinity, in line with previous conclusions [162].

The constant diffusivity in HEC gel turns out to be $D_{\text{gel}} \approx 16$ μm$^2/s$ and drops in the SC by a factor of roughly 80 to $D_{\text{SC}} \approx 0.2$ μm$^2/s$, see Fig. 3.2C. The diffusivity maintains such a low value up to a depth of $z = 15$ μm, where it abruptly increases. For $z \geq 15$ μm $D(z)$ exhibits a rather constant value of $D_{\text{VE}} \approx 400$ μm$^2/s$, which is significantly larger than the value in HEC gel and somewhat smaller than the estimated diffusion constant of dexamethasone in pure water $D_{\text{H}_2\text{O}} \approx 680$ μm$^2/s$ [159]. We tentatively associate the layer 10 μm $< z < 15$ μm, where the diffusivity is as low as in the SC but which structurally is distinct from the SC and belongs to the VE, with the stratum granulosum (SG). Note that the SG, which is known to be located right below the SC, is not visible in the transmission profiles in Fig. 3.1B, The SG barrier function has been shown to be due to tight junctions [163–166], in line with the low local diffusivity

in this region displayed in Fig. 3.2C.

Summarizing, four distinct features are revealed by our analysis, (i) a low diffusivity in the SC, (ii) a low diffusivity in a thin layer just below the SC which we associate with the SG, (iii) a sudden drop in free energy from the gel to the SC and a slight but significant free-energy increase in the SC, and (iv) a pronounced free-energy barrier from the epidermis to the dermis. We stress that these features in the free-energy and diffusivity profiles are not put in by way of our analysis method, but rather directly follow from the experimental concentration profiles. We note in passing that the steep increase of the diffusivity at the boundary from the putative SG (with $D_{\rm SG} \approx 1\ \mu{\rm m}^2/s$) to the VE (with $D_{\rm VE} \approx 400\ \mu{\rm m}^2/s$) is nothing one could directly identify from the experimental concentration profiles shown in Fig. 3.2A.

3.2.3 Predicting concentration profiles

In Fig. 3.2A we demonstrate that the numerical solutions of the diffusion equation (red lines), based on the free-energy and diffusivity profiles $F(z)$ and $D(z)$ in Fig. 3.2B+C, reproduce the experimental concentration profiles very well (black lines). Small deviations are observed for the drug-concentration profile after 10 min penetration time, the agreement is almost perfect for the 100 and 1000 min profiles. This not only means that our method for extracting $F(z)$ and $D(z)$ from concentration profiles works, we also conclude that the diffusion equation (3.1) describes the concentration time evolution in skin very well.

We define the time-dependent integral DXM amount that has penetrated into the epidermis over the distance range $0 < z < 80\ \mu$m as

$$C_{\rm epi} = \int_{0\mu m}^{80\mu m} c(z) dz. \tag{3.2}$$

In Fig. 3.2D we compare the experimental data for $C_{\rm epi}$ (filled circles), which are directly obtained by integrating over the experimental concentration profiles in Fig. 3.2A, with the theoretical prediction based on the diffusion equation and the determined $F(z)$ and $D(z)$ profiles (red line). Note the logarithmic time scale that extends from $t = 1$ s to $t = 10^8$ s ≈ 3 ys. According to the experimental protocol, at time $t = 0$ the entire amount of DXM, corresponding to a surface concentration of $600\mu{\rm g/cm}^2$, is located in the gel and thus $C_{\rm epi}$ is zero. With increasing time, the theoretically predicted $C_{\rm epi}$ increases gradually and reaches a maximum of $C_{\rm epi} = 471.9\ \mu{\rm g/cm}^2$ at $t \approx 6 \times 10^4$ s $= 1000$ min, at which time only $\approx 1.2\ \mu{\rm g/cm}^2$ DXM have penetrated into the dermis (see Sec. 3.4.4 for details). In the long-time limit, which is reached above $t \approx 10^7$ s ≈ 115 days, as seen in the inset of Fig. 3.2D, theory predicts the equilibrium value $C_{\rm epi}^{\rm eq} = 465.0\ \mu{\rm g/cm}^2$, denoted by a horizontal broken line. In this hypothetical limit, longer than the exfoliation time of skin which is 30 - 40 days, theory predicts that $\approx 10.0\ \mu{\rm g/cm}^2$ DXM have penetrated into the dermis, while $\approx 125.0\ \mu{\rm g/cm}^2$ DXM still reside in the gel (see Sec. 3.4.4 for the full calculation). Note that *in vivo*, dermal blood

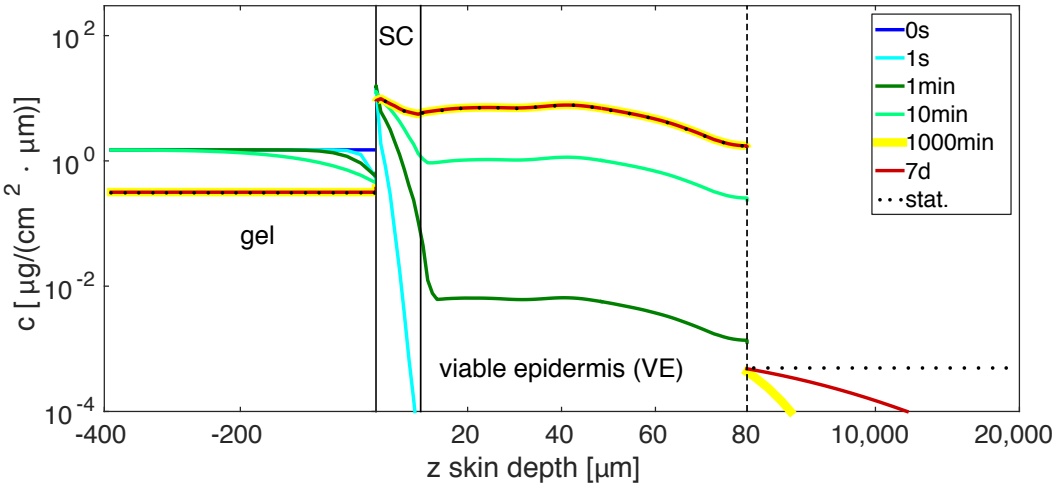

Figure 3.3: Comparison of theoretical DXM concentration profiles for a wide range of different penetration times. At time zero the drug is entirely in the gel. Already at t=1 s DXM penetrates into the SC. At intermediate times t=1 min and t=10 min the VE is gradually filled, while at longer times t=1000 min and t=7 d the profile below the epidermis approaches the stationary profile (indicated by a dotted curve).

perfusion is crucial and could be easily taken into account in a generalized diffusion model by an additional reaction term.

The theoretically predicted curve for C_{epi} in Fig. 3.2D agrees well with the experimental data, which is not surprising in light of the good agreement of the concentration profiles in Fig. 3.2A. This indicates that also the short- and long-time DXM penetration amounts, which are difficult to extract experimentally, are straightforwardly obtained from our model.

In Fig. 3.3 we show calculated DXM concentration depth profiles for a wide range of times. We here also plot the predicted concentration profiles in the gel and below the epidermis, for which no experimental data is available. We see that for short penetration times the concentration profile in HEC gel is inhomogeneous, so the simplifying assumption of a constant concentration in the gel becomes invalid. Interestingly, already at $t = 1$ s DXM enters the SC. The 1000 min profile is indistinguishable from the stationary profile in the HEC gel and the epidermis, while below the epidermis, extending from $z = 80$ μm to $z = 2$ cm, even after 7 days the stationary (flat) concentration profile has not yet been reached (note the inhomogeneous depth scale and the logarithmic concentration scale). Not surprisingly, molecular diffusion over a macroscopic length scale of 2 cm takes a long time.

3.2.4 Checking model validity

We check the robustness of our diffusion model by comparison with two simplified models. In the constant-F model we restrict the free energy in the epidermis to be constant (with the diffusivity still being a variable function), while in the constant-D model

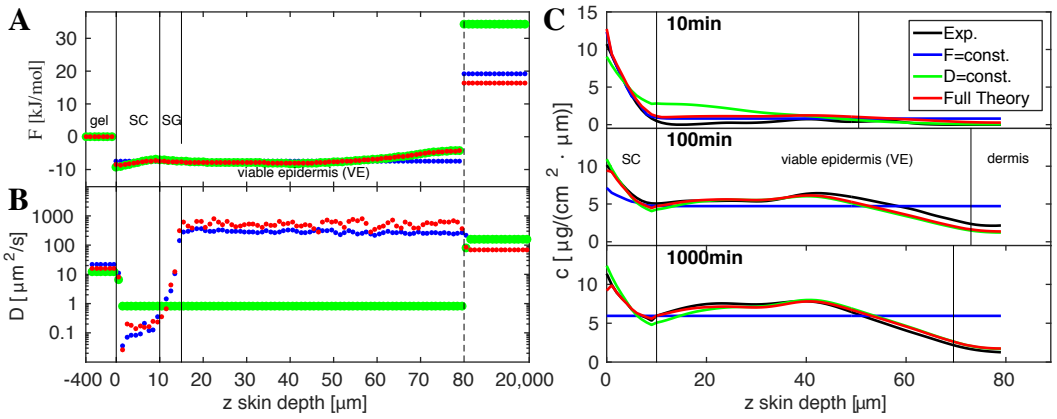

Figure 3.4: Comparison of the restricted constant-F (blue lines) and the constant-D model (green lines) with the full model (red lines) and experimental concentration profiles (black lines) in terms of the (A) free energy, (B) diffusivity and (C) concentration profiles. The constant-F model fails to predict the experimental long-time concentration profiles for penetration times 100 min and 1000 min, the constant-D model fails to predict the short-time concentration profile 10 min.

we restrict the diffusivity in the epidermis to be constant (with the free energy being a variable function). This means that the number of adjustable model parameters drops from 162 in the full model down to 83, otherwise we use the same methods for finding inverse solutions of the diffusion equation as before (see Material and Methods).

The free-energy profiles of the constant-F (blue) and the constant-D models (green) in Fig. 3.4A are rather similar and differ not much from the full model result (red), in particular, the free energy jumps from the HEC gel to the SC and from the VE to the dermis come out roughly the same. The diffusivity profile of the constant-F model in Fig. 3.4B is again similar to the full model, while the constant-D model obviously misses the diffusivity jump from the SC to the VE region.

When we look at the predicted DXM concentration profiles in Fig. 3.4A we clearly see the short-comings of the restricted models: The constant-F model (blue lines) correctly predicts the short-time behavior including the 10 min profile, but fails severely for the long penetration time 1000 min which is close to the stationary equilibrium limit. In contrast, the constant-D model (green line) produces a concentration profile for 1000 min that is indistinguishable from the full model and thus describes the experimental profile very nicely, while it fails at the short penetration time of 10 min. The comparison of the full model with the restricted models demonstrates that both the free-energy and the diffusivity profiles are needed in order to correctly describe the experimental concentration profiles over the entire penetration time range from 10 min to 1000 min. We also understand from this comparison that the diffusivity profile is important at penetration times up to 10 min, while the free-energy profile is required to describe the long-time and the equilibrium behavior accurately.

A robustness check by comparison with results obtained from a reduced data set is shown in Sec. 3.4.6 and Fig. 3.8, from which we conclude that the model is able to cor-

rectly predict concentration profiles even for times at which limited data is provided.

3.2.5 Conclusions

A method for deriving free-energy and diffusivity profiles from experimental concentration profiles at three different penetration times of drugs in human skin is presented. The approach is generally applicable to all kinds of barrier situations and different diffusors whenever spatially resolved concentration profiles at different times are available and can also be generalized to higher dimensions. For the specific example of dexamethasone penetrating into human skin, our results demonstrate that both diffusivity and free-energy profiles are important to describe the skin barrier: The inhomogeneous free-energy profile is essential to correctly describe the long-time concentration profiles, while the diffusivity profile is needed for reproducing the short-time drug penetration. Epidermal skin barrier function against the permeation of DXM is shown to rely on the combination of two key properties, namely a low diffusivity in the SC and a low free energy (i.e. high solubility) in the entire epidermis. Each of these properties by itself severely reduces the DXM permeation through the epidermis, but it is the combination that leads to the exceptionally low and slow DXM transport into the dermis.

The design of efficient drug delivery methods through the epidermis thus meets two challenges: First, the low diffusivity in the SC needs to be overcome. Secondly, the free-energy barrier from the epidermis, which we show to have pronounced lipophilic affinity, to the hydrophilic dermis severely slows down the permeation of lipophilic drugs. The remedy could consist of modified drugs with balanced lipophilic-hydrophobic character such that the epidermis-dermis affinity barrier is small or even absent. To aid the design of such drugs, similar studies shall be undertaken for compounds with varying lipophilicity and molecular weight.

3.3 Materials and methods

3.3.1 Experimental concentration profiles

The experimental studies use *ex vivo* human 2-cm-thick abdominal skin samples and were detailed previously [145,146] and performed by the Rühl, Schäfer-Korting/Hedtrich, and Vogt/Blume-Peytavi group. The skin surface was exposed to a 0.4 mm thick layer of a 70% ethanol HEC gel formulation containing DXM with a concentration of $c_{\text{gel}}(t = 0) = 1.5$ mg/(cm^{2}mm) for penetration times of 10, 100, and 1000 min at a temperature of 305 K in a humidified chamber at the saturation point. After gently removing the HEC gel, samples were subsequently treated in a 2.5% glutaraldehyde in 0.1 M Na-cacodylate buffer and with K_4[(Fe(CN)$_6$] and OsO_4 for lipid and DXM fixation, dehydrated, embedded in epoxy resin, sliced into sections of 350 nm thickness, and placed on silicon nitride membranes of 100 nm thickness. X-ray microscopy studies were performed at the synchrotron radiation facility BESSY II (Berlin, Germany) in

a scan depth range of 100 μm with a step width of 200 nm. The photon energy was tuned in order to probe exclusively DXM at 530.1 eV via the O $1s \rightarrow \pi^\star$ transition [146]. This allows us to derive the absolute local DXM concentration by using Beer-Lambert's law, see [145, 146] for details.

3.3.2 Numerical solution and inversion of diffusion equation

For the numerical solution the diffusion equation (3.1) is discretized in space and time and takes the form of a Master equation [136]

$$\frac{c_i(t+\Delta t) - c_i(t)}{\Delta t} = W_{i,i-1}c_{i-1}(t) + W_{i,i+1}c_{i+1}(t) + W_{i,i}c_i(t), \tag{3.3}$$

where Δt is the time discretization step. We match different spatial discretization schemes: Since experimental concentration data is available at μm-resolution in the epidermis up to a skin depth of 80 μm, we use an equidistant discretization with $\Delta z = 1$ μm in the range $0 < z < 80$ μm. For the transition rates we use [136]

$$W_{i,j} = \frac{D_i + D_j}{2(\Delta z)^2} \exp(-\frac{F_i - F_j}{2k_BT}) \quad \text{with} \quad j = i \pm 1 \tag{3.4}$$

and $W_{i,i} = -W_{i-1,i} - W_{i+1,i}$, which satisfies concentration conservation and detailed balance. We thus have $2 \times 80 = 160$ parameters from the discretized $F(z)$ and $D(z)$ profiles in the epidermal layer. In the HEC gel, which serves as the DXM source during the penetration, no experimental concentration data is available. We discretize the HEC gel with seven sites and a total thickness of 0.4 mm, as in the experiment. We discretize the dermis and the subcutaneous layer, for which also no experimental concentration data is available, with 15 sites and a total thickness of 2 cm, as in the experiment. The total number of discretization sites is $N = 102$. The free energies F_{gel} and F_{derm} and the diffusivities D_{gel} and D_{derm} in the HEC gel and the sub-epidermal layer are assumed to be constant and are treated as free fitting parameters. Reflective boundary conditions are used at the upper gel surface and at the lower sub-dermal boundary, as appropriate for the experimental conditions. The total number of parameters is reduced from 164 to 162 due to the fact that only free-energy differences and diffusivity sums of neighboring sites enter Eq. (3.4). For more details see Sec. 3.4.2. The concentration profile $c_i(t)$ at time $t = n\Delta t$ follows from Eq. (3.3) as

$$c_i(t) = \sum_{j=1}^{N} [(\mathbf{1} + \Delta t \mathbf{W})^n]_{i,j}\, c_j(0) = \sum_{j=1}^{N} \mathrm{e}^{t\mathbf{W}}_{i,j}\, c_j(0) \tag{3.5}$$

where $\mathbf{W}$ is the rate matrix defined in Eq. (3.4) and the continuous limit $\Delta t \rightarrow 0$ has been taken in order to express the n-th power by the matrix exponential. Equation (3.5) can be used to numerically solve the diffusion equation for any initial distribution

$c_j(t=0)$ and diffusivity and free-energy profiles $D(z)$ and $F(z)$. In order to determine $D(z)$ and $F(z)$ based on experimental concentration profiles at different times, we minimize the squared sum of deviations

$$\sigma^2 = \frac{1}{N_\mathrm{p}} \sum_{k=1}^{N_\mathrm{p}} \frac{1}{N_k^\mathrm{data}} \sum_{i=1}^{N_k^\mathrm{data}} \left(c_i^\mathrm{exp}(t_k) - \sum_{j=1}^{N} \mathbf{e}_{i,j}^{t_k \mathbf{W}} c_j(0) \right)^2 , \tag{3.6}$$

where N_k^data is the number of experimental concentration data per profile and $N_\mathrm{p} = 3$ is the number of experimental concentration profiles. We use $N_1^\mathrm{data} = 73$ data points for the 10 min profile and $N_2^\mathrm{data} = N_3^\mathrm{data} = 80$ data points for the 100 and 1000 min profiles, taken from the smoothed splines (black lines) in Fig. 3.2A. The total number of 233= 73+80+80 input data points is necessarily higher than the number of 162 free-energy and diffusivity parameters we need to determine. The profile $c_i(t=0)$ corresponds to the initial condition where DXM is homogeneously distributed in the gel only. For minimization of the error function Eq. (3.6) we use the trust-region iteration approach [90, 167]; see Sec. 3.4.3 for details. As an initial guess for the minimization we use a flat free-energy profile and choose random values for $D(z)$ in the range $[10^{-1}, \ldots, 10^3] \mu\mathrm{m}^2/s$. We perform 1000 runs with different initial values for $D(z)$ with a maximal number of 250 iterations per run. For our results, we only use the best 1% solutions with a residual error $\sigma < 0.6$ μg/(cm$^2\mu$m). A perfect solution with an error of $\sigma = 0$ is never observed, which reflects that our equation system is overdetermined and at the same time input concentration profiles come from different skin samples. In the constant-F and constant-D models we obtains errors $\sigma < 1.6$ μg/(cm$^2\mu$m) and $\sigma < 0.9$ μg/(cm$^2\mu$m) for the best 1% of the solutions, significantly larger than for the full model.

3.4 Supporting Information

3.4.1 DXM concentration profiles from X-ray microscopy

The DXM concentration profiles are generated by soft X-ray absorption spectromicroscopy, which is a label-free technique that yields 2D absolute concentration profiles in thin skin slabs with a lateral resolution below 100 nm [145].

In the sample after 1000 min penetration time the SC is not aligned perpendicularly with respect to the z-axis, as seen in Fig. 3.5A. Therefore, we first apply an affine transformation and shear the 2D profile until the SC is perpendicular to the z-axis, the resulting aligned 2D transmission intensity profile is shown in Fig. 3.5B.

Absolute DXM concentration profiles are derived from the transmission intensity profiles at two different photon energies as described before [145]. The resulting 2D DXM concentration profiles at three different penetration times are shown in Fig. 3.6. For the theoretical analysis we average the 2D concentration profiles along the lateral position x. The resulting 1D concentration profiles are shown in Fig. 3.2.

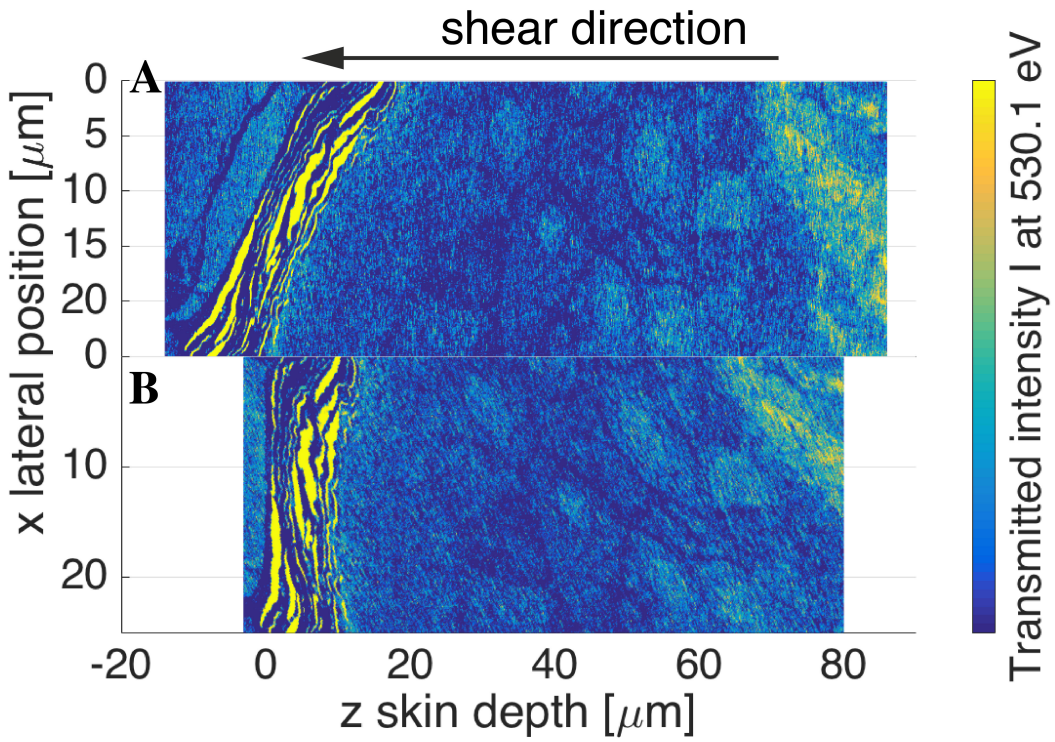

Figure 3.5: (A) 2D transmission intensity profile at photon energy $E = 530.1$ eV after 1000 min penetration time taken directly from X-ray microscopy. The SC is not aligned perpendicularly to the z-axis. (B) Aligned 2D intensity profile after shearing along the z-axis.

To import the experimental data into the inverse diffusion-equation modeling, we apply cubic smoothing splines. This is accomplished by minimizing the sum

$$\sum_{i=1}^{N_k^{\text{data}}} \lambda(c(z_i) - c_{\text{s}}(z_i))^2 + (1-\lambda)\left(c_{\text{s}}(z_{i-1}) - 2c_{\text{s}}(z_i) + c_{\text{s}}(z_{i+1})\right)^2 \tag{3.7}$$

for the 10, 100, and 1000 min profiles, where N_k^{data} is the number of data points in the k-th data set, $c(z)$ is the experimental 1D-concentration profile and $c_{\text{s}}(z)$ is a cubic spline function which serves as an estimator for $c(z)$. The smoothing parameter λ is set to $\lambda = 0.02$, which leads to a sufficient smoothing of the cubic splines, as seen in the main text. We used the cubic smoothing spline function implemented in *Matlab*.

3.4.2 Variable discretization of the 1D diffusion equation

For modeling of the diffusion, we separate the total system into three layers, the HEC gel, the epidermis and the layer underneath that includes the dermis and parts of the subcutaneous fat layer. Experimental measurements are only available within the epidermis over a thickness of ≈ 80 μm. The HEC gel layer and the sub-epidermal layer

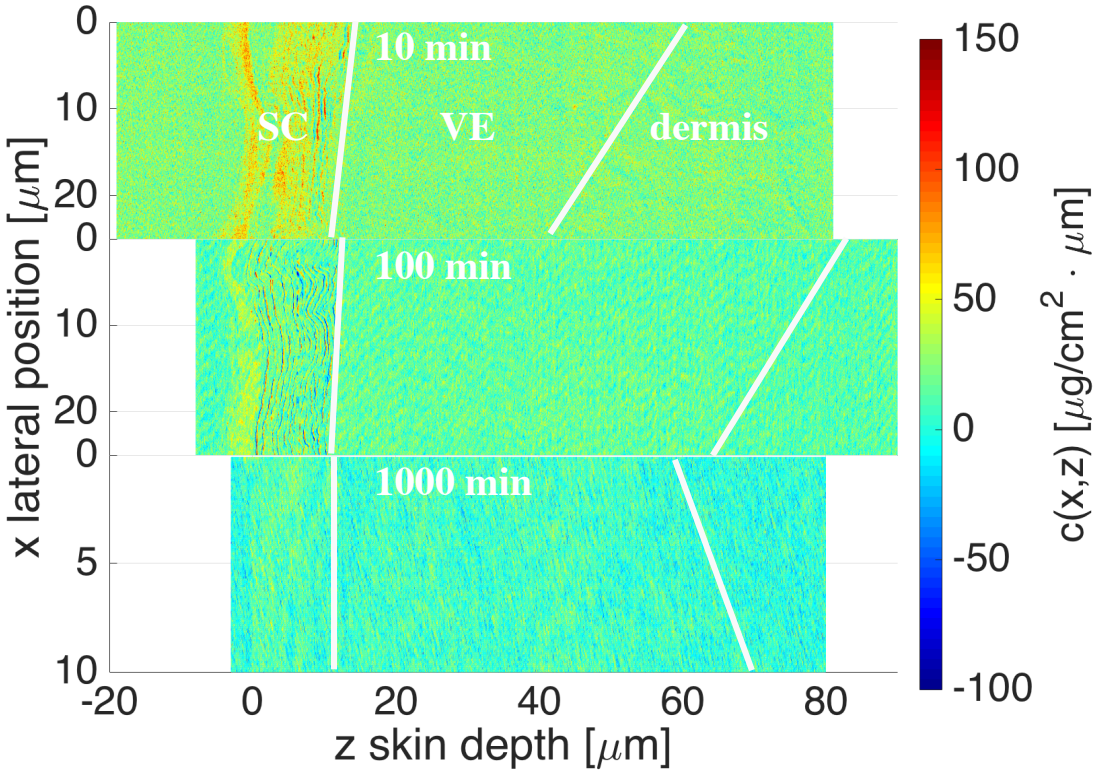

Figure 3.6: Experimental 2D concentration profiles obtained after 10, 100, and 1000 min penetration time. The 1000 min profile has been sheared to achieve perpendicular orientation of the SC with respect to the z-axis. In the 10 and 100 min profiles the inhomogeneous distribution of DXM within the SC is well observed.

(which is called dermis in the remainder for brevity) have thicknesses of 0.4 mm and 2 cm, respectively. We use a constant discretization width of 1 μm for the epidermis and variable discretization width in the HEC gel and the dermis. Note that the free energy and the diffusivity are assumed to be constant in the HEC gel and in the dermis. For constant free energy and diffusivity the diffusion equation reduces to

$$\frac{\partial c(t,z)}{\partial t} = D\frac{\partial^2 c(t,z)}{\partial z^2}. \tag{3.8}$$

We derive a discretized version of Eq. 3.8 for a non-uniform discretization of the spatial coordinate z. Let $\Delta_i = z_i - z_{i-1}$ be the distance between two discretization points. Performing a Taylor expansion up to second order yields

$$c(z_{i+1}) = c(z_i) + \Delta_{i+1}\frac{\partial c(z_i)}{\partial z} + \frac{1}{2}\Delta_{i+1}^2\frac{\partial^2 c(z_i)}{\partial z^2} + O(\Delta_{i+1}^3) \tag{3.9}$$

$$c(z_{i-1}) = c(z_i) - \Delta_i\frac{\partial c(z_i)}{\partial z} + \frac{1}{2}\Delta_i^2\frac{\partial^2 c(z_i)}{\partial z^2} + O(\Delta_i^3). \tag{3.10}$$

Multiplying the first equation with Δ_i and the second equation with Δ_{i+1} and adding both equations gives for the second derivative

$$D\frac{\partial^2 c(z_i)}{\partial z^2} = 2D\Big(\frac{1}{\Delta_{i+1}(\Delta_{i+1}+\Delta_i)}c_{i+1} - \frac{1}{\Delta_{i+1}\cdot\Delta_i}c_i + \frac{1}{\Delta_i(\Delta_{i+1}+\Delta_i)}c_{i-1}\Big) \tag{3.11}$$

$$= W_{i,i+1}c_{i+1} + W_{i,i}c_i + W_{i,i-1}c_{i-1}, \tag{3.12}$$

from which we can read off the rates

$$W_{i,i+1} = 2D\frac{1}{\Delta_{i+1}(\Delta_{i+1}+\Delta_i)} \tag{3.13}$$

$$W_{i,i} = -2D\frac{1}{\Delta_{i+1}\cdot\Delta_i} \tag{3.14}$$

$$W_{i,i-1} = 2D\frac{1}{\Delta_i(\Delta_{i+1}+\Delta_i)}. \tag{3.15}$$

Using Eq. 3.12 we numerically solve the diffusion equation for variable discretization widths in areas of constant free energy and diffusivity. In areas of non-constant free energy and diffusivity but equidistant discretization width, we use the discretization given in the main text.

3.4.3 Trust-region optimization for constrained non-linear problems

In order to obtain the profiles for the free energy $F(z)$ and diffusivity $D(z)$ from the given experimental concentration profiles, we introduce the sum of the squared residuals

$$\sigma^2 = \frac{1}{N_\mathrm{p}}\sum_{k=1}^{N_\mathrm{p}}\frac{1}{N_k^\mathrm{data}}\sum_{i=1}^{N_k^\mathrm{data}}\left(c_i^\mathrm{exp}(t_k) - \sum_{j=1}^{N}\mathrm{e}_{i,j}^{t_k\mathbf{W}}c_j(0)\right)^2 \tag{3.16}$$

$$= \mathbf{R}^T\mathbf{R} = r_1^2 + r_2^2 + \ldots + r_{N_\mathrm{data}}^2, \tag{3.17}$$

where $\mathbf{R}(\mathbf{x})$ is the residual vector containing the errors of the predicted and observed concentrations as a function of $\mathbf{x} = \mathbf{x}(F_1,\ldots,F_{N_\mathrm{param}},D_1,\ldots,D_{N_\mathrm{param}})$. The vector $\mathbf{x}$ has $2N_\mathrm{param}$ and the residual vector has $N_\mathrm{data} = \sum_{k=1}^{N_p} N_k^\mathrm{data}$ components.

In order to minimize Eq. 3.17 we approximate σ^2 by a 1st order Taylor expansion

$$\sigma^2(\mathbf{x}+\mathbf{d}) = Q(\mathbf{d}) \approx \mathbf{R}^T(\mathbf{x}+\mathbf{d})\mathbf{R}(\mathbf{x}+\mathbf{d}) \tag{3.18}$$

with $\mathbf{R}(\mathbf{x}+\mathbf{d}) \approx \mathbf{R}(\mathbf{x}) + \mathbf{J}_R(\mathbf{x})\mathbf{d}$, where $\mathbf{J}$ describes the Jacobian of $\mathbf{R}$ at $\mathbf{x}$ and gives for Q

$$Q(\mathbf{d}) = \sigma^2(\mathbf{x}) + \left(\mathbf{J}^T\mathbf{R}(\mathbf{x})\right)^T\mathbf{d} + \frac{1}{2}\mathbf{d}^T\mathbf{J}^T\mathbf{J}\mathbf{d}, \tag{3.19}$$

with $\mathbf{J}^T\mathbf{R}(\mathbf{x})$ denoting the gradient of $\sigma^2(\mathbf{x})$ and $\mathbf{J}^T\mathbf{J}$ approximating the Hessian of $\sigma^2(\mathbf{x})$. In order to obtain a new approximation in the next iteration step $\mathbf{x}^{m+1} = \mathbf{x}^m + \mathbf{d}$, we *trust* the approximation $Q(\mathbf{d})$ only within a trust-region radius Δ^m depending on the current iteration step m. We state the following trust-region problem

$$\text{Find} \quad \min \quad Q(\mathbf{d}) \quad \text{under the constraint} \quad \|\mathbf{D}^{-1}\mathbf{d}\| < \Delta^m, \tag{3.20}$$

where $\mathbf{D}$ is a scaling matrix that transforms constraints we assume on the solution space of $\mathbf{x}$ or $\mathbf{d}$ into an unconstrained problem $\mathbf{d}_{unc.} = \mathbf{D}^{-1}\mathbf{d}$. Note that two kinds of constraints are introduced: (i) one comes from restricting the parameter space $\mathbf{x}$ to a subspace of $\mathbf{x}$ and the other constraint (ii) comes from minimizing the function $Q(\mathbf{d})$ only within a trust-region Δ. How accurate $\sigma^2(\mathbf{x})$ is approximated by $Q(\mathbf{d})$ can be estimated by the reduction value

$$r^m = \frac{\sigma^2(\mathbf{x}) - \sigma^2(\mathbf{x}+\mathbf{d})}{\sigma^2(\mathbf{x}) - Q(\mathbf{d})}, \tag{3.21}$$

where the numerator describes the actual reduction, and the denominator the predicted reduction. If r is close to 1 the approximation is good and the step $\mathbf{x}^m + \mathbf{d}$ is accepted with an increase of the trust-region Δ^m. If the approximation is bad then $\mathbf{x}^{m+1} = \mathbf{x}^m$ and the trust-region will be decreased.

Finding the minimum of $Q(\mathbf{d})$ within the trust-region radius Δ could be done by applying the Gauss-Newton or steepest-descend algorithm to Q which would involve solving a linear system. We use a so-called dogleg strategy for trust region problems which is a hybrid of Gauss-Newton and steepest descent. At first, we calculate the steepest descent direction and find the steepest point - the Cauchy point - along that direction within the trust-region radius. From the Cauchy point we calculate the vector pointing to the Gauss-Newton point. The intersection between that vector and the trust region boundary is the new point $\mathbf{x}^{m+1}$. We assume no constraints for F but constrain D to $D \in (0, 10^4]$ $\mu\text{m}^2/s$ where the upper bound is four times larger than the diffusion constant of DXM in water. 1,000 runs with 250 iterations per run are performed where only the best 1% of solutions are kept for further analysis. We use the *trust-region reflective* routine implemented in *Matlab*.

3.4.4 Calculating the DXM penetration amount from estimated $F(z)$ and $D(z)$ profiles

The penetrated amount in the epidermis at time t is calculated by

$$C_{\text{epi}}(t) = \int_{0\mu m}^{80\mu m} c(z,t)dz, \tag{3.22}$$

where $c(z,t)$ is approximated by $e^{t\mathbf{W}}_{i,j}c_j(0)$. This yields at time $t = 1000$ min an epidermal DXM amount of ≈ 471.9 $\mu\text{g/cm}^2$. The amount in the dermis at the same time

follows as

$$C_{\text{derm}}(t = 1000min) = \int_{80\mu m}^{2cm} c(z)dz \approx 1.2\mu g/cm^2. \tag{3.23}$$

In the stationary long-time limit the distribution of DXM can be calculated from the free energy alone. The integrated amount of DXM in the dermis in the long-time limit is determined by

$$C_{\text{derm}}^{\text{eq}} = 600\mu g/cm^2 \cdot \frac{1}{Z} \cdot \int_{80\mu m}^{2cm} e^{-\beta F(z)}dz \approx 10.0\mu g/cm^2, \tag{3.24}$$

where the normalization factor is given by

$$Z = \int_{-400\mu m}^{2cm} e^{-\beta F(z)}dz. \tag{3.25}$$

Analogously, the stationary amount in the epidermis follows as $C_{\text{epi}}^{\text{eq}} \approx 465.0\ \mu\text{g/cm}^2$ and in the gel as $C_{\text{gel}}^{\text{eq}} \approx 125.0\ \mu\text{g/cm}^2$.

3.4.5 Estimate of free-energy barrier height between epidermis and dermis

In Fig. 3.7A the error σ of the residual is plotted as a function of the free-energy barrier height $\Delta F_{\text{VE/derm}}$ between viable epidermis and dermis. The error decreases with increasing barrier height and reaches a minimum value of $\sigma \approx 0.57\ \mu\text{g/(cm}^2\mu\text{m)}$, indicated by a horizontal broken line, for a barrier height of $\Delta F_{\text{VE/derm}} = 20.5$ kJ/mol. For larger barrier height the error stays roughly constant, we conclude that the value $\Delta F_{\text{VE/derm}} = 20.5$ kJ/mol constitutes a lower bound for the free-energy barrier between the viable epidermis and the dermis.

The influence of a varying values of $\Delta F_{\text{VE/derm}}$ on the DXM concentration profile in the epidermis is for 1000 min penetration time shown in Fig. 3.7B. For small values of $\Delta F_{\text{VE/derm}}$ the predicted concentration profile is much lower than the experimental profile, which is shown by a dotted line. Only the profiles for $\Delta F_{\text{VE/derm}} = 15$ kJ/mol (green line) and $\Delta F_{\text{VE/derm}} = 20.5$ kJ/mol (red line) get close to the experimental profile.

The same conclusion can be drawn from the integrated DXM amount in the epidermis, which is shown in Fig. 3.7C. For low free-energy barrier $\Delta F_{\text{VE/derm}}$ the integrated DXM amount is much lower than the experimental one since DXM easily penetrates into the dermis. This can in particularly be seen for $\Delta F_{\text{VE/derm}} = 0, 5, 10$ kJ/mol, for which most of the DXM will have penetrated into the dermis and below. We conclude that a sufficient barrier height is crucial in order to hinder DXM penetration into the dermis.

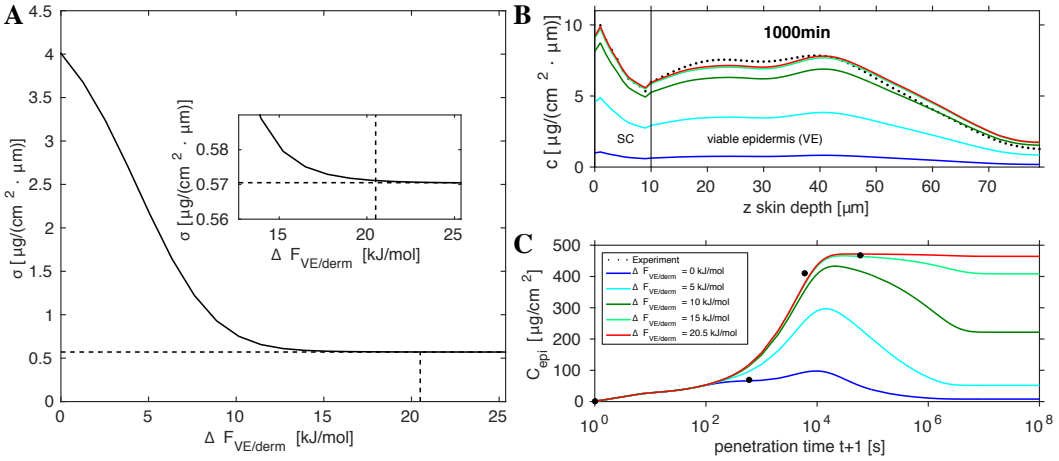

Figure 3.7: **Effect of varying free-energy barrier height $\Delta F_{\mathrm{VE/derm}}$ between VE and dermis** (A) Residual error σ as a function of $\Delta F_{\mathrm{VE/derm}}$. The minimal error $\sigma = 0.571$ μg/(cm$^2\mu$m) is indicated by a dashed horizontal line, which is reached for a free-energy barrier of $\Delta F_{\mathrm{VE/derm}} = 20.5$ kJ/mol, which is indicated by a vertical broken line. (B) 1000-min concentration profiles calculated for different barrier heights $\Delta F_{\mathrm{VE/derm}}$. (C) Integrated amount of DXM in epidermis for different barrier heights $\Delta F_{\mathrm{VE/derm}}$.

3.4.6 Bootstrapping analysis

In the following we do not use the full experimental data set to derive the underlying free-energy and diffusivity profiles. Instead, we reduce the input data set for one penetration time. As described in the main text, there are 164 free-energy and diffusivity parameters we need to estimate. The total number of experimental concentration input data points is $73 + 80 + 80 = 233$. For a least-square algorithm it is important that the number of input data points is equal or larger than the number of unknown parameters, otherwise the matrix $\mathbf{J}^T\mathbf{J}$ is not invertible and the Gauss-Newton step cannot be performed. If we would omit the entire 10 min profile, which consists of 73 data points, we would end up with 160 input data points and thus an underdetermined system. The same holds for omitting the 100 min and 1000 min sample. Therefore, we will not omit an entire profile, but rather omit every data point of that profile except the data in the SC, which contributes with 12 data points.

The minimization protocol is the same as used in the main text: 1,000 runs with 250 iterations, a constant free-energy landscape and arbitrarily chosen diffusivity values D in the interval $[10^{-1}, \ldots, 10^{3}]$ μm$^2/s$ are used as initial guess. Only the best 1% of solutions with the smallest error σ are considered. In Fig. 3.8 the estimated free-energy and diffusivity profiles and the predicted concentration profiles are shown. When reducing the 10 min input data set, we still get accurate results for the concentration profile in the SC, but a higher concentration in the viable epidermis is predicted at 10 min penetration time. For 100 and 1000 min penetration time the prediction is very accurate when compared with the experimental data. The error is calculated to be $\sigma = 0.7$ μg/(cm$^2\mu$m) and thus is only slightly higher than for the case with complete input

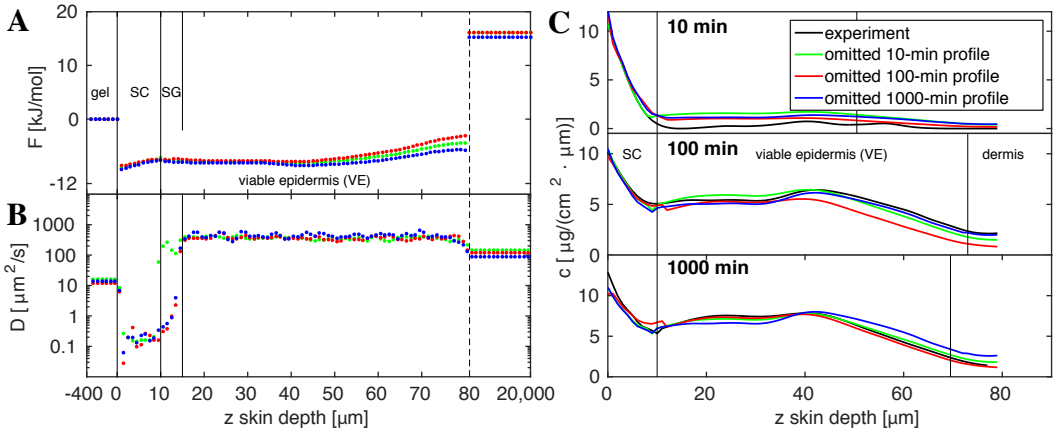

Figure 3.8: **Bootstrapping:** Reducing the input data sets at 10, 100, or 1000 min penetration time produces a higher error σ in the prediction of the concentration profiles but does not drastically change the predicted free-energy profile in (A). The diffusivity profile in (B) is more susceptible to data reduction. (C) Resulting concentration profiles compared with experimental data.

data, leading to an error of $\sigma = 0.6$ μg/(cm$^2\mu$m).

When reducing the 100 min input data set, there is good agreement for the profiles at 10 min and 1000 min penetration time, but the 100 min profile understandably shows larger deviations. The error is $\sigma = 0.7$ μg/(cm$^2\mu$m).

When reducing the 1000 min input data set in the minimization procedure, the agreement for the 10 min profile and the 100 min profile is good with an error of $\sigma = 0.7$ μg/(cm$^2\mu$m), but as one would expect, the deviations at a penetration time of 1000 min are larger.

The free-energy profiles for all three reduced input data sets are quite similar to each other.

All diffusivity profiles for the reduced 10, 100, and 1000 min input data sets show very similar profiles, especially in the SC region. Only the profile for the reduced 10 min data set shows deviations in the SG, where the diffusivity is predicted to be of the same magnitude as in the VE, which explains why more substance has penetrated through the SC into the VE. We conclude that even with reduced input data, the estimated free-energy and diffusivity profiles reproduce the experimental concentration profiles at different times in a satisfactory manner.

Chapter 4

Data-based modeling of drug diffusion in healthy and damaged human skin

Bibliographic information. The content of this chapter is in preparation to be submitted to a peer-reviewed journal (Ref. [iii]).

4.1 Introduction

Organisms contain numerous structurally distinct protective barriers. The largest such barrier is the skin, which is designed to keep most substances out, but allows at the same time desired substances to penetrate [74, 75, 139]. The full understanding of the barrier function of skin is considered a key objective in medicine and drug development. A corrupted skin barrier is considered the main cause for skin diseases such as psoriasis or atopic dermatitis [80, 168].

The structure of human skin can be broadly divided into two layers, the epidermis with a thickness of about 80 - 100 μm, which prevents water loss and provides a barrier against pathogens of all kinds, and the dermis, about 2 mm thick, which protects the human body against mechanical stress and contains hair follices and lymphatic and blood vessels [140], see Fig. 4.1A for a schematic drawing. The epidermis is further divided into the stratum corneum (SC), the 10 - 20 μm thick outermost layer consisting of stratified layers of flattened dead cells (corneocytes), and the viable epidermis (VE). The SC constitutes a key element in the skin barrier function. The structure of the SC has been described as being similar to a wall made of bricks and mortar. The bricks correspond to the corneocytes, whereas the mortar corresponds to the intercellular matrix containing lipid bilayers [169]. In the stratum granulosum (SG), located right underneath the SC and being part of the VE, protein-rich keratinocytes transform into corneocytes.

Over the last decades numerous drug-diffusion models have been developed at different levels of complexity [81–86, 142]. Recently, we introduced a data-based model-

ing approach based on the 1D general diffusion equation, where as the only input drug concentration depth profiles at consecutive times are needed in order to determine all parameters of the model [170]. The diffusion equation describes the evolution of a 1D-concentration profile $c(z,t)$ as a function of depth z and time and depends on the position-dependent free-energy and diffusivity profiles $F(z)$ and $D(z)$,

$$\frac{\partial}{\partial t}c(z,t) = \frac{\partial}{\partial z}\left(D(z)e^{-\beta F(z)}\frac{\partial}{\partial z}c(z,t)e^{\beta F(z)}\right), \tag{4.1}$$

where $\beta = 1/(k_B T)$ is the inverse thermal energy.

The free-energy profile $F(z)$ describes the local affinity and determines how the substance, in our specific case dexamethasone (DXM), partitions in the long-time limit, described by the equilibrium concentration profile $c_{\text{eq}}(z) \propto e^{-\beta F(z)}$. The diffusivity profile $D(z)$ is a local measure of the rate at which the drug would diffuse in a flat free-energy landscape. The model is very general and can be used to describe the diffusion of molecular solutes including water and ions, but also nanoparticles, bacteria, and viruses.

The diffusion equation is used in a variety of different applications such as modeling of marketing strategies [20], decision processes [21], and epigenetic phenotype fluctuations [147]. The position-dependent diffusivity profile $D(z)$ has been shown to be important for e.g. protein-folding dynamics [18, 151–153], particle diffusion at interfaces [19, 150], and membrane transport [148].

In general the diffusion equation can be solved analytically only in very simple limits, whereas for general $F(z)$ and $D(z)$ the solution $c(z,t)$ must be calculated numerically. The inverse problem, i.e. extracting $F(z)$ and $D(z)$ from simulation or experimental concentration profiles, is much more demanding, since inverse problems are generically ill-posed, in the sense that the solution is not unique and sensitive to the noise of the input data [171, 172].

In this paper we pursue two goals: (i) We compare free-energy and diffusivity profiles derived from drug concentration profiles in healthy and damaged skin and (ii) we present a critical test of the robustness of the method to extract free-energy and diffusivity profiles from experimental concentration profiles. For this, we use concentration-depth profiles at three distinct penetration times of the lipophilic antiinflammatory glucocorticoid dexamethasone (DXM) in *ex vivo* human skin. This drug has been chosen since it is frequently used for inflammatory skin diseases [87] and can be detected by label-free X-ray microscopy [145, 146, 173].

The paper is structured as follows.

In Sec. 4.2 we compare results for healthy and damaged skin. We find that the free-energy profiles for healthy and damaged skin are very similar, whereas the diffusivity in the SC is about 200 times larger in damaged skin compared to healthy skin, which results in an enhanced drug penetration at short times and leads to a corrupted skin barrier function. This is an interesting result, as it shows that skin barrier disfunction is primarly a transport property and is not reflected in the equilibrium distribution of molecular solutes.

In Sec. 4.3 we discuss the robustness of our inversion method, based on the concentration profiles of DXM originating from healthy skin. We analyze the behavior of the resulting free-energy and diffusivity profiles when the amount of input data (i.e. the concentration profiles) and the amount of output parameters (i.e. the free-energy and diffusivity profiles) are reduced. As a result, we find that solutions obtained from only one measured concentration profile as input are not robust, whereas for more than one profile the inverse problem becomes well-posed and the resulting free-energy and diffusivity profiles are robust and stable.

After concluding in Sec. 4.4, we briefly describe the experimental set-up in Sec. 4.5 to obtain concentration profiles of DXM in human skin. Here we also provide a description of our inversion method for the generalized diffusion equation and introduce a regularization scheme for our inversion method.

4.2 Results and discussion

4.2.1 Concentration profiles

Our analysis is based on published experimental concentration profiles [170, 173]. In the experimental studies 2-cm-thick abdominal *ex vivo* human skin samples are obtained from a healthy female donor as a byproduct of plastic surgery. At time $t = 0$ a 0.4 mm thick layer of a 70% ethanol HEC gel formulation containing DXM with a concentration of $c_{\text{gel}}(t = 0) = 1.5$ mg/(cm^{2}mm) was applied to the surface of excised human skin for penetration times of 10, 100, and 1000 min at a temperature of $T = 305$ K. 2D-concentration profiles of DXM in skin were obtained by soft X-ray scanning microscopy. The damaged skin was prepared from a healthy skin sample by performing 30 tape-stripping procedures [174, 175] before the HEC gel formulation has been applied on the skin surface. In such a tape-stripping procedure an adhesive tape is pushed onto the skin and then peeled off, which removes and disrupts parts of the SC. A disrupted skin barrier is related to many skin diseases such as psoriasis or atopic dermatitis [80].

In Fig. 4.1B we show 1D DXM concentration profiles for damaged and healthy skin after 10 min penetration time. For healthy skin DXM is only observable in the SC, whereas for damaged skin DXM has already entered the viable epidermis. We will later see that this difference of the penetration behavior is primarly caused by a modification of the diffusive properties of the SC layer and not so much by a change of the free energy profile.

4.2.2 Free-energy and diffusivity profiles

On the basis of 1D DXM concentration profiles at three distinct penetration times, namely 10, 100, and 1000 min, we compare the free-energy and diffusivity profiles for healthy and damaged skin.

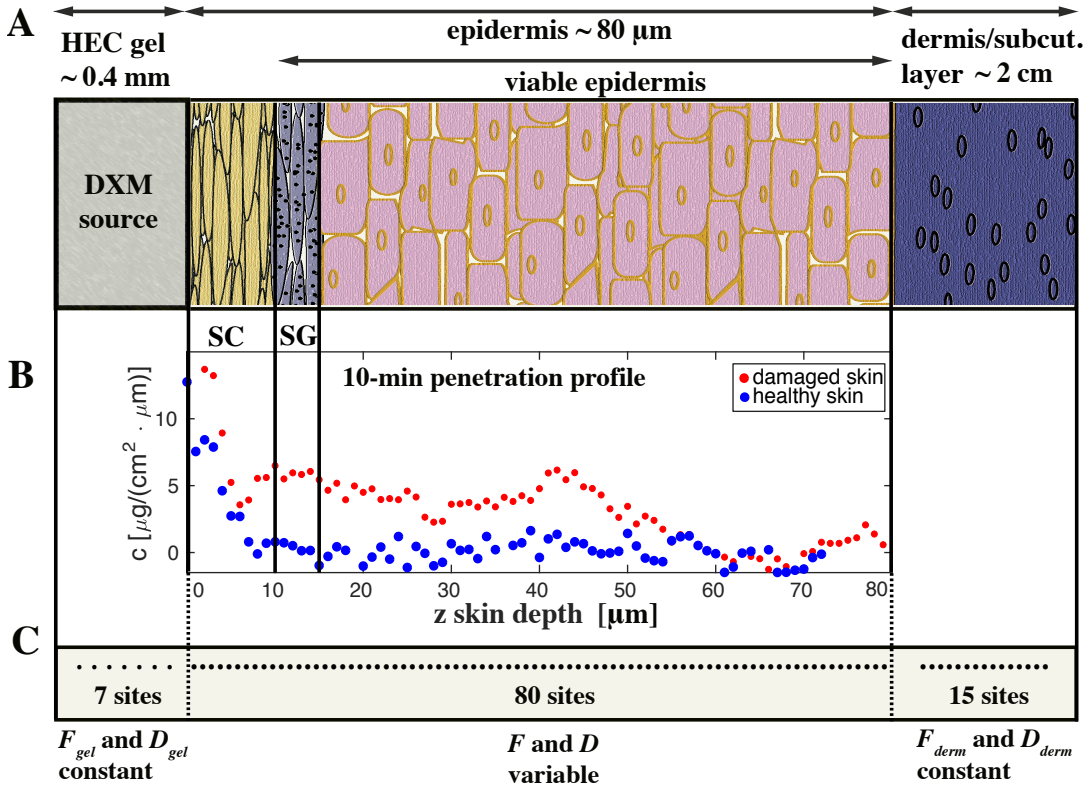

Figure 4.1: **(A)** Sketch of the human skin structure. The 0.4 mm thick HEC gel layer acts as the DXM source. **(B)** Laterally averaged 1D concentration-depth profiles of DXM for damaged (red) and healthy skin (blue) [173]. **(C)** Discretization scheme used in the numerical analysis. The gel is discretized with seven equally spaced sites, the epidermal layer with 80 equally spaced sites, and the dermis and subcutaneous layer with 15 equally spaced sites.

In Fig. 4.2A we plot the concentration-depth profiles of damaged (red dots) and healthy skin (blue dots). Note that all (six) profiles originate from the same donor but from different samples, since an analysis with the same sample at different penetration times is not possible. The position of the outer skin surface of the skin is shifted such that it is located at $z = 0$ μm.

For all skin samples the SC is located between $z = 0$ μm and $z \approx 7 \ldots 10$ μm, which can be inferred from the point at which the DXM concentration stops decreasing and exhibits a rather constant concentration which then marks the beginning of the VE. The VE extends from $z \approx 10$ μm to a variable depth ranging from $z \approx 30$ μm to $z \approx 80$ μm. Note, that the different thickness of the VE is an inherent property of human skin [77]. With increasing skin depth in the VE the concentration starts to decrease again, which marks the transition to the water-rich dermis.

In the 10-min profile in Fig. 4.2A DXM has only penetrated into the SC for healthy skin, whereas for damaged skin DXM has entered already the VE. In the 100 and 1000-

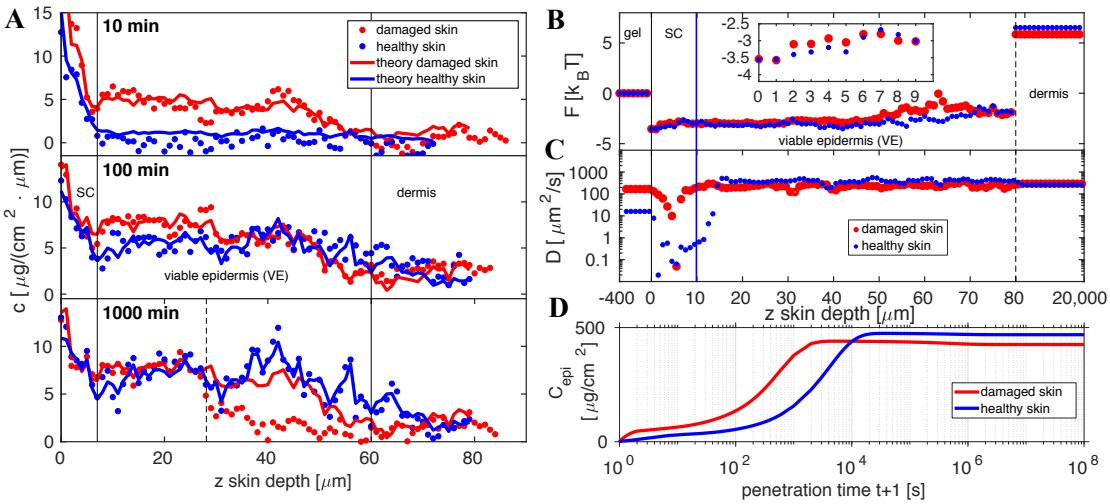

Figure 4.2: (**A**) Experimental input data of damaged (red dots) and healthy skin (blue dots) together with estimated profiles obtained from minimizing Eq. (4.9) from damaged (red) and healthy skin (blue). Only the first 28 μm of the 1000-min profile of damaged skin have been considered in the analysis due to the different position of the dermis in the other profiles. (**B**) Free-energy and (**C**) diffusivity profiles for damaged skin (red dots) compared with healthy skin (blue dots). The most significant difference is observable in the diffusivity profile for damaged skin, which is about a factor of 200 larger in the SC compared to healthy skin. (D) The penetrated amount C_{epi} in the epidermis for damaged skin reaches a maximum already after $t = 2{\cdot}10^3$ s, whereas for healthy skin the maximum is reached only after $t \approx 2{\cdot}10^4$ s.

min profile of healthy skin DXM is found in the VE with only minor differences between the penetration times. The concentration of DXM in the 1000-min profile of damaged skin drops significantly at about $z = 30$ μm which marks the beginning of the dermis.

In order to obtain the free-energy and diffusivity profiles of damaged and healthy skin we feed each set of profiles, at penetration times 10, 100, and 1000 min, into Eq. (4.9), which sums the deviations between the measured and the predicted concentration profiles, and minimize the residual error σ by following the minimization protocol described in Sec. 4.5. The healthy skin samples contribute with 73, 80, and 80 data points for penetration times 10, 100, and 1000 min yielding in total 233 input data points, whereas the damaged skin samples contribute with 80, 80, and 28 data points yielding a total of 188 input data points. Note that we only use the first 28 data points of the 1000-min profile of damaged skin, because of the apparently shifted position of the dermis for this skin sample.

The predicted concentration profiles for damaged skin (red lines) in Fig. 4.2A accurately describe the input data, for the 1000-min sample only up to $z = 28$ μm due to the different location of the dermis. The predicted profiles for healthy skin (blue lines) describe the input data accurately for all three profiles, see Fig. 4.2A.

The free-energy profile of damaged skin (red dots), depicted in Fig. 4.2B, is very sim-

ilar to the one obtained from healthy skin (blue dots). We set the free energy in the gel for healthy and damaged skin to a constant $F_{\text{gel}} = 0$. There is a negative jump between gel and SC of $F_{\text{gel/SC}} = -3.5\ k_{\text{B}}T$, equivalent for healthy and damaged skin, which reflects the fact that the lipophilic drug DXM resides rather in the lipid-rich SC than in the HEC gel. For both healthy and damaged skin, the free energy increases sligthly in the SC, which reflects the structural change within the SC. In the VE, the free energy of healthy and damaged skin stays rather constant up to $z = 50\ \mu$m before it increases slightly up to $z = 80\ \mu$m, which reflects the decreasing concentration profiles in this range, see Fig. 4.2A. At $z = 80\ \mu$m there is a large free-energy barrier of $F^{\text{hel}}_{\text{VE/derm}} = 8.4\ k_{\text{B}}T$ for healthy skin and $F^{\text{dam}}_{\text{VE/derm}} = 7.7\ k_{\text{B}}T$ for damaged skin, which is related to the different affinity of DXM to the water-rich dermis. Consequently, the free-energy difference between gel and dermis comes out as $F^{\text{hel}}_{\text{gel/derm}} = 6.5\ k_{\text{B}}T$ and $F^{\text{dam}}_{\text{gel/derm}} = 5.8\ k_{\text{B}}T$ for healthy and damaged skin, respectively, which is very close to the free-energy difference derived from the maximal solubility of DXM in water, $c_{\text{H}_2\text{O}} = 89\text{mg/L}$ at $25\ ^\circ C$ [161], and the maximal solubility in HEC gel, $c_{\text{H}_2\text{O}} = 15\text{g/L}$, which yields the partition coefficient $k_{\text{B}}T\ln(c_{\text{gel}}/c_{\text{H}_2\text{O}}) \approx 5.1\ k_{\text{B}}T$. This underlines the hydrophilic character of the dermis and the lipophilic character of the viable epidermis. Overall, we note only small deviations in the free-energy profiles between healthy and damaged skin.

The average diffusivity in the SC of healthy skin turns out to be in average $D^{\text{hel}}_{\text{SC}} \approx 0.15\ \mu\text{m}^2/\text{s}$ and maintains such a low value up to a depth of $z = 15\ \mu$m. For $z > 15\ \mu$m the diffusivity is rather constant and about $D_{\text{VE}} \approx 400\ \mu\text{m}^2/\text{s}$, which is sligthly smaller than the diffusivity of DXM in water $D_{\text{DXM/H}_2\text{O}} \approx 680\ \mu\text{m}^2/\text{s}$ [159]. The low diffusivity in the range from $z = 10\ \mu$m up to $z = 15\ \mu$m can be connected to the presence of the SG, since the diffusivity is as low as in the SC, but the concentration profiles in this range are distinct from the concentration profiles in the range from $z = 0\ \mu$m up to $z = 10\ \mu$m, see Fig. 4.2A. We point out that the SG is part of the VE and located right underneath the SC. The diffusivity barrier in the SG is known to be caused by tight junctions [163,164,166] and, thus, we tentatively relate the low diffusivity in the SG to the presence of tight junctions.

The diffusivity profile of damaged skin deviates significantly from healthy skin for depths below $z = 15\ \mu$m. In the SC up to about $z = 7\ \mu$m, the mean diffusivity is about $40\ \mu\text{m}^2/\text{s}$ and thus significantly larger compared to healthy skin. At $z > 7\ \mu$m the diffusivity increases abruptly to $\approx 300\ \mu\text{m}^2/\text{s}$ and this value is maintained throughout the entire VE. Therefore, we tentatively locate the boundary between SC and VE at $z \approx 7\ \mu m$. The diffusivity in the dermis comes out as $D_{\text{derm}} = 300\ \mu\text{m}^2/\text{s}$ and is the same for healthy and damaged skin.

Surprisingly, the diffusivity in the gel turns out to be $D^{\text{dam}}_{\text{gel}} \approx 152\ \mu\text{m}^2/\text{s}$ for damaged skin and $D^{\text{hel}}_{\text{gel}} \approx 16\ \mu\text{m}^2/\text{s}$ for healthy skin. Basically, both gel diffusivities should be the same due to the same gel preparation procedure for healthy and damaged skin. The reason for the different gel diffusivities is due to the absence of experimental concentration profiles in the gel. Therefore, the diffusivity in the gel will be adjusted such a way to reproduce the experimental concentration profiles in the epidermis. In or-

der to more accurately determine the actual gel diffusivity, experimental concentration profiles of DXM in the HEC gel would be needed.

For damaged skin, the enhanced penetration of DXM into the epidermis is most clearly visualized by the integrated amount of DXM in the epidermal layer up to $z = 80$ μm, defined as

$$C_{\text{epi}} = \int_{0\mu\text{m}}^{80\mu\text{m}} c(z)dz. \tag{4.2}$$

The maximum for healthy skin is reached after about $t \approx 2 \cdot 10^4$ s, whereas for damaged skin it is already reached after $t \approx 2 \cdot 10^3$ s, thus, describing roughly a 10-fold increase of the DXM penetration speed into human skin, see Fig. 4.2D.

Concluding, for healthy skin the following results are obtained from our data-based modeling approach: A low diffusivity in the SC and a low diffusivity in the layer underneath the SC that we associate with the SG is observable. In the free energy we reveal a sudden drop at the transition from gel to SC with a slight increase of the free energy in the SC, and a distinct free-energy barrier at the transition from epidermis to dermis.

The free-energy profile for damaged skin shows the same features as for healthy skin, but the diffusivity profile deviates substantially from healthy skin with a much larger diffusivity in the SC, which results in a much faster penetration of DXM into skin. This means that skin damage is primarily manifested in the short-time penetration behavior, which is governed by the diffusivity profile, while the long-time limit penetration and in particular the equilibrium DXM distribution is rather similar for healthy and damaged skin.

4.3 Robustness of model

4.3.1 Estimate of noise amplitude of input data

We estimate the noise amplitude of the experimental input data for healthy skin from the residual between the raw input data $c_i^{\text{exp}}(t_k)$ and the smoothed input data $c_i^{\text{s}}(t_k)$ obtained from cubic smoothing splines [176,177], see Fig. 4.3A. For this we minimize

$$\sum_{i=1}^{N_k^{\text{data}}} \lambda(c_i^{\text{exp}} - c_i^{\text{s}})^2 + (1-\lambda)\left(c_{i-1}^{\text{s}} - 2c_i^{\text{s}} + c_{i+1}^{\text{s}}\right)^2 \tag{4.3}$$

for the 10, 100, and 1000-min profiles with smoothing parameter $\lambda = 0.1$, where c_i^{s} is a cubic spline function. We use the cubic smoothing spline algorithm implemented in Matlab.

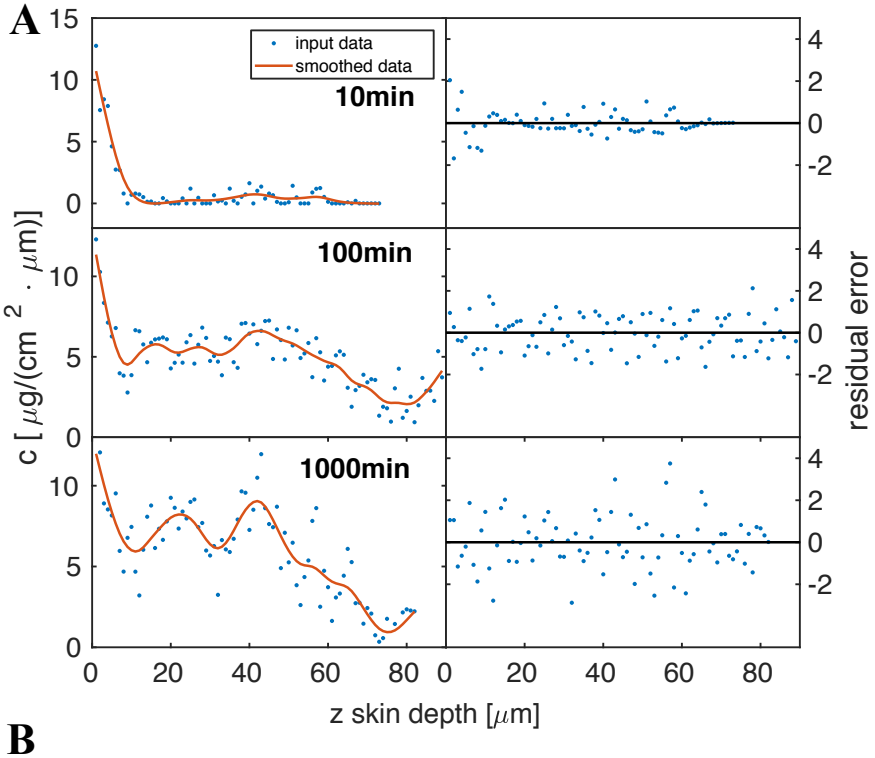

B

profile [min]	10	100	1000	all	10 and 1000
δ [μg/(cm$^2\mu$m)]	0.56	0.86	1.30	0.96	1.0

Figure 4.3: (**A**) (Left) Smoothed experimental DXM concentration profiles (red lines) obtained from smoothing cubic splines at three consecutive penetration times. The blue dots represent the raw experimental input data for healthy skin. (Right) Residual error per data point relative to the cubic smoothing spline. (**B**) Table containing the noise amplitude of every single profile and combinations of profiles.

The absolute squared error we calculate for each profile via

$$\delta_{t_k}^2 = \frac{1}{N_k^{\text{data}}} \sum_{i=1}^{N_k^{\text{data}}} \left(c_i^{\text{exp}}(t_k) - c_i^{\text{s}}(t_k) \right)^2 , \tag{4.4}$$

We obtain for the 10-min profile $\delta_{10\text{min}} = 0.56\ \mu\text{g}/(\text{cm}^2\mu\text{m})$, $\delta_{100\text{min}} = 0.86\ \mu\text{g}/(\text{cm}^2\mu\text{m})$ for the 100-min profile, and $\delta_{1000\text{min}} = 1.30\ \mu\text{g}/(\text{cm}^2\mu\text{m})$ for the 1000-min profile, see table in Fig. 4.3B . The averaged error over the three profiles is

$$\begin{aligned} \bar{\delta}_{\text{all}} &= \sqrt{\frac{1}{3}\left(\delta_{10\text{min}}^2 + \delta_{100\text{min}}^2 + \delta_{1000\text{min}}^2\right)} \\ &= 0.96 \mu\text{g}/(\text{cm}^2\mu\text{m}) \end{aligned} \tag{4.5}$$

and describes an estimate of the noise amplitude of the input data.

4.3.2 Output-parameter reduction

In this section, we analyze the behavior of the solution when the number of output parameters, that means the resolution of the extracted free-energy and diffusivity profiles, in the epidermal layer is reduced, whereas the number of input-parameters, i.e. the resolution of the concentration profiles, is unchanged.

The analysis is based on the 10, 100, and 1000-min profiles of healthy skin, consisting of 73, 80, and 80 data points, yielding a total of 233 input data points, which we feed into our inverse solver defined by Eq. (4.9). We follow the minimization protocol described in Sec. 4.5.1.

We discuss four cases. In the first case (blue lines in Fig. 4.4), we use the raw input profiles $c_i^{\text{exp}}(t_k)$ with an output-parameter resolution Δ_{out} equivalent to the resolution of the input data $\Delta_{\text{in}} = 1\ \mu\text{m}$. This results in $N_{\text{out}} = 164$ parameters to estimate (80 parameters in the epidermis, 1 in the gel, 1 in the dermis/subcutaneous layer for D and F).

In the second case (orange lines in Fig. 4.4), we use the raw input profiles and an output-parameter resolution of $\Delta_{\text{out}} = 10\ \mu\text{m}$, resulting in $N_{\text{out}} = 20$ parameters to estimate. In the third case (green lines in Fig. 4.4), we use the raw input profiles and an output-parameter resolution of $\Delta_{\text{out}} = 80\ \mu\text{m}$, resulting in $N_{\text{out}} = 6$ parameters to estimate.

The set-up in the fourth case (red lines in Fig. 4.4) is equivalent to the first case with $\Delta_{\text{out}} = 1\ \mu\text{m}$, but instead of the raw input data, we use the smoothed profiles $c_i^{\text{s}}(t_k)$ described in the previous section.

The resulting residual errors σ_{exp} defined in Eq. (4.9) are plotted in Fig. 4.4D as a function of the output parameter resolution Δ_{out}. The dashed line indicates the averaged noise amplitude $\bar{\delta}_{\text{all}} = 0.96\ \mu\text{g}/(\text{cm}^2\mu\text{m})$ defined in Eq. (4.5).

As a result, the residual errors σ_{exp} of all different cases are larger than the noise amplitude of the input data. This implies a regularized solution and hence a Tikhonov-regularization according to Eq. (4.11) is not needed.

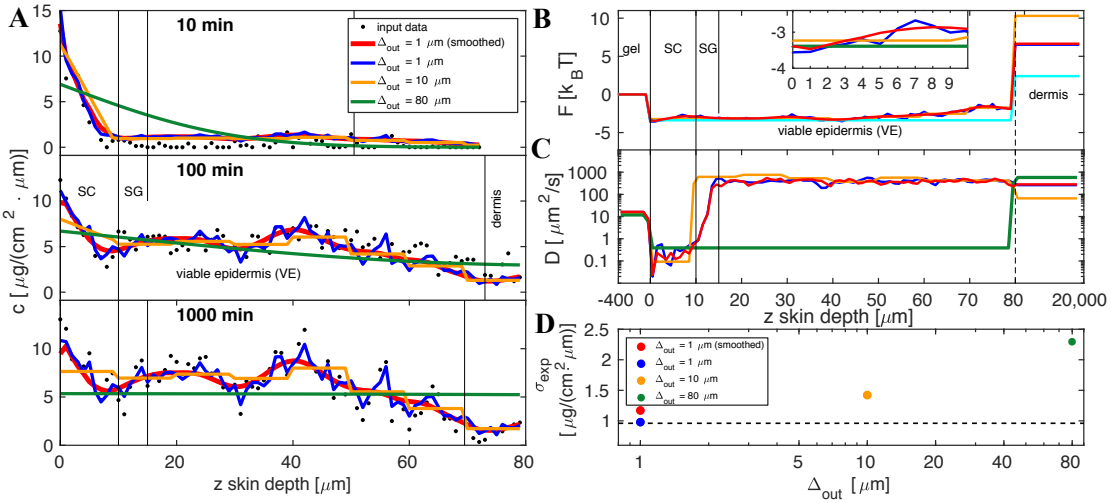

Figure 4.4: Output-parameter reduction. (**A**) Experimental concentration profiles of healthy skin (black dots) for different penetration times. Input data is described accurately for all cases except for $\Delta_{\text{out}} = 80$ μm (green lines). (**B**) Free-energy profiles $F(z)$ and (**C**) diffusivity profiles $D(z)$ derived for different output-parameter resolutions. The smoothed (red) and non-smoothed (blue) free-energy and diffusivity profiles at $\Delta_{\text{out}} = 1$ μm agree very well to each other and underline the robustness of the inversion method, since the slightly different input profiles lead to the same underlying output parameters. The orange profile ($\Delta_{\text{out}} = 10$ μm) shows deviations in the diffusivity profile in the SG and the green profile ($\Delta_{\text{out}} = 80$ μm) deviates significantly compared with the other three cases. (**D**) Numerical errors for different values of output-parameter resolution Δ_{out}. Every result is larger than the noise amplitude $\bar{\delta}_{\text{all}} = 0.96 \mu\text{g}/(\text{cm}^2 \mu\text{m})$ (dashed line) and implies a regularized solution.

The experimental profiles are depicted in Fig. 4.4A. For an output-parameter resolution of $\Delta_{\text{out}} = 1$ μm the input data is fitted accurately, see red and blue lines in Fig. 4.4A. For $\Delta_{\text{out}} = 10$ μm the 100- and 1000-min profiles are described accurately, whereas deviations in the SC at penetration time $t = 1000$ min occur. This arises from the constraint of only one fitting parameter for the free energy in the SC which leads to a flat profile in the SC. When assuming only one fitting parameter for F and D in the entire epidermis ($\Delta_{\text{out}} = 80$ μm) the data is fitted less accurately. Especially in the 1000-min profile (green line) in Fig. 4.4A, a constant profile in the entire epidermal layer is obviously in contradiction to the input data.

When we compare the free-energy and diffusivity profiles in Fig. 4.4B and C originating from smoothed (red) and raw input data (blue) for $\Delta_{\text{out}} = 1$ μm, we observe only minor deviations between the profiles. This fact underlines the robustness of the inversion method, since small differences of the input data result in small changes of the output parameters, which is an indicator of a well-posed problem.

For the case of a parameter resolution $\Delta_{\text{out}} = 10$ μm, see orange lines in Fig. 4.4B and C, the free-energy and diffusivity profiles are similar to the results for $\Delta_{\text{out}} = 1$ μm with the difference that the diffusivity at $z = 10$ μm reaches already the diffusivity value in the epidermal layer ≈ 400 $\mu\text{m}^2/\text{s}$, whereas for $\Delta_{\text{out}} = 1$ μm the value is reached at

$z = 15$ μm.

For an output-parameter resolution of $\Delta_{\text{out}} = 80$ μm, see green lines in Fig. 4.4B and C, the free energy is similar to the ones for finer discretizations, whereas the diffusivity profile deviates significantly in the viable epidermis, which is smaller by a factor of 1000 leading to an insufficient description of the input data in Fig. 4.4A.

From the parameter reduction analysis we conclude that a coarser model up to $\Delta_{\text{out}} = 10$ μm still describes the input data well compared to the full parameterization on the resolution-level of the input data (red and blue curves in Fig. 4.4). For a significantly coarser output-parameter resolution ($\Delta_{\text{out}} = 80$ μm) the deviations between predicted results and experimental data increase markedly.

4.3.3 Input-parameter reduction

In this section, we vary the amount of input data. Throughout this section we only use the raw unsmoothed input data and an output-parameter resolution of $\Delta_{\text{out}} = 4$ μm which results in $N_{\text{out}} = 44$ output parameters to estimate (22 for F and 22 for D). We start with the 10-min profile as the only input which contributes with 73 data points. We follow the minimization protocol described in Sec. 4.5.1. For the residual error we obtain $\sigma_{\text{exp}}^{\text{10min}} = 0.47 \mu\text{g}/(\text{cm}^2 \mu\text{m})$. This error is lower than the noise level of the 10-min profile $\delta_{\text{10min}} = 0.56 \mu\text{g}/(\text{cm}^2 \mu\text{m})$ and implies according to Eq. (4.12) an unregularized solution. This becomes clear when considering the resulting concentration profiles (solid green lines) in Fig. 4.5A. The input data is described well at $t = 10$ min, but no accurate description for the 100 and 1000-min profile is provided. The underlying free-energy and diffusivity profiles show large-scale oscillatory behavior, see Fig. 4.5B and C. The diffusivity in the VE jumps between five orders of magnitude and the free energy exhibits large jumps in the VE as well.

Therefore, we seek to find a Tikhonov-regularized solution by minimizing Eq. (4.11). The best residual errors $\sigma_{\text{exp}}^{\text{10min}}(\alpha)$ as a function of the regularization parameter α are shown in Fig. 4.5D (green dots). For $\alpha \geq 0.15$ the residual error is larger than the noise amplitude and for $\alpha \leq 0.10$ the residual error is below the noise amplitude. According to Eq. (4.12) we choose the value of $\alpha = 0.15$ since it marks the optimal trade-off between an over and under-fitting of the input data. The resulting 10-min profile (dotted green line) matches the input data well, see Fig. 4.5A, but to no surprise the 100 and 1000-min profiles are still not described accurately, since information at these times is not included. However, the free-energy and diffusivity profile show a smoother appearance, but still with significant deviations compared to the full-data description (blue lines).

We conclude that, it is not possible in general to determine a reasonable parameter set from only one measured concentration profile assuming that the concentration profile $c_i(t = 0)$ at $t = 0$ is given.

Next, we use the 10 and 1000-min profiles, which cover the short and long-time limits. The profiles contribute with 73 and 80 data points. The residual error $\sigma_{\text{exp}}^{\text{10,1000min}}(\alpha)$ obtained from minimizing Eq. (4.11) does not fall below the noise amplitude $\delta_{\text{10,1000min}}$

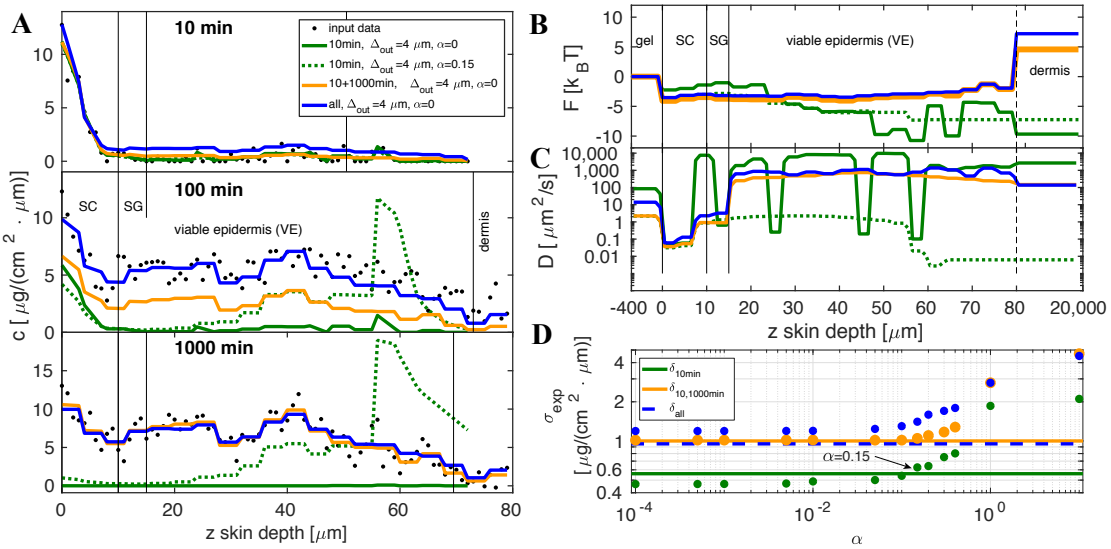

Figure 4.5: (**A**) Raw input data of healthy skin (black dots) and calculated profiles from estimated output parameters free energy and diffusivity. The green profiles, where the 10-min profile is the only input, describe the unregularized (solid green line) and a regularized Tikhonov-solution (dotted green line). Both profiles fit the 10-min profile but large deviations in the 100 and 1000-min profiles arise. When the 10 and 1000-min profiles are used as input (orange lines), the 10 and 1000-min data is fitted well, but a small underestimation of the 100-min profile is observable. When all three profiles are used all input profiles are fitted accurately. (**B**) The unregularized free energy and diffusivity (solid green line) of the 10-min profile show large oscillatory behavior, whereas the Tikhonov-regularized profiles (dotted green line) are smoother, but still provide no reasonable physical interpretation. In the other cases the resulting profiles are very similar. (**C**) Residual errors $\sigma_{\text{exp}}(\alpha)$ obtained from minimizing Eq. (4.11) as a function of the regularization parameter α. The residual of the 10-min profile falls below the noise amplitude of the profile. Thus, a single-input profile results in an unregularized solution. When considering the 10 and 1000-min profile the residual is of the order of the noise amplitude and thus regularized. And when considering all three profiles, the residual becomes larger than the noise amplitude which is also a regularized solution.

for every considered α, see orange dots in Fig. 4.5D. Thus, a Tikhonov-regularization is not required and we discuss the results for $\alpha = 0$. By considering the resulting concentration profiles (orange lines in Fig. 4.5A) we see that the 10 and 1000-min profiles are fitted accurately, but the 100-min profile is slightly underestimated.

For the case where all three profiles are considered (blue lines) with $\alpha = 0$, the input data is fitted accurately in every profile, the resulting free-energy and diffusivity profiles in Fig. 4.5B and C are also well in agreement to the ones in Fig. 4.4B and C (blue lines). The residual error is always larger than the noise amplitude, see Fig. 4.5D.

We conclude that the inversion method with only one profile, shown by the green curves in Fig. 4.5, is ill-posed, whereas for more than one profile the inversion problem constitutes a regularized and well-posed problem, thus, the solution is robust.

4.4 Conclusions

In this paper, we pursued two goals. In the first part, we extracted the free-energy and diffusivity profiles from experimental concentration profiles of the antiinflammatory drug dexamethasone (DXM) in healthy and damaged skin. The estimated free-energy profiles in healthy and damaged skin are very similar, thus, the equilibrium concentration profiles in the long-time limit, which are governed by the free-energy profiles, are predicted to not differ in healthy and damaged skin. In contrast, the diffusivity profiles are significantly different. In fact, the diffusivity in the SC of damaged skin is larger by a factor of 200 compared to healthy skin and gives rise to an accelerated drug penetration into human skin, which dominates in the short-time limit. The larger diffusivity in the SC is the main indicator of a perturbed skin barrier function in the SC.

In the second part, we examined the robustness of our inversion method by which we determined the free-energy and diffusivity profiles of the 1D generalized diffusion equation based on concentration profiles at distinct times as input and discussed the validity of the model. For this, we investigated the effects of a reduction of the output and input parameters and conclude that the inversion method we presented in this paper is robust. Thus, our method is generally applicable to situations where concentration profiles are available.

In the future, a multi-dimensional inversion method incorporating the geometry of the cellular structure of the SC could provide a clearer understanding of penetration pathways. Further, an application of our inversion method to other penetrating substances, particularly hydrophilic substances, could provide better insights into general mechanisms of dug penetration in skin.

4.5 Model and simulation details

4.5.1 Numerical solution and inversion of diffusion equation

For the numerical solution, we discretize the diffusion equation (4.1) in space and time, which gives rise to a Master equation [136]

$$\frac{c_i(t+\Delta t)-c_i(t)}{\Delta t} = W_{i,i-1}c_{i-1}(t) + W_{i,i+1}c_{i+1}(t) + W_{i,i}c_i(t), \tag{4.6}$$

where Δt is the time discretization step. For the transition rates we use [136]

$$W_{i,j} = \frac{D_i + D_j}{2(\Delta z)^2} \exp\left(-\frac{F_i - F_j}{2k_BT}\right) \quad \text{with} \quad j = i \pm 1 \tag{4.7}$$

where the condition $W_{i,i} = -W_{i-1,i} - W_{i+1,i}$ is fulfilled, which implies conservation of concentration and detailed balance. We employ an inhomogeneous spatial discretization scheme. Since the experimental input data is available at $\Delta_{\text{in}} = 1$ μm-resolution in

the epidermal layer up to 80 μm, we use an equidistant discretization with $\Delta z = \Delta_{\text{in}} = 1$ μm in the range $0 < z < 80$ μm. In the HEC gel, which acts as the DXM source during the penetration, no experimental concentration data is available and we therefore discretize the HEC gel with only seven sites for the total thickness of 400 μm. We also discretize the dermis and the subcutaneous layer, for which also no experimental concentration data is available, with 15 sites with a total thickness of 2 cm. This leads to a total number of $N = 102$ discretization sites, see Fig. 4.1C.

We employ different output-parameter discretizations Δ_{out} in the epidermal layer for the free energy and diffusivity, in particular when we discuss the robustness of the model in Sec. 4.3. For the comparison between healthy and damaged skin in Sec. 4.2 the output parameter resolution Δ_{out} in the epidermal layer is equivalent to the input parameter resolution, $\Delta_{\text{out}} = \Delta_{\text{in}} = 1$ μm, which yields 80 parameters for the free energy and 80 parameters for the diffusivity, giving rise to a total of 160 parameters in the epidermis.

The free energies F_{gel} and F_{derm} and the diffusivities D_{gel} and D_{derm} in the HEC gel and the sub-epidermal layer are assumed to be constant, see Fig. 4.1C, and are treated as free fitting parameters. According to the experimental set-up we employ reflective boundary conditions at the upper gel surface and at the lower sub-dermal boundary.

The concentration profile $c_i(t)$ at time $t = n\Delta t$ follows from Eq. (4.6) as

$$c_i(t) = \sum_{j=1}^{N} \left[(\mathbf{1} + \Delta t \mathbf{W})^n\right]_{i,j} c_j(0) = \sum_{j=1}^{N} \mathrm{e}_{i,j}^{t\mathbf{W}} c_j(0) \tag{4.8}$$

where $\mathbf{W}$ is the rate matrix introduced in Eq. (4.7) and we have taken the continuous limit $\Delta t \to 0$ and $n \to \infty$ to express the n-th power by the matrix exponential.

Equation (4.8) can be used to numerically solve the diffusion equation (4.1) for arbitrary diffusivity $D(z)$ and free-energy profiles $F(z)$. As initial distribution $c_j(t = 0)$, we assume that DXM is homogeneously distributed in the gel only. If we want to determine the parameters $D(z)$ and $F(z)$ based on experimental concentration profiles at consecutive times, we seek to minimize the residual error (squared sum of deviations) defined as

$$\sigma_{\text{exp}}^2 = \frac{1}{N_{\text{p}}} \sum_{k=1}^{N_{\text{p}}} \frac{1}{N_k^{\text{data}}} \sum_{i=1}^{N_k^{\text{data}}} \left(c_i^{\text{exp}}(t_k) - \sum_{j=1}^{N} \mathrm{e}_{i,j}^{t_k \mathbf{W}} c_j(0) \right)^2 , \tag{4.9}$$

where N_k^{data} is the number of experimental concentration data per profile and N_{p} is the number of experimental concentration profiles.

For the minimization of the residual error, Eq. (4.9), we use the trust-region algorithm [90, 167]. We adapt the following minimization protocol: As an initial guess we use a flat free energy profile and choose random values for the diffusivity $D(z)$ in the range $[10^{-1}, \ldots, 10^{4}]$ $\mu\text{m}^2/\text{s}$. We perform 400 runs with different initial values for $D(z)$ with a maximal number of 250 iterations per run, where we only use the best 1% of the resulting solutions for $F(z)$ and $D(z)$.

4.5.2 Regularization of the inverse problem

Usually one solves partial differential equations such as the diffusion equation in Eq. (4.1) for the concentration $c_i(t)$ at time t for given free-energy $F(z)$ and diffusivity profiles $D(z)$, an initial condition $c_i(t=0)$, and boundary conditions. This is an example of a well-posed problem. However, the inverse problem, where profiles at different times are given, but the underlying free energy and diffusivity are unknown, can be ill-posed in the sense that the solution is not unique or sensitive to noise present in the input data.

One way to overcome issues arising from an ill-posed problem is to seek a regularized solution, for which numerous approaches exist [171, 178–182]. The general idea is to introduce an additional term in the functional in Eq. (4.9) that renders the problem well-defined. This can be achieved by introducing the penalty term

$$\sigma^2_{\text{pen}} = \sum_{j=1}^{N_{\text{out}}/2-1} (F_j - F_{j+1})^2 + \sum_{j=1}^{N_{\text{out}}/2-1} (D_j - D_{j+1})^2 \tag{4.10}$$

where N_{out} is the total number of output parameters. This penalty term ensures smoothness of the output parameters, namely the free energy $F(z)$ and diffusivity profile $D(z)$, and is added to Eq. (4.9) and controlled by the regularization parameter $\alpha \in [0, \infty)$ yielding the regularized expression

$$\sigma^2_{\text{reg}} = \sigma^2_{\text{exp}} + \alpha\sigma^2_{\text{pen}}. \tag{4.11}$$

This regularization scheme is called *Tikhonov*-regularization [172]. For small α the weight is shifted to σ^2_{exp} which can result in an over-fitting of the input data. In contrast, when α is large the actual input data has less weight and the minimization tends toward flat profiles, resulting in an under-fitting of the input data.

The choice of α is typically based on heuristic arguments [183–188]. For non-linear problems, as in Eq. (4.9), a discrepancy principle has been proven useful [189–191]. This principle describes a selection rule for the regularization parameter $\alpha = \alpha(\delta)$ as a function of the estimated noise amplitude δ of the input data $c_i^{\text{exp}}(t_k)$. The rule is given in terms of the inequality

$$\sigma_{\text{exp}}(\alpha) \geq \delta, \tag{4.12}$$

where $\sigma_{\text{exp}}(\alpha)$ is the residual error of the regularized solution obtained by minimizing Eq. (4.11). Eq. (4.12) demands that the residual error $\sigma_{\text{exp}}(\alpha)$ should be larger than the actual noise amplitude of the input data.

Chapter 5

Summary and Outlook

In this thesis we pursue a description of diffusion processes on both the microscopic and mesoscopic level.

In Chapter 2, we analyze the structural dynamics in liquid water. Based on classical molecular dynamics simulations of SPC/E water, we investigate water dynamics in the 12-dimensional continuum space of a water trimer. Using Markov state modeling, we identify different processes and time scales, and relate them to rearrangements of hydrogen-bond (H-bond) configurations. The slowest processes are identified as donor-acceptor, acceptor-acceptor, and double donor/acceptor interchanges, which describe the breaking and forming of at least two H-bonds. Thus, slow water kinetics consists either of single-water or collective reorientations of water molecules.

Using a projection onto H-bond states, we derive a Markov state model in a much restricted state space and analyze the switching of an H-bond from one accepting water molecule to a second accepting water molecule. From this, we decompose all possible H-bond switching pathways using transition path analysis. The main transition pathways correspond to a direct switch between H-bond acceptors without a broken H-bond as an intermediate state, making up about $2/3$ of all possible transitions. The other $1/3$ of all possible transitions splits into non-H-bond intermediate states ($\approx 26\%$) and in alternative ($\approx\ 5\%$) H-bond rearrangements as intermediate states. The dominant transition pathways we find for the single H-bond switch are consistent with previous results [37, 58, 59], but the analysis by a Markov state model allows to describe a more complete picture of the H-bond rearrangement dynamics. Quantum calculations for isolated clusters at zero temperature [114–116] suggested that H-bond rearrangements are local and do not involve more than three water molecules. Therefore, an analysis of tetra- or pentamers using Markov state models would be interesting to check if H-bond rearrangements involving more than three water molecules in the liquid phase exist. We point out that in our simulation trajectories are obtained from classical force field simulations, which neglect quantum effects, and provide an acceptable approximation at the time scale we are investigating [132, 133].

In Chapter 3, based on the general 1D diffusion equation, we derive a data-based

method for extracting free-energy and diffusivity profiles from experimental concentration profiles using the example of the drug dexamethasone. For this we numerically invert the diffusion equation by solving a corresponding least-square problem. The approach is generally applicable to various diffusing substances whenever spatially-resolved concentration profiles at different times are available. For the specific example of concentration depth profiles of dexamethasone in human skin measured at three consecutive penetration times (10, 100, and 1000 min), our results show that both the free-energy and diffusivity profiles are needed to accurately model the skin barrier and experimental input profiles. In particular, the free-energy profile is essential to correctly describe the long-time concentration profiles, while the diffusivity profile is needed to reproduce the short-time behavior. Our method reveals that epidermal skin barrier function against the permeation of dexamethsone relies on the combination of two aspects, namely a low diffusivity in the stratum corneum (the outermost skin layer) and a low free energy in the entire epidermal layer. Each of these properties by itself severely reduces the permeation of dexamethasone through the epidermis and, thus, reflects the exceptionally slow transport of the drug dexamethasone into the dermis (the layer underneath the epidermis). This constitutes two major challenges for the design of drug delivery methods. Firstly, the free-energy barrier from the lipophilic epidermis to the hydrophilic dermis slows down the permeation rate of lipophilic drugs such as dexamethasone, and secondly, the low diffusivity in the stratum corneum needs to be overcome. A promising approach would consist of a modified drug with amphiphilic character in order to effectively remove the free-energy barrier from epidermis to dermis.

In Chapter 4, we also consider drug transport in skin and pursue two goals. Namely, a comparison between the extracted free-energy and diffusivity profiles from experimental concentration profiles of dexamethasone in healthy and damaged skin, and the examination of the robustness of our inversion method presented in Chapter 3. The resulting free-energy profiles in damaged and healthy skin show almost no differences. This implies that the long-time limit of the concentration profiles originating from damaged and healthy skin is the same. On the other hand, the diffusivity profiles deviate significantly between healthy and damaged skin. In particular, the diffusivity in the stratum corneum of damaged skin is larger by a factor of 200 compared to healthy skin and gives rise to an accelerated drug penetration into human skin. This feature is only reflected in the short-time limit. Therefore, the skin barrier dysfunction is mainly a transport property. In the second part of this chapter, we examine the robustness of our inversion method. For this, we investigate the effects of coarse-graining the output parameters, namely the free-energy and diffusivity profiles, as well as a reduction of the input parameters, namely the number of concentration profiles. We find that the inversion method we presented in Chapter 3 is robust, so that our method is generally applicable to systems in which concentration profiles are analyzed.

In the future, a multi-dimensional inversion method incorporating the geometry of the cellular structure of the stratum corneum could provide a clearer understanding

of penetration pathways. Further, an application of our inversion method to other penetrating substances, particularly hydrophilic and amphiphilic substances, could provide better insights into general mechanisms of drug penetration in skin. The free-energy and diffusivity profiles obtained in such studies could then be used in coarse-grained diffusion modeling, in order to obtain a more complete understanding of locally-resolved skin properties.

List of Publications

The present thesis is based on the following manuscripts, which have been published or are in preparation for publication in peer-reviewed journals:

[i] Robert Schulz, Yann von Hansen, Jan O. Daldrop, Julian Kappler, Frank. Noé and Roland R. Netz, "Collective hydrogen-bond rearrangements in liquid water", in preparation

[ii] Robert Schulz, Kenji Yamamoto, André Klossek, Roman Flesch, Stefan Hönzke, Fiorenza Rancan, Annika Vogt, Ulrike Blume-Peytavi, Sarah Hedtrich, Monika Schäfer-Korting, Eckart Rühl and Roland R. Netz, "Data-based modeling of drug penetration relates human skin barrier function to the interplay of diffusivity and free-energy profiles", *Proc. Natl. Acad. Sci. U.S.A.*, vol. 114, pp. 3631-3636, **2017**
DOI: 10.1073/pnas.1620636114

[iii] Robert Schulz, Roland R. Netz, "Data-based modeling of drug diffusion in healthy and damaged human skin", in preparation

The following publication is not discussed in the present thesis:

[iv] Robert Schulz, Benjamin Werner and Ulrich Behn, "Self-Tolerance in a Minimal Model of the Idiotypic Network", *Front. Immunol.*, vol. 5, **2014**
DOI: 10.3389/fimmu.2014.00086

Bibliography

[1] Y. von Hansen, F. Sedlmeier, M. Hinczewski, and R. R. Netz, "Friction contribution to water-bond breakage kinetics," *Phys. Rev. E*, vol. 84, Nov 2011.

[2] D. S. Banks and C. Fradin, "Anomalous diffusion of proteins due to molecular crowding," *Biophys. J.*, vol. 89, pp. 2960–2971, nov 2005.

[3] D. Merritt, *Dynamics and Evolution of Galactic Nuclei (Princeton Series in Astrophysics)*. Princeton University Press, 2013.

[4] F. Black and M. Scholes, "The pricing of options and corporate liabilities," *Journal of Political Economy*, vol. 81, pp. 637–654, may 1973.

[5] R. C. Merton, "Theory of rational option pricing," in *Theory of Valuation*, pp. 229–288, WORLD SCIENTIFIC, jul 2005.

[6] E. M. Rogers, *Diffusion of Innovations, 5th Edition*. Free Press, 2003.

[7] A. Bunde, J. Caro, J. Kärger, and G. Vogl, *Diffusive Spreading in Nature, Technology and Society*. Springer, 2017.

[8] T. Graham, "A short account of experimental researches on the diffusion of gases through each other, and their separation by mechanical means," *Quart. J. Sci., Lit. a. Art*, vol. 27, pp. 74–83, 1829.

[9] T. Graham, "On the law of the diffusion of gases," *Philos. Mag.*, pp. 175–190, 1833.

[10] J. C. Maxwell, "On the dynamical theory of gases," *Philos. Trans. R. Soc. Lond. B. Biol. Sci.*, vol. 157, pp. 49–88, jan 1867.

[11] A. Fick, "Ueber diffusion," *Ann. Phys.*, vol. 170, no. 1, pp. 59–86, 1855.

[12] A. Einstein, "Über die von der molekularkinetischen theorie der wärme geforderte bewegung von in ruhenden flüssigkeiten suspendierten teilchen," *Ann. Phys.*, vol. 322, no. 8, pp. 549–560, 1905.

[13] M. von Smoluchowski, "Zur kinetischen theorie der brownschen molekularbewegung und der suspensionen," *Ann. Phys.*, vol. 326, no. 14, pp. 756–780, 1906.

[14] R. Brown, "A brief account of microscopical observations made in the months of june, july and august 1827, on the particles contained in the pollen of plants, and on the general existence of active molecules in organic and inorganic bodies," *Phil. Mag.*, vol. 4, pp. 161–173, sep 1828.

[15] J. B. Perrin, "L'agitation moléculaire et le mouvement brownien," *C. R. Acad. Sci*, vol. 146, pp. 967–970, 1908.

[16] J. B. Perrin, "Mouvement brownien et réalité moléculaire," *Ann. Chim. Phys.*, vol. 18, pp. 1–114, 1909.

[17] E. Frey and K. Kroy, "Brownian motion: a paradigm of soft matter and biological physics," *Ann. Phys.*, vol. 14, pp. 20–50, feb 2005.

[18] R. Best and G. Hummer, "Coordinate-dependent diffusion in protein folding," *Proc. Natl. Acad. Sci. U.S.A.*, vol. 107, p. 1088, 2010.

[19] P. Liu, E. Harder, and B. Berne, "On the calculation of diffusion coefficients in confined fluids and interfaces with an application to the liquid-vapor interface of water," *J. Phys. Chem. B*, vol. 108, p. 6595, 2004.

[20] F. M. Bass, "A new product growth for model consumer durables," *Management Science*, vol. 15, p. 215, 1969.

[21] R. Ratcliff and G. McKoon, "The diffusion decision model: Theory and data for two-choice decision tasks," *Neural. Comput.*, vol. 20, p. 873, 2008.

[22] H. Risken and T. Frank, *The Fokker-Planck Equation: Methods of Solution and Applications (Springer Series in Synergetics)*. Springer, 1996.

[23] M. V. Smoluchowski, "über brownsche molekularbewegung unter einwirkung äußerer kräfte und deren zusammenhang mit der verallgemeinerten diffusionsgleichung," *Ann. Phys.*, vol. 353, no. 24, pp. 1103–1112, 1916.

[24] K. Itô, "Stochastic integral," *Proc. Imp. Acad.*, vol. 20, no. 8, pp. 519–524, 1944.

[25] R. L. Stratonovich, "A new representation for stochastic integrals and equations," *SIAM J. Control*, vol. 4, pp. 362–371, may 1966.

[26] D. S. Lemons and A. Gythiel, "Paul langevin's 1908 paper "on the theory of brownian motion" ["sur la théorie du mouvement brownien," c. r. acad. sci. (paris) 146, 530–533 (1908)]," *Am. J. Phys.*, vol. 65, pp. 1079–1081, nov 1997.

[27] N. G. van Kampen, "Itô versus stratonovich," *J. Stat. Phys.*, vol. 24, pp. 175–187, jan 1981.

[28] P. Ball, "Water as an active constituent in cell biology," *Chem. Rev.*, vol. 108, pp. 74–108, Jan 2008.

[29] P. Ball, "Water is an active matrix of life for cell and molecular biology," *Proc. Natl. Acad. Sci. U.S.A.*, vol. 114, pp. 13327–13335, jun 2017.

[30] G. B. Forbes, *Human Body Composition: Growth, Aging, Nutrition, and Activity*. Springer, 2011.

[31] K. R. Segal, S. Burastero, A. Chun, P. Coronel, R. N. Pierson, and J. Wang, "Estimation of extracellular and total body water by multiple-frequency bioelectrical-impedance measurement," *Am. J. Clin. Nutr.*, vol. 54, pp. 26–29, jul 1991.

[32] D. H. Wertz and H. A. Scheraga, "Influence of water on protein structure. an analysis of the preferences of amino acid residues for the inside or outside and for specific conformations in a protein molecule," *Macromolecules*, vol. 11, pp. 9–15, jan 1978.

[33] Y. Duan, "Pathways to a protein folding intermediate observed in a 1-microsecond simulation in aqueous solution," *Science*, vol. 282, pp. 740–744, oct 1998.

[34] C. M. Dobson, "The structural basis of protein folding and its links with human disease," *Philos. Trans. R. Soc. Lond. B Biol. Sci.*, vol. 356, pp. 133–145, feb 2001.

[35] D. J. Selkoe, "Folding proteins in fatal ways," *Nature*, vol. 426, pp. 900–904, dec 2003.

[36] A. Witze, "Icy enceladus hides a watery ocean," *Nature*, apr 2014.

[37] D. Laage and J. T. Hynes, "On the molecular mechanism of water reorientation," *J. Phys. Chem. B*, vol. 112, pp. 14230–14242, Nov 2008.

[38] A. Luzar and D. Chandler, "Hydrogen-bond kinetics in liquid water," *Nature*, vol. 379, no. 6560, p. 55, 1996.

[39] A. Otten and S. Herminghaus, "How plants keep dry: A physicist's point of view," *Langmuir*, vol. 20, pp. 2405–2408, mar 2004.

[40] A. Soper, E. Castner, and A. Luzar, "Impact of urea on water structure: a clue to its properties as a denaturant?," *Biophys. Chem.*, vol. 105, pp. 649–666, sep 2003.

[41] J. L. Finney, "Water? what's so special about it?," *Philos. Trans. Royal Soc. B*, vol. 359, no. 1448, pp. 1145–1165, 2004.

[42] J. Grdadolnik, F. Merzel, and F. Avbelj, "Origin of hydrophobicity and enhanced water hydrogen bond strength near purely hydrophobic solutes," *Proc. Natl. Acad. Sci. U.S.A.*, vol. 114, pp. 322–327, dec 2016.

[43] G. Stirnemann, P. J. Rossky, J. T. Hynes, and D. Laage, "Water reorientation, hydrogen-bond dynamics and 2d-IR spectroscopy next to an extended hydrophobic surface," *Faraday. Discuss.*, vol. 146, p. 263, 2010.

[44] P. Debye, "Polar molecules," *J. Soc. Chem. Ind.*, vol. 48, pp. 1036–1037, oct 1929.

[45] S. Woutersen, "Femtosecond mid-IR pump-probe spectroscopy of liquid water: Evidence for a two-component structure," *Science*, vol. 278, pp. 658–660, oct 1997.

[46] H.-K. Nienhuys, R. A. van Santen, and H. J. Bakker, "Orientational relaxation of liquid water molecules as an activated process," *J. Chem. Phys.*, vol. 112, pp. 8487–8494, may 2000.

[47] H. J. Bakker and J. L. Skinner, "Vibrational spectroscopy as a probe of structure and dynamics in liquid water," *Chem. Rev.*, vol. 110, no. 3, pp. 1498–1517, 2010.

[48] C. J. Fecko, J. J. Loparo, S. T. Roberts, and A. Tokmakoff, "Local hydrogen bonding dynamics and collective reorganization in water: Ultrafast infrared spectroscopy of hod/d2o," *J. Chem. Phys.*, vol. 122, no. 5, p. 054506, 2005.

[49] J. Jonas, T. DeFries, and D. J. Wilbur, "Molecular motions in compressed liquid water," *J. Chem. Phys.*, vol. 65, pp. 582–588, jul 1976.

[50] J. Ropp, C. Lawrence, T. C. Farrar, and J. L. Skinner, "Rotational motion in liquid water is anisotropic: A nuclear magnetic resonance and molecular dynamics simulation study," *J. Am. Chem. Soc.*, vol. 123, pp. 8047–8052, aug 2001.

[51] J. Teixeira, M.-C. Bellissent-Funel, S. H. Chen, and A. J. Dianoux, "Experimental determination of the nature of diffusive motions of water molecules at low temperatures," *Phys. Rev. A*, vol. 31, pp. 1913–1917, mar 1985.

[52] D. D. Cola, A. Deriu, M. Sampoli, and A. Torcini, "Proton dynamics in supercooled water by molecular dynamics simulations and quasielastic neutron scattering," *J. Chem. Phys.*, vol. 104, pp. 4223–4232, mar 1996.

[53] C. Rønne, P.-O. Åstrand, and S. R. Keiding, "THz spectroscopy of liquid H2O and D2O," *Phys. Rev. Lett.*, vol. 82, pp. 2888–2891, apr 1999.

[54] J. Barthel, K. Bachhuber, R. Buchner, and H. Hetzenauer, "Dielectric spectra of some common solvents in the microwave region. water and lower alcohols," *Chem. Phys. Lett.*, vol. 165, no. 4, pp. 369 – 373, 1990.

[55] B. J. Alder and T. E. Wainwright, "Studies in molecular dynamics. i. general method," *J. Chem. Phys.*, vol. 31, pp. 459–466, aug 1959.

[56] H. J. C. Berendsen, J. P. M. Postma, W. F. van Gunsteren, and J. Hermans, "Interaction models for water in relation to protein hydration," in *The Jerusalem Symposia on Quantum Chemistry and Biochemistry*, pp. 331–342, Springer Netherlands, 1981.

[57] F. H. Stillinger, "Water revisited," *Science*, vol. 209, no. 4455, pp. 451–457, 1980.

[58] F. S. Csajka and D. Chandler, "Transition pathways in a many-body system: Application to hydrogen-bond breaking in water," *J. Chem. Phys.*, vol. 109, no. 3, p. 1125, 1998.

[59] D. Laage, "A molecular jump mechanism of water reorientation," *Science*, vol. 311, pp. 832–835, Feb 2006.

[60] Y. Sugita and Y. Okamoto, "Replica-exchange molecular dynamics method for protein folding," *Chem. Phys. Lett.*, vol. 314, pp. 141–151, nov 1999.

[61] P. G. Bolhuis, D. Chandler, C. Dellago, and P. L. Geissler, "Transition path sampling: Throwing ropes over rough mountain passes, in the dark," *Annu. Rev. Phys. Chem.*, vol. 53, pp. 291–318, oct 2002.

[62] S. Kumar, J. M. Rosenberg, D. Bouzida, R. H. Swendsen, and P. A. Kollman, "THE weighted histogram analysis method for free-energy calculations on biomolecules. i. the method," *Journal of Computational Chemistry*, vol. 13, pp. 1011–1021, oct 1992.

[63] W. Paul and J. Baschnagel, *Stochastic Processes: From Physics to Finance*. Springer, 2013.

[64] F. Noé, C. Schütte, E. Vanden-Eijnden, L. Reich, and T. R. Weikl, "Constructing the equilibrium ensemble of folding pathways from short off-equilibrium simulations," *Proc. Natl. Acad. Sci. U.S.A.*, vol. 106, pp. 19011–19016, Nov 2009.

[65] C. R. Schwantes and V. S. Pande, "Improvements in markov state model construction reveal many non-native interactions in the folding of NTL9," *J. Chem. Theory Comput.*, vol. 9, pp. 2000–2009, mar 2013.

[66] G. R. Bowman, K. A. Beauchamp, G. Boxer, and V. S. Pande, "Progress and challenges in the automated construction of markov state models for full protein systems," *J. Chem. Phys.*, vol. 131, p. 124101, sep 2009.

[67] I. Buch, T. Giorgino, and G. D. Fabritiis, "Complete reconstruction of an enzyme-inhibitor binding process by molecular dynamics simulations," *Proc. Natl. Acad. Sci. U.S.A.*, vol. 108, pp. 10184–10189, jun 2011.

[68] M. Weber, A. Bujotzek, and R. Haag, "Quantifying the rebinding effect in multivalent chemical ligand-receptor systems," *J. Chem. Phys.*, vol. 137, p. 054111, aug 2012.

[69] C. Gu, H.-W. Chang, L. Maibaum, V. S. Pande, G. E. Carlsson, and L. J. Guibas, "Building markov state models with solvent dynamics," *BMC Bioinformatics*, vol. 14, no. Suppl 2, p. S8, 2013.

[70] P. Hamm, "Markov state model of the two-state behaviour of water," *J. Chem. Phys.*, vol. 145, p. 134501, oct 2016.

[71] F. Noé, "Probability distributions of molecular observables computed from markov models," *J. Chem. Phys.*, vol. 128, p. 244103, jun 2008.

[72] H. J. C. Berendsen, J. R. Grigera, and T. P. Straatsma, "The missing term in effective pair potentials," *J. Phys. Chem.*, vol. 91, pp. 6269–6271, nov 1987.

[73] R. Phillips, J. Kondev, J. Theriot, and H. Garcia, *Physical Biology of the Cell*. Garland Science, 2012.

[74] G. Cevc and U. Vierl, "Nanotechnology and the transdermal route: A state of the art review and critical appraisal," *J. Control. Release*, vol. 141, p. 277, 2010.

[75] O. Lieleg and K. Ribbeck, "Biological hydrogels as selective diffusion barriers," *Trends Cell Biol.*, vol. 21, p. 543, 2011.

[76] W. M. Pardridge, "The blood-brain barrier: Bottleneck in brain drug development," *NeuroRX*, vol. 2, pp. 3–14, jan 2005.

[77] J. Sandby-Møller, T. Poulsen, and H. C. Wulf, "Epidermal thickness at different body sites: relationship to age, gender, pigmentation, blood content, skin type and smoking habits," *Acta. Derm. Venereol.*, vol. 83, pp. 410–413, Nov. 2003.

[78] D. Bommannan, R. O. Potts, and R. H. Guy, "Examination of stratum corneum barrier function in vivo by infrared spectroscopy," *J. Invest. Dermatol.*, vol. 95, pp. 403–408, oct 1990.

[79] T. J. Hudson, "Skin barrier function and allergic risk," *Nature Genetics*, vol. 38, pp. 399–400, apr 2006.

[80] D.-W. Kim, J.-Y. Park, G.-Y. Na, S.-J. Lee, and W.-J. Lee, "Correlation of clinical features and skin barrier function in adolescent and adult patients with atopic dermatitis," *Int. J. Dermatol.*, vol. 45, pp. 698–701, jun 2006.

[81] P. P. Bhatt, M. S. Hanna, P. Szeptycki, and H. Takeru, "Finite dose transport of drugs in liquid formulations through stratum corneum: analytical solution to a diffusion model," *Int. J. Pharm.*, vol. 50, pp. 197–203, Mar 1989.

[82] K. Kubota, "Finite dose percutaneous drug absorption: A basic program for the solution of the diffusion equation," *Comput. Biomed. Res.*, vol. 24, pp. 196–207, Apr 1991.

[83] Y. G. Anissimov and M. S. Roberts, "Diffusion modeling of percutaneous absorption kinetics. 1. effects of flow rate, receptor sampling rate, and viable epidermal resistance for a constant donor concentration," *J. Pharm. Sci.*, vol. 89, pp. 144–144, Jan 2000.

[84] G. B. Kasting, "Kinetics of finite dose absorption through skin 1. vanillylnonanamide," *J. Pharm. Sci.*, vol. 90, no. 2, pp. 202–212, 2001.

[85] J. E. Rim, P. M. Pinsky, and W. W. van Osdol, "Using the method of homogenization to calculate the effective diffusivity of the stratum corneum with permeable corneocytes," *J. Biomech.*, vol. 41, pp. 788–796, Jan 2008.

[86] A. Naegel, T. Hahn, U. F. Schaefer, C. Lehr, M. Heisig, and G. Wittum, "Finite dose skin penetration: a comparison of concentration-depth profiles from experiment and simulation," *Comput. Vis. Sci.*, vol. 14, pp. 327–339, Oct 2011.

[87] A. E. Coutinho and K. E. Chapman, "The anti-inflammatory and immunosuppressive effects of glucocorticoids, recent developments and mechanistic insights," *Mol. Cell. Endocrinol.*, vol. 335, pp. 2–13, mar 2011.

[88] S. Kardaun and M. Jonkman, "Dexamethasone pulse therapy for stevens-johnson syndrome/toxic epidermal necrolysis," *Acta. Derm. Venero.*, vol. 87, no. 2, pp. 144–148, 2007.

[89] J. J. Moré and D. C. Sorensen, "Computing a trust region step," *SIAM Journal on Scientific and Statistical Computing*, vol. 4, pp. 553–572, sep 1983.

[90] A. R. Cann, N. I. M. Gould, and P. L. Toint, *Trust Region Methods*. Society for Industrial and Applied Mathematics, jan 2000.

[91] Y. M. Rhee, E. J. Sorin, G. Jayachandran, E. Lindahl, and V. S. Pande, "Simulations of the role of water in the protein-folding mechanism," *Proc. Natl. Acad. Sci. USA*, vol. 101, pp. 6456–6461, Apr 2004.

[92] K. F. Rinne, J. C. F. Schulz, and R. R. Netz, "Impact of secondary structure and hydration water on the dielectric spectrum of poly-alanine and possible relation to the debate on slaved versus slaving water," *J. Chem. Phys.*, vol. 142, p. 215104, 2015.

[93] P. Setny, R. Baron, P. M. Kekenes-Huskey, J. A. McCammon, and J. Dzubiella, "Solvent fluctuations in hydrophobic cavity-ligand binding kinetics," *Proc. Natl. Acad. Sci. USA*, vol. 110, pp. 1197–1202, 2013.

[94] A. Erbas, D. Horinek, and R. R. Netz, "Viscous friction of hydrogen-bonded matter," *J. Am. Chem. Soc.*, vol. 134, pp. 623 – 630, 2012.

[95] R. Buchner and G. Hefter, "Interactions and dynamics in electrolyte solutions by dielectric spectroscopy," *Phys. Chem. Chem. Phys.*, vol. 11, pp. 8984 – 8999, 2009.

[96] K. F. Rinne, S. Gekle, and R. R. Netz, "Ion-specific solvation water dynamics: Single water versus collective water effects," *J. Phys. Chem. A*, vol. 118, pp. 11667 – 11677, 2014.

[97] A. Hassanali, F. Giberti, J. Cuny, T. D. Kühne, and M. Parrinello, "Proton transfer through the water gossamer," *Proc. Natl. Acad. Sci. USA*, vol. 110, pp. 13723 – 13728, 2013.

[98] X. Huang, C. J. Margulis, and B. J. Berne, "Dewetting-induced collapse of hydrophobic particles," *Proc. Natl. Acad. Sci. USA*, vol. 100, pp. 11953–11958, Sep 2003.

[99] S. Sharma and P. G. Debenedetti, "Evaporation rate of water in hydrophobic confinement," *Proc. Natl. Acad. Sci. USA*, vol. 109, pp. 4365–4370, Mar 2012.

[100] A. Luzar, "Resolving the hydrogen bond dynamics conundrum," *J. Chem. Phys.*, vol. 113, p. 10663, 2000.

[101] D. Laage, G. Stirnemann, F. Sterpone, R. Rey, and J. T. Hynes, "Reorientation and allied dynamics in water and aqueous solutions," *Annu. Rev. Phys. Chem.*, vol. 62, pp. 395–416, may 2011.

[102] D. Laage, "Reinterpretation of the liquid water quasi-elastic neutron scattering spectra based on a nondiffusive jump reorientation mechanism," *J. Phys. Chem. B*, vol. 113, no. 9, pp. 2684–2687, 2009.

[103] K. Amann-Winkel, M.-C. Bellissent-Funel, L. E. Bove, T. Loerting, A. Nilsson, A. Paciaroni, D. Schlesinger, and L. Skinner, "X-ray and neutron scattering of water," *Chem. Rev.*, vol. 116, no. 13, pp. 7570–7589, 2016.

[104] S. T. Roberts, K. Ramasesha, and A. Tokmakoff, "Structural rearrangements in water viewed through two-dimensional infrared spectroscopy," *Acc. Chem. Res.*, vol. 42, no. 9, pp. 1239–1249, 2009.

[105] J. D. Eaves, J. J. Loparo, C. J. Fecko, S. T. Roberts, A. Tokmakoff, and P. L. Geissler, "Hydrogen bonds in liquid water are broken only fleetingly," *Proc. Natl. Acad. Sci. USA*, vol. 102, no. 37, pp. 13019–13022, 2005.

[106] H. S. Chung, J. M. Louis, and W. A. Eaton, "Experimental determination of upper bound for transition path times in protein folding from single-molecule photon-by-photon trajectories," *Proc. Natl. Acad. Sci. USA*, vol. 106, pp. 11837 – 11844, 2009.

[107] S. Chaudhury and D. E. Makarov, "A harmonic transition state approximation for the duration of reactive events in complex molecular rearrangements," *J. Chem. Phys.*, vol. 133, p. 034118, 2010.

[108] W. K. Kim and R. R. Netz, "The mean shape of transition and first-passage paths," *J. Chem. Phys.*, vol. 143, p. 224108, 2015.

[109] C. J. Fecko, J. D. Eaves, J. J. Loparo, A. Tokmakoff, and P. L. Geissler, "Ultrafast hydrogen-bond dynamics in the infrared spectroscopy of water," *Science*, vol. 301, no. 5640, pp. 1698–1702, 2003.

[110] M. L. Cowan, B. D. Bruner, N. Huse, J. R. Dwyer, B. Chugh, E. T. J. Nibbering, T. Elsaesser, and R. J. D. Miller, "Ultrafast memory loss and energy redistribution in the hydrogen bond network of liquid h2o," *Nature*, vol. 434, pp. 199–202, mar 2005.

[111] L. D. Marco, M. Thämer, M. Reppert, and A. Tokmakoff, "Direct observation of intermolecular interactions mediated by hydrogen bonding," *J. Chem. Phys.*, vol. 141, no. 3, p. 034502, 2014.

[112] M. Heyden, J. Sun, S. Funkner, G. Mathias, H. Forbert, M. Havenith, and D. Marx, "Dissecting the thz spectrum of liquid water from first principles via correlations in time and space," *Proc. Natl. Acad. Sci. USA*, vol. 107, pp. 12068 – 12073, 2010.

[113] J. Stenger, D. Madsen, P. Hamm, E. T. J. Nibbering, and T. Elsaesser, "A photon echo peak shift study of liquid water," *J. Phys. Chem. A*, vol. 106, no. 10, pp. 2341–2350, 2002.

[114] K. Liu, J. D. Cruzan, and R. J. Saykally, "Water clusters," *Science*, vol. 271, no. 5251, pp. 929–933, 1996.

[115] W. T. S. Cole and R. J. Saykally, "Hydrogen bond network rearrangement dynamics in water clusters: Effects of intermolecular vibrational excitation on tunneling rates," *J. Chem. Phys.*, vol. 147, no. 6, p. 064301, 2017.

[116] J. O. Richardson, C. Pérez, S. Lobsiger, A. A. Reid, B. Temelso, G. C. Shields, Z. Kisiel, D. J. Wales, B. H. Pate, and S. C. Althorpe, "Concerted hydrogen-bond breaking by quantum tunneling in the water hexamer prism," *Science*, vol. 351, no. 6279, pp. 1310–1313, 2016.

[117] J.-H. Prinz, H. Wu, M. Sarich, B. Keller, M. Senne, M. Held, J. D. Chodera, C. Schütte, and F. Noé, "Markov models of molecular kinetics: generation and validation.," *J Chem Phys*, vol. 134, p. 174105, May 2011.

[118] G. R. Bowman, V. S. Pande, and F. Noé, "An introduction to markov state models and their application to long timescale molecular simulation," *Adv. Exp. Med. Biol.*, 2014.

[119] M. Sarich and C. Schütte, *Metastability and Markov State Models in Molecular Dynamics*. Courant Lecture Notes, American Mathematical Society, 2013.

[120] V. A. Voelz, M. Jäger, L. Zhu, S. Yao, O. Bakajin, S. Weiss, L. J. Lapidus, and V. S. Pande, "Markov State Models of Millisecond Folder ACBP Reveals New Views of the Folding Reaction," *Biophys. J.*, vol. 100, p. 515a, 2011.

[121] S. Gu, D.-A. Silva, L. Meng, A. Yue, and X. Huang, "Quantitatively characterizing the ligand binding mechanisms of choline binding protein using markov state model analysis," *PLoS Comput. Biol.*, vol. 10, p. e1003767, 2014.

[122] F. Paul, C. Wehmeyer, E. T. Abualrous, H. Wu, M. D. Crabtree, J. Schöneberg, J. Clarke, C. Freund, T. R. Weikl, and F. Noé, "Protein-ligand kinetics on the seconds timescale from atomistic simulations," *Nat. Commun.*, vol. 8, p. 1095, 2017.

[123] K. M. Thayer, B. Lakhani, and D. L. Beveridge, "Molecular dynamics–markov state model of protein ligand binding and allostery in CRIB-PDZ: Conformational selection and induced fit," *J. Phys. Chem. B*, vol. 121, pp. 5509–5514, may 2017.

[124] N. Plattner and F. Noé, "Protein conformational plasticity and complex ligand binding kinetics explored by atomistic simulations and markov models," *Nat. Commun.*, vol. 6, p. 7653, 2015.

[125] D. Shukla, Y. Meng, B. Roux, and V. S. Pande, "Activation pathway of src kinase reveals intermediate states as targets for drug design.," *Nat. Commun.*, vol. 5, p. 3397, 2014.

[126] I. M. Svishev and P. G. Kusalik, "Roto-translational motion in liquid water and its structural implication," *Chem. Phys. Lett.*, vol. 215, pp. 596 – 600, 1993.

[127] V. S. Pande, K. Beauchamp, and G. R. Bowman, "Everything you wanted to know about markov state models but were afraid to ask," *Methods*, vol. 52, no. 1, pp. 99 – 105, 2010.

[128] R. Kumar, J. R. Schmidt, and J. L. Skinner, "Hydrogen bonding definitions and dynamics in liquid water," *J. Chem. Phys.*, vol. 126, no. 20, p. 204107, 2007.

[129] M. K. Scherer, B. Trendelkamp-Schroer, F. Paul, G. Pérez-Hernández, M. Hoffmann, N. Plattner, C. Wehmeyer, J.-H. Prinz, and F. Noé, "PyEMMA 2: A software package for estimation, validation, and analysis of markov models," *J. Chem. Theo. Comp.*, vol. 11, pp. 5525–5542, oct 2015.

[130] A. Luzar and D. Chandler, "Effect of environment on hydrogen bond dynamics in liquid water," *Phys. Rev. Lett.*, vol. 76, no. 6, p. 928, 1996.

[131] Y. L. A. Rezus and H. J. Bakker, "On the orientational relaxation of hdo in liquid water," *J. Chem. Phys.*, vol. 123, no. 11, p. 114502, 2005.

[132] X.-Z. Li, B. Walker, and A. Michaelides, "Quantum nature of the hydrogen bond," *Proc. Natl. Acad. Sci. USA*, vol. 108, no. 16, pp. 6369–6373, 2011.

[133] S. Habershon, T. E. Markland, and D. E. Manolopoulos, "Competing quantum effects in the dynamics of a flexible water model," *J. Chem. Phys.*, vol. 131, p. 024501, jul 2009.

[134] W. E. and E. Vanden-Eijnden, "Towards a theory of transition paths," *J. Stat. Phys.*, vol. 123, no. 3, pp. 503–523, 2006.

[135] P. Metzner, C. Schütte, and E. Vanden-Eijnden, "Transition path theory for markov jump processes," *Multuscale Model Sim.*, vol. 7, pp. 1192–1219, Jan 2009.

[136] D. J. Bicout and A. Szabo, "Electron transfer reaction dynamics in non-debye solvents," *J. Chem. Phys.*, vol. 109, no. 6, p. 2325, 1998.

[137] M. Kijima, *Markov processes for stochastic modeling*. Stochastic modeling series, London, New York: Elsevier, 1997.

[138] S. Lloyd, "Least squares quantization in PCM," *IEEE Trans. Inf. Theory.*, vol. 28, pp. 129–137, Mar 1982.

[139] E. Blanco, H. Shen, and M. Ferrari, "Principles of nanoparticle design for overcoming biological barriers to drug delivery," *Nat. Biotechnol.*, vol. 33, p. 941, 2015.

[140] H. Schaefer, A. Zesch, and G. Stüttgen, *Skin Permeability*. Springer Science Business Media, 1982.

[141] P. Elias, "Epidermal barrier function - intercellular lamellar lipid structures, origin, composition and metabolism," *J. Control. Release*, vol. 15, p. 199, 1991.

[142] G. B. Kasting and M. A. Miller, "Kinetics of finite dose absorption through skin 2: Volatile compounds," *J. Pharm. Sci.*, vol. 95, pp. 268–280, Feb 2006.

[143] A. Naegel, M. Heisig, and G. Wittum, "Detailed modeling of skin penetration - an overview," *Adv. Drug Deliv. Rev.*, vol. 65, pp. 191–207, Feb 2013.

[144] S. Mitragotri, Y. G. Anissimov, A. L. Bunge, H. F. Frasch, R. H. Guy, J. Hadgraft, G. B. Kasting, M. E. Lane, and M. S. Roberts, "Mathematical models of skin permeability: An overview," *Int. J. Pharm.*, vol. 418, pp. 115–129, Oct 2011.

[145] K. Yamamoto, R. Flesch, T. Ohigashi, S. Hedtrich, A. Klossek, P. Patoka, G. Ulrich, S. Ahlberg, F. Rancan, A. Vogt, U. Blume-Peytavi, P. Schrade, S. Bachmann, M. Schäfer-Korting, N. Kosugi, and E. Rühl, "Selective probing of the penetration of dexamethasone into human skin by soft x-ray spectromicroscopy," *Anal. Chem.*, vol. 87, pp. 6173–6179, June 2015.

[146] K. Yamamoto, A. Klossek, R. Flesch, T. Ohigashi, E. Fleige, F. Rancan, J. Frombach, A. Vogt, U. Blume-Peytavi, P. Schrade, S. Bachmann, R. Haag, S. Hedtrich, M. Schäfer-Korting, N. Kosugi, and E. Rühl, "Core-multishell nanocarriers: Transport and release of dexamethasone probed by soft x-ray spectromicroscopy," *J. Control. Release*, vol. 242, pp. 64 – 70, 2016. International Conference on Dermal Drug Delivery by Nanocarriers, Berlin 14-16 March.

[147] D. Sisan, M. Halter, J. Hubbard, and A. Plant, "Predicting rates of cell state change caused by stochastic fluctuations using a data-driven landscape model," *Proc. Natl. Acad. Sci. U.S.A.*, vol. 109, p. 19262, 2012.

[148] J. Straub, B. Berne, and B. Roux, "Spatial dependence of time-dependent friction for pair diffusion in a simple fluid," *J. Chem. Phys.*, vol. 93, p. 6804, 1990.

[149] S. J. Marrink and H. Berendsen, "Simulation of water transport through a lipid membrane," *J. Phys. Chem.*, vol. 98, p. 4155, 1994.

[150] J. Bollinger, A. Jain, and T. Truskett, "Structure, thermodynamics, and position-dependent diffusivity in fluids with sinusoidal density variations," *Langmuir*, vol. 30, p. 8247, 2014.

[151] J. Bryngelson and P. Wolynes, "Intermediates and barrier crossing in a random energy model (with applications to protein folding)," *J. Phys. Chem.*, vol. 93, p. 6902, 1989.

[152] S. Krivov and M. Karplus, "Diffusive reaction dynamics on invariant free energy profiles," *Proc. Natl. Acad. Sci. U.S.A.*, vol. 105, p. 13841, 2008.

[153] H. Chung, S. Piana-Agostinetti, D. Shaw, and W. Eaton, "Structural origin of slow diffusion in protein folding," *Science*, vol. 349, p. 1504, 2015.

[154] A. Berezhkovskii and A. Szabo, "Time scale separation leads to position-dependent diffusion along a slow coordinate," *J. Chem. Phys.*, vol. 135, p. 074108, 2011.

[155] S. P. Lund, J. B. Hubbard, and M. Halter, "Nonparametric estimates of drift and diffusion profiles via fokker-planck algebra," *J. Phys. Chem. B*, vol. 118, pp. 12743–12749, Nov 2014.

[156] G. Hummer, "Position-dependent diffusion coefficients and free energies from bayesian analysis of equilibrium and replica molecular dynamics simulations," *New J. Phys.*, vol. 7, p. 34, 2005.

[157] M. Hinczewski, Y. von Hansen, J. Dzubiella, and R. R. Netz, "How the diffusivity profile reduces the arbitrariness of protein folding free energies," *J. Chem. Phys.*, vol. 132, no. 24, p. 245103, 2010.

[158] J. Carmer, F. van Swol, and T. Truskett, "Note: Position-dependent and pair diffusivity profiles from steady-state solutions of color reaction-counterdiffusion problems," *J. Chem. Phys.*, vol. 141, p. 046101, 2014.

[159] Y. Moussy, L. Hersh, and P. Dungel, "Distribution of [3h]dexamethasone in rat subcutaneous tissue after delivery from osmotic pumps," *Biotechnol. Prog.*, vol. 22, pp. 819–824, June 2006.

[160] E. Sparr and H. Wennerström, "Responding phospholipid membranes–interplay between hydration and permeability," *Biophys. J.*, vol. 81, p. 1014, 2001.

[161] ChemIDplus, "Dexamethasone in chemidplus databse of united states national library of medicine (nlm)," *http://chem.sis.nlm.nih.gov/chemidplus/rn/50-02-2*, 2015.

[162] O. G. Jepps, Y. Dancik, Y. G. Anissimov, and M. S. Roberts, "Modeling the human skin barrier - towards a better understanding of dermal absorption," *Adv. Drug Deliv. Rev.*, vol. 65, pp. 152–168, Feb 2013.

[163] K. Hashimoto, "Intercellular space of the human epidermis as demonstrated with lanthanum," *J. Invest. Dermatol.*, vol. 57, pp. 17–31, Jul 1971.

[164] M. Furuse, M. Hata, K. Furuse, Y. Yoshida, A. Haratake, Y. Sugitani, T. Noda, A. Kubo, and S. Tsukita, "Claudin-based tight junctions are crucial for the mammalian epidermal barrier: a lesson from claudin-1-deficient mice," *J. Cell Biol.*, vol. 156, pp. 1099–1111, Mar 2002.

[165] A. Kubo, K. Nagao, M. Yokouchi, H. Sasaki, and M. Amagai, "External antigen uptake by langerhans cells with reorganization of epidermal tight junction barriers," *J. Exp. Med.*, vol. 206, pp. 2937–2946, Dec 2009.

[166] N. Kirschner and J. M. Brandner, "Barriers and more: functions of tight junction proteins in the skin," *Ann. N. Y. Acad. Sci.*, vol. 1257, pp. 158–166, Jun 2012.

[167] J. Nocedal and S. Wright, *Numerical Optimization*. Springer-Verlag, 2006.

[168] S. H. Lee, S. K. Jeong, and S. K. Ahn, "An update of the defensive barrier function of skin," *Yonsei Med J*, vol. 47, no. 3, p. 293, 2006.

[169] Z. Nemes and P. M. Steinert, "Bricks and mortar of the epidermal barrier," *Exp. Mol. Med.*, vol. 31, pp. 5–19, mar 1999.

[170] R. Schulz, K. Yamamoto, A. Klossek, R. Flesch, S. Hönzke, F. Rancan, A. Vogt, U. Blume-Peytavi, S. Hedtrich, M. Schäfer-Korting, E. Rühl, and R. R. Netz, "Data-based modeling of drug penetration relates human skin barrier function to the interplay of diffusivity and free-energy profiles," *Proc. Natl. Acad. Sci. U.S.A.*, vol. 114, pp. 3631–3636, mar 2017.

[171] A. N. Tikhonov, *Nonlinear Ill-Posed Problems*. Springer, 2014.

[172] T. Sullivan, *Introduction to Uncertainty Quantification (Texts in Applied Mathematics)*. Springer, 2015.

[173] K. Yamamoto, A. Klossek, R. Flesch, F. Rancan, M. Weigand, I. Bykova, M. Bechtel, S. Ahlberg, A. Vogt, U. Blume-Peytavi, P. Schrade, S. Bachmann, S. Hedtrich, M. Schäfer-Korting, and E. Rühl, "Influence of the skin barrier on the penetration of topically-applied dexamethasone probed by soft x-ray spectromicroscopy," *European Journal of Pharmaceutics and Biopharmaceutics*, vol. 118, pp. 30–37, sep 2017.

[174] J. Lademann, H.-J. Weigmann, C. Rickmeyer, H. Barthelmes, H. Schaefer, G. Mueller, and W. Sterry, "Penetration of titanium dioxide microparticles in a sunscreen formulation into the horny layer and the follicular orifice," *Skin Pharmacology and Physiology*, vol. 12, no. 5, pp. 247–256, 1999.

[175] J. Lademann, U. Jacobi, C. Surber, H.-J. Weigmann, and J. Fluhr, "The tape stripping procedure – evaluation of some critical parameters," *European Journal of Pharmaceutics and Biopharmaceutics*, vol. 72, pp. 317–323, jun 2009.

[176] P. Craven and G. Wahba, "Smoothing noisy data with spline functions," *Numerische Mathematik*, vol. 31, pp. 377–403, dec 1978.

[177] C. H. Reinsch, "Smoothing by spline functions," *Numerische Mathematik*, vol. 10, pp. 177–183, oct 1967.

[178] M. Z. Nashed, "The theory of tikhonov regularization for fredholm equations of the first kind (c. w. groetsch)," *SIAM Review*, vol. 28, pp. 116–118, mar 1986.

[179] U. Tautenhahn and Q. nian Jin, "Tikhonov regularization and a posteriori rules for solving nonlinear ill posed problems," *Inverse Problems*, vol. 19, pp. 1–21, nov 2002.

[180] A. Neumaier, "Solving ill-conditioned and singular linear systems: A tutorial on regularization," *SIAM Review*, vol. 40, pp. 636–666, jan 1998.

[181] P. C. Hansen, "The truncatedSVD as a method for regularization," *BIT*, vol. 27, pp. 534–553, dec 1987.

[182] J. Baumeister, *Stable Solution of Inverse Problems*. Vieweg+Teubner Verlag, 1987.

[183] P. C. Hansen, "The l-curve and its use in the numerical treatment of inverse problems," in *in Computational Inverse Problems in Electrocardiology, ed. P. Johnston, Advances in Computational Bioengineering*, pp. 119–142, WIT Press, 2000.

[184] D. Calvetti, S. Morigi, L. Reichel, and F. Sgallari, "Tikhonov regularization and the l-curve for large discrete ill-posed problems," *Journal of Computational and Applied Mathematics*, vol. 123, pp. 423–446, nov 2000.

[185] C. R. Vogel, "Non-convergence of the l-curve regularization parameter selection method," *Inverse Problems*, vol. 12, pp. 535–547, aug 1996.

[186] M. Hanke, "Limitations of the l-curve method in ill-posed problems," *BIT Numerical Mathematics*, vol. 36, pp. 287–301, jun 1996.

[187] D. Krawczyk-Stańdo and M. Rudnicki, "Regularization parameter selection in discrete ill-posed problems — the use of the u-curve," *International Journal of Applied Mathematics and Computer Science*, vol. 17, jan 2007.

[188] L. Reichel and H. Sadok, "A new l-curve for ill-posed problems," *Journal of Computational and Applied Mathematics*, vol. 219, pp. 493–508, oct 2008.

[189] K. Kunisch, "On a class of damped morozov principles," *Computing*, vol. 50, pp. 185–198, sep 1993.

[190] S. W. Anzengruber and R. Ramlau, "Morozov's discrepancy principle for tikhonov-type functionals with nonlinear operators," *Inverse Problems*, vol. 26, p. 025001, dec 2009.

[191] O. Scherzer, "The use of morozov's discrepancy principle for tikhonov regularization for solving nonlinear ill-posed problems," *Computing*, vol. 51, pp. 45–60, mar 1993.

Abstract

In biological systems, the interaction of a particle with its environment leads to diffusive motion. This kind of motion can be observed on various length and time scales. In this thesis we develop methods for the description of biological diffusion processes across many length scales.

On the microscopic level, we investigate the normal modes of the local hydrogen bond dynamic rearrangement in liquid water from molecular dynamics simulations using Markov state models. For three water molecules, we find five well-separated slow dynamic modes with relaxation times in the 2 - 6 ps range. The eigenstates of these processes are shown to correspond to different collective interchanges of hydrogen bond donors and acceptors. We derive the complete transition network for the switching of one hydrogen bond between two acceptor water molecules. The most probable pathway corresponds to a direct switch without an intermediate state, whereas a considerable fraction of paths proceeds along alternative routes that involve different intermediate states with short-lived alternative hydrogen bonds or weakly bound states.

On the mesoscopic level, based on experimental concentration depth profiles of the anti-inflammatory drug dexamethasone in human skin, we model the time-dependent drug penetration by the 1D general diffusion equation that accounts for spatial variations in diffusivity and free energy. We develop a robust method to numerically invert the diffusion equation and thereby obtain the diffusivity and the free-energy profiles of the drug as a function of skin depth without further model assumptions. For dexamethasone, skin barrier function is shown to rely on the combination of a substantially reduced drug diffusivity in the stratum corneum (the outermost epidermal layer), dominant at short times, and a pronounced free-energy barrier at the transition from the epidermis to the dermis underneath, which determines the drug distribution in the long-time limit. We finally pursue a comparison between healthy and damaged human skin. The resulting free-energy profiles for damaged and healthy skin are essentially the same, whereas the diffusivity profile of damaged skin exhibits a significantly enhanced diffusivity within the first 10 μm of the upper skin layer. Therefore, the skin barrier dysfunction is primarily a transport property, and does not modify the equilibrium distribution of molecular solutes.

Kurzfassung

In biologischen Systemen führt die Wechselwirkung eines Partikels mit seiner Umgebung zu diffusivem Verhalten. Diese Art der Bewegung kann auf verschiedenen Längen- und Zeitskalen beobachtet werden. In dieser Arbeit werden Methoden für die Beschreibung von biologischen Diffusionsprozessen auf unterschiedlichen Längenskalen entwickelt.
Auf der mikroskopischen Ebene werden die Normalmoden dynamischer Neuanordnungen lokaler Wasserstoffbrückenbindungen in flüssigem Wasser aus MD-Simulationen mithilfe von Markov-State-Modellen untersucht. Für ein Drei-Wasser-System, finden wir fünf klar unterscheidbare langsame dynamische Moden mit Relaxationszeiten im Bereich von 2 - 6 ps. Die Zustände dieser Prozesse korrespondieren zu kollektiven Austauschen von Wasserstoffbrückenbindungen zwischen den Wassermolekülen. Wir bestimmen das komplette Übergangsnetzwerk für den Wasserstoffbrückenwechsel zwischen zwei Akzeptor-Wassermolekülen. Einem direkten Übergang ohne einen intermediären Zustand entspricht der wahrscheinlichste Pfad, wohingegen ein nicht zu vernachlässigender Anteil über Pfade geht, die verschiedene intermediäre Zustände mit kurzlebigen alternativen Wasserstoffbrückenbindungen oder schwach gebundenen Zuständen enthalten.
Auf der mesoskopischen Ebene modellieren wir die zeitabhängige Penetration des entzündungshemmenden Medikaments Dexamethason mithilfe der eindimensionalen allgemeinen Diffusionsgleichung mit ortsaufgelöster Diffusivität und Freier Energie. Dazu werden experimentelle Konzentrationsprofile von Dexamethason in menschlicher Haut verwendet. Wir entwickeln eine robuste Methode um die Diffusionsgleichung numerisch zu invertieren und dadurch das Diffusivitäts- und Freie-Energie-Profil des Medikaments ohne weitere Annahmen ortsaufgelöst zu erhalten. Für Dexamethason stellt sich heraus, dass die Hautbarrierefunktion auf einer Kombination einer deutlich reduzierten Diffusivität im Stratum Corneum (der äußersten epidermalen Hautschicht), dominant auf der Kurzzeitskala, und einer ausgezeichneten Freie-Energie-Barriere am Übergang von der Epidermis zur Dermis beruht, die die Verteilung im Langzeitlimes charakterisiert. Darüber hinaus vergleichen wir gesunde mit geschädigter Haut. Die sich ergebenden Freie-Energie-Profile sind in beiden Fällen gleich, wohingegen die Diffusivität von geschädigter Haut in den ersten 10 Mikrometern der obersten Hautschicht deutlich höher ist. Es ergibt sich, dass die Dysfunktion der Hautbarriere hauptsächlich eine Transporteigenschaft ist und die Gleichgewichtsverteilung von diffundierenden Partikeln nicht beeinflusst.

Selbstständigkeitserklärung

Hiermit erkläre ich, dass ich die vorliegende Dissertationsschrift mit dem Titel

Multi-scale Diffusion Processes - From Hydrogen Bonds to Human Skin

selbständig angefertigt und hierfür keine anderen als die angegebenen Hilfsmittel verwendet habe. Die Arbeit ist weder in einem früheren Promotionsverfahren angenommen noch als ungenügend beurteilt worden.

Berlin, den 5. Juli 2018

Curriculum vitae

For data privacy reasons, the curriculum vitae is not included in the online version of this thesis.

Danksagung

Ich möchte mich an dieser Stelle bei allen bedanken, die mich zum Vollenden dieser Arbeit unterstützt haben. Insbesondere bei meinem Betreuer Prof. Dr. Roland Netz für die intensive Betreuung und inspirierenden Diskussionen, der mir auch hinreichend Freiraum ließ, meinen eigenen Gedanken und Ideen zu folgen. Darüber hinaus danke ich allen Co-Autoren für ihre Mitarbeit sowie für die spannenden Diskussionen und Perspektiven aus anderen wissenschaftlichen Disziplinen.

Besonderer Dank geht natürlich an meine Familie, die mich in vielerlei Hinsicht unterstützt hat. Ich danke all meinen ehemaligen und aktuellen Arbeitskollegen für die tolle und harmonische Atmosphäre, insbesondere Julian, der sich immer Zeit genommen hat, meine Fragen zu beantworten und mir neuen Input zu geben. Nicht zu vergessen natürlich auch unsere verlässliche Sektretärin Annette, die mich und alle anderen in unserer Gruppe in vielen organisatorischen Dingen unterstützt hat.